Northumbria Research Link

Citation: Ford, Bethan (2022) Investigation of kesterite solar cells on molybdenum foil substrates. Doctoral thesis, Northumbria University.

This version was downloaded from Northumbria Research Link: https://nrl.northumbria.ac.uk/id/eprint/50190/

Northumbria University has developed Northumbria Research Link (NRL) to enable users to access the University's research output. Copyright © and moral rights for items on NRL are retained by the individual author(s) and/or other copyright owners. Single copies of full items can be reproduced, displayed or performed, and given to third parties in any format or medium for personal research or study, educational, or not-for-profit purposes without prior permission or charge, provided the authors, title and full bibliographic details are given, as well as a hyperlink and/or URL to the original metadata page. The content must not be changed in any way. Full items must not be sold commercially in any format or medium without formal permission of the copyright holder. The full policy is available online: http://nrl.northumbria.ac.uk/policies.html

Northumbria University NEWCASTLE

CUSTOMER SERVICE EXCELLENCE CSE

UniversityLibrary

Investigation of Kesterite Solar Cells on Molybdenum Foil Substrates

Northumbria University
NEWCASTLE

Bethan Ford

Doctor of Philosophy

2022

Investigation of Kesterite Solar Cells on Molybdenum Foil Substrates

Bethan Ford

Thesis in partial fulfilment of the requirements of the University of Northumbria for the degree

Doctor of Philosophy

Department of Mathematics, Physics and Electrical Engineering

February 2022

Abstract

Kesterite $Cu_2ZnSn(S,Se)_4$ (CZTSSe) is an attractive photovoltaic absorber material, demonstrating high theoretical power conversion efficiency. CZTSSe is comprised of low toxicity, low cost and earth abundant elements, has a high absorption coefficient and a tuneable direct energy band gap. In this work, Cu_2ZnSnS_4 (CZTS) nanoparticle inks were fabricated using hot injection of metallic precursors in surfactant, deposited on flexible Mo foil substrates and processed into to thin film CZTSSe solar cell devices. The work focuses on studying flexible CZTSSe devices for wide scale applications; in particular, striving towards comparable efficiencies to those on rigid substrates, investigation into the behaviour of flexible devices when bent and the recovery of flexible CZTSSe over time.

In order to achieve high efficiency devices on flexible substrates, an alkali doping source is required. When fabricating on rigid soda lime glass (SLG) an intrinsic Na source is present in the substrate, reported to promote grain growth and reduce recombination centres in the absorbers. Introducing a slide of SLG during the high temperature selenisation step of the device fabrication on Mo foil substrates results in an absolute efficiency improvement of 1%. Using this doping method, CZTSSe solar devices were fabricated on Mo foil demonstrating a power conversion efficiency (PCE) of 4.5%. Flexible CZTSSe devices show no PCE degradation when bent to a radius of curvature (ROC) of 64 mm. This is a representative ROC for new applications which include curved solar cells. Another factor, which is important for new PV application, is device degradation over time. CZTSSe devices exhibit time-based device degradation. By introducing an annealing step of 150 °C for 10 minutes in Ar, the initial device performance is recovered.

Contents

List of Figures

List of Tables

Publications

Papers

B. Ford, M C. Nayor, X. Xu, G. Zoppi, V. Barrioz, S. Bull and N S. Beattie, "Performance under bending of Mo-foil based CZTSSe solar cells made from nanoparticle inks" In Preparation (2022).

Matthew C. Naylor, Devendra Tiwari, Alice Sheppard, Jude Laverock, Stephen Campbell, **Bethan Ford**, Xinya Xu, Michael Jones, Yongtao Qu, Pietro Maiello, Vincent Barrioz, Neil S. Beattie, Neil A. Fox, David J. Fermin, Guillaume Zoppi,"Ex-situ Ge-doping of CZTS Nanocrystals and CZTSSe Solar Absorber Films", Faraday Discussions (2022).

S. Campbell, M. Duchamp, **B. Ford**, M. Jones, L L. Nguyen,M C. Naylor, X. Xu, P. Maiello, G. Zoppi, V. Barrioz, N S. Beattie and Y. Qu, "Recovery mechanisms in aged kesterite solar cells, ACS Applied Energy Materials, 5, 5404-5414 (2022).

X. Xu, M C. Naylor, M. Jones, **B. Ford**, S J. Bull, S. Campbell, Y. Qu, S M. Garner, F M. Behan, V. Akhavan, H. Mitrani, V. Barrioz, G. Zoppi and N S. Beattie, "A design-led approach to photovoltaics manufacturing", Renewable Energy, *Submitted*.

X. Xu, Y. Qu, S. Campbell, M. Le Garrec, **B. Ford**, V. Barrioz, G. Zoppi and N S. Beattie, "Solution processing route to Na incorporation in CZTSSe nanoparticle ink solar cells on foil substrates", Journal of Materials Science: Materials in Electronics, 30, 7883-7889 (2019).

Conferences

B. Ford, Y. Qu, M. Couturieux, G. Zoppi, V. Barrioz and N S. Beattie. "CO_2 cleaning of $Cu_2ZnSn(S,Se)_4$ solar cells fabricated from nanoparticle ink", NECEM International Conference on Energy Materials and Interfaces, Newcastle University, 29th July-1st August 2019, Poster presentation.

Acknowledgements

I am grateful to my primary supervisor Professor Neil Beattie for his supervision and support during my PhD. In addition, I would like to thank my secondary supervisor Professor Guillaume Zoppi for his insight and guidance throughout my work. I would also like to show my gratitude to Dr. Vincent Barrioz for his continuous help and shared knowledge over the course of my project. A special thanks goes to the technicians within the department, Pietro Maiello and Rebecca Payne for their help and encouragements not only with technical matters but also personally. I would also like to thank my research group for their contributions and bettering my scientific ability, specifically Matthew Naylor and Ryan Voyce, for their encouragement and company.

During my research, I have been lucky enough to benefit from expertise, support and many laughs from friends Matthew Parnell, Luke Haworth, Prashant Agrawal and David Roughton. My PhD would have been a lot more difficult without them. In addition I would like to thank all my family and friends for their continued support.

Above all, I thank my Mam, Dad, Niall and Ray. I wouldn't have been able to do this without them.

Declaration

I declare that the work presented in this thesis has not been submitted for any other award and is all my own. I confirm that this thesis fully acknowledges opinions, ideas and contributions from the work of others. Ethical approval for the research has been approved by the University Ethics Committee on 31/01/2019.

I declare the word count of this thesis is 30,872 words.

B. Ford

22/02/2022

Chapter 1

Introduction

1.1 Motivation for Research

The Shell Sky scenario describes net zero carbon dioxide emissions by 2070 [1]. A potential contribution to this scenario is the further installation of photovoltaic (PV) systems and deployment of PV into new applications. PV devices enable the direct conversion of sunlight into electrical power. In addition to this, flexible PV devices allow both building integrated PV (BIPV) [2] and vehicle integrated PV (VIPV) devices [3] and are potentially more economically viable than traditional PV, such as solar farms and roof mounts. To fabricate such flexible devices, thin film materials are lightweight, flexible and cost-effective, an important feature for growing the PV market. Flexible solar devices also have the advantage of low cost manufacturing techniques such as roll-to-roll processing, which in turn shortens the energy payback time [4].

Currently, the thin film market is dominated by the materials CdTe and Cu(InGa)(S,Se)$_2$ (CIGS) both achieving over 20% efficiency with the latter demonstrating a record efficiency of 23.3% [5, 6]. The ability for mass production of both materials however is hindered by the scarcity and/or toxicity of In, Ga and Cd which are classified as critical raw materials [7]. Recently, perovskite materials have demonstrated quick advancements, achieving 23.6% in a short amount of time, however, as a new technology the devices are still unstable [8–10]. Kesterite CZTSSe is an attractive material for thin film applications due to its high absorption coefficient over the visible range ($\sim 10^4$ cm^{-1}) and direct tuneable band gap based on the S:Se ratio [11–15]. Additionally, CZTSSe provides environmental and economic benefits such as relatively low toxicity, high stability and low cost

earth abundant elemental composition. Champion CZTSSe solar cell devices demonstrate a PCE of 12.6% fabricated using a solution based method; however, this method utilises hydrazine which is highly toxic and potentially explosive [16, 17]. A more sustainable and less hazardous alternative is hot injection of metallic precursors into surfactant to create nanoparticle inks, yielding PCE values of up to 9.6% [18]. This value of efficiency however, is reported for CZTSSe devices fabricated on rigid surfaces, typically soda lime glass (SLG). Flexible device performance depends heavily on the chosen substrate; such as ultra thin flexible glass [19, 20], stainless steel [21] or Mo foil [4, 22, 23], where the latter demonstrates a record PCE of 10 .3% using vacuum based fabrication processes. Mo foil is a particularly attractive substrate, due to the compatibility of its coefficient of thermal expansion (CTE) with CZTSSe, high electrical conductivity and flexibility.

In order to maximise the full potential of PV technologies into niches in the market [24], flexible PV devices with competitive cost, efficiency and flexibility are essential.

1.2 Thesis Structure

This thesis is divided into 8 chapters. Chapter 2 introduces photovoltaic theory alongside semiconductor principles and outlines the properties of CZTSSe as a material for solar cell device application. The experimental methodology used to fabricate and characterise CZTSSe solar cells is presented in Chapter 3. Chapters 4, 5, 6 provide and analyse experimental results. Chapter 4 focuses on doping methods to improve flexible device performance. In Chapter 5, the effect of bending is analysed with an increasing radius of curvature and cyclic testing regime. In Chapter 6, the effects of a post fabrication annealing step is explored and device recovery is systemically investigated. Finally, the conclusion of this work alongside an outlook for further work is described in Chapter 7.

Chapter 2

Photovoltaic Theory

2.1 History of Solar Cells

Edmond Becquerel reported the first photovoltaic cell in 1837. He discovered that current and voltage were generated when silver chloride in an electrolyte was subject to different types of light [25]. Following his discovery, the first sight of the photovoltaic effect in a solid system was reported by Adams and Day in 1876 in which they observed current flowing through a selenium bar when only subject to light [26]. Later, in 1883, the first thin film photovoltaic devices were fabricated by Fritts. Fritts prepared selenium films by compressing molten selenium between two metal plates and coating in a thin layer of gold, achieving a power conversion efficiency of 1% [27]. Albert Einstein, in 1905, drew the world's attention to solar energy when he published a scientific paper on the photoelectric effect. This work led him to win the Nobel prize in physics in 1921. The development of the theory of semiconductor-metal junctions by Schottky and Mott in 1939 [28, 29] described the Schottky barrier, where light travels through a thin metal layer before reaching the semiconductor [30]. Schottky barriers demonstrate rectifying behaviour, which, enable them to be used as diodes. The Schottky-Mott rule therefore predicted the Schottky barrier height according to the semiconductor material ionisation energy and the work function of the metal used [31]. The first alternative to the Schottky barrier came in 1954 by Bell laboratories. This was the first use of the p-n junction, created by Pearson, Fuller and Chapin, producing a silicon cell with a PCE of 4% [32]. Following their work, Hoffman Electronics furthered the field by achieving PCE's of 10% in 1959 by reducing the device series resistance by developing electrical contacts [33,34].

From the 1950's, the PV market and research continued to grow, specifically when the search for renewable energy began in the 1970's during the first major oil crisis dubbed the energy crisis. By 2000, silicon solar cells had reached an efficiency of 20% with further materials being explored such as GaAs and CdTe.

In 2021, the international energy agency reported that 290 GW of renewable power was commissioned that year, a 3% growth on the previous year. This energy was driven by solar PV, accounting for over half the renewable power expansion in 2021 [35]. In the next few years solar PV capacity, alongside other renewable technologies, is predicted to grow as seen in Figure 2.1. To allow this growth to continue, research is continuously being conducted on PV materials, with the progress in all cell types and materials shown in Figure 2.2 [36]. Within the solar cell technologies listed, kesterite CZTSSe is still within the emerging technologies category but has undergone significant development in its short history. The initial rise in of CZTS was rapid in comparison to other thin film technologies is due to its similarities to CIGS, which enabled CZTS progression to be quick with already established ways in which CIGS cells were enhanced. CZTS research has since slowed, with the record efficiency still considerable lower than the thin film competitors. CZTSSe cells are an example of single junction devices, meaning there is only one layer of absorber material within the device. The efficiency achievable is, therefore, limited by the Shockley-Quessier limit, which defines the maximum conversion efficiency a material can generate (discussed in Section 2.6) [37]. At a band gap of 1.34 eV, the maximum efficiency achievable for a single junction device is 33.7% [38]. Kesterite has a band gap range of 1 to 1.5 eV. Theoretically, CZTSSe can achieve efficiencies over 30%.

2.2 Light Properties

Work conducted by Einstein and Planck dictates that light can be observed as both waves and particles [39]. Electromagnetic radiation can be quantised in particles known as photons, defined as a collection of waves that interact either localised or spatially. Because of this, a photon may appear as a wave or particle, yielding the term particle-wave duality. The energy of photons (E) can be therefore characterised using their wavelength λ, via the relation in Equation 2.1.

$$E = \frac{hc}{\lambda}, \tag{2.1}$$

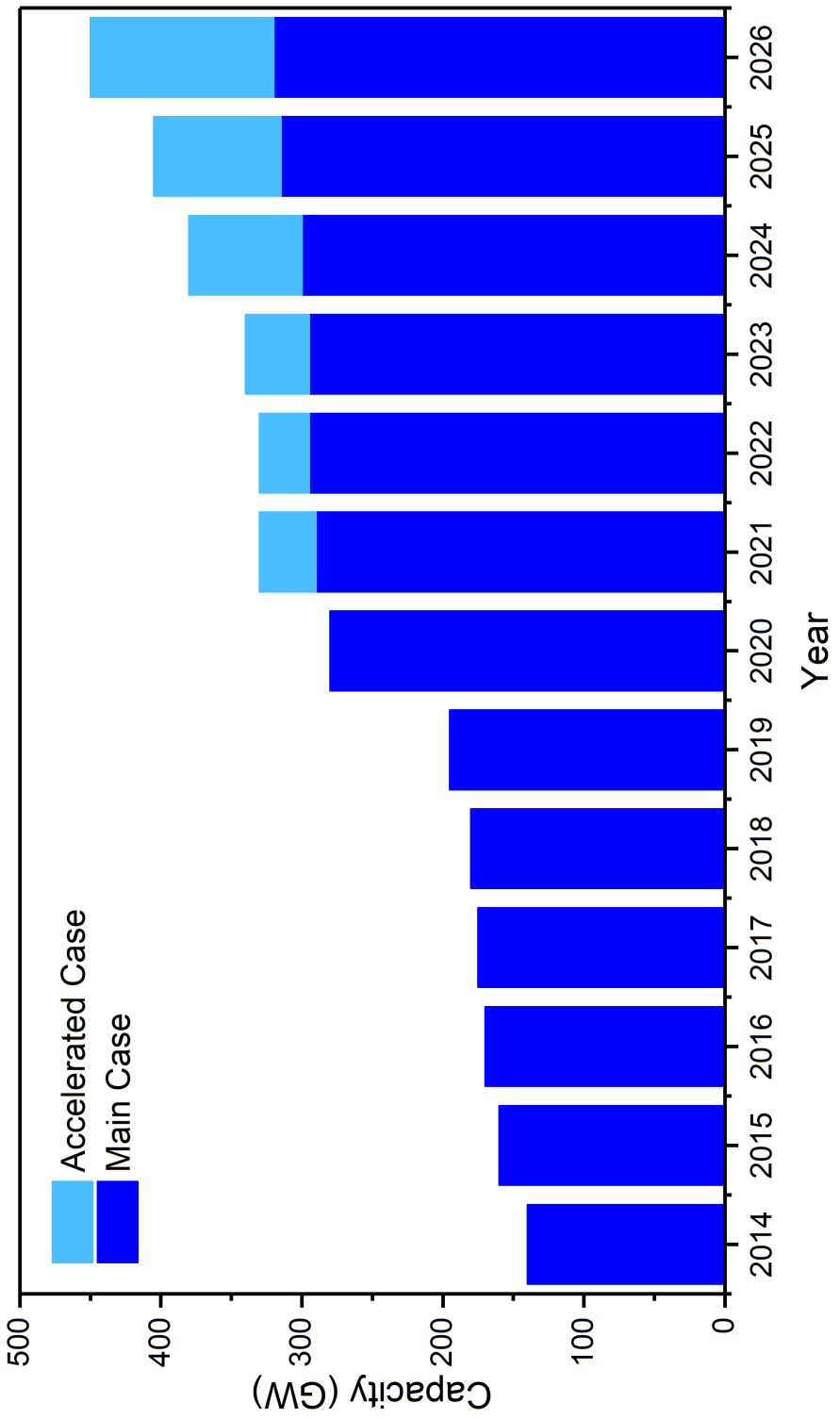

Figure 2.1: Renewable power capacity from 2014 to 2021 with predicted capacity to 2026. The accelerated case here assumes governments address policy, regulatory and implementation challenges until 2026. [35].

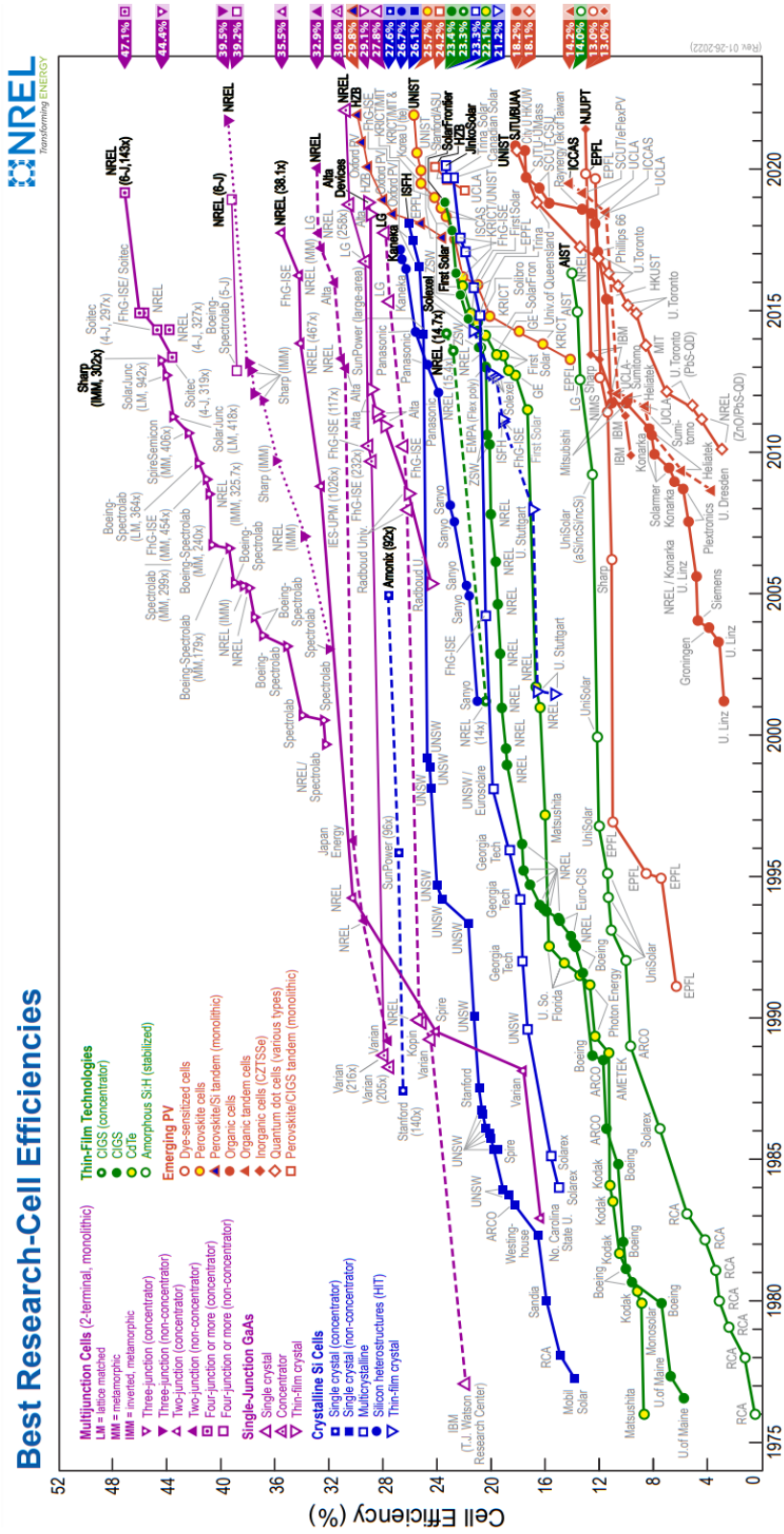

Figure 2.2: Highest confirmed conversion efficiencies for a range of photovoltaic technologies [36].

where h is Planck's constant and c is the speed of light. The photon flux Φ is defined as the number of photons per second per m^2. Using Φ and E, the power density of the incident light on the device at a given wavelength can be obtained with Equation 2.2

$$H = \Phi \times \frac{hc}{\lambda}. \tag{2.2}$$

2.3 Semiconductor Fundamentals

2.3.1 Energy Band Gap

Semiconductor materials are found in group IV, groups III and V, or groups II and VI in the periodic table. Each semiconductor material is comprised of tightly bonded atoms, each with electrons covalently bonded formed between atoms, localised around the atom. At absolute 0 K, all electrons are are stuck in their bonded arrangement. With an increase in temperature, these electrons can gain energy to release from their bonds and therefore, take part in conduction. At absolute 0 K, a semiconductor behaves as an insulator, shown in Figure 2.3a, where as at room temperature a semiconductor has sufficient free electrons that it can behave as a conductor, shown in Figure 2.3b. In a large crystal structure the covalent electrons, known as valence electrons, can interact with each other. Interaction causes the energy levels of the electrons to shift within the structure and split into a number of closely spaced levels. In solids, the energy levels formed can be considered as a continuous band forming the energy band of the material. With a decreasing inter atomic distance, the valence electrons energy levels split into a range of energy bands. The two most important of these bands are the highest occupied being the conduction band with a conduction band minimum (CBM) and the lowest unoccupied being the valence band with a valence band maximum (VBM). The CBM has an energy E_c and VBM an energy E_v. The energy band gap E_g, given by Equation 2.3 is the minimum energy required to excite an electron from the bound state in the valence band into the conduction band to be free to participate in conduction

$$E_g = E_c - E_v. \tag{2.3}$$

The band structure of the semiconductor is obtained from plotting the energy E with momentum p, shown in Figure 2.4. Considering the relationship between E and p given in Equation 2.4, the energy possible for a given p value yields an oscillating plot. Dependant on the relative position of E_c and E_v, the band gap can therefore be direct or indirect. In a direct semiconductor, the VBM and CBM peaks have the same momentum, resulting in an

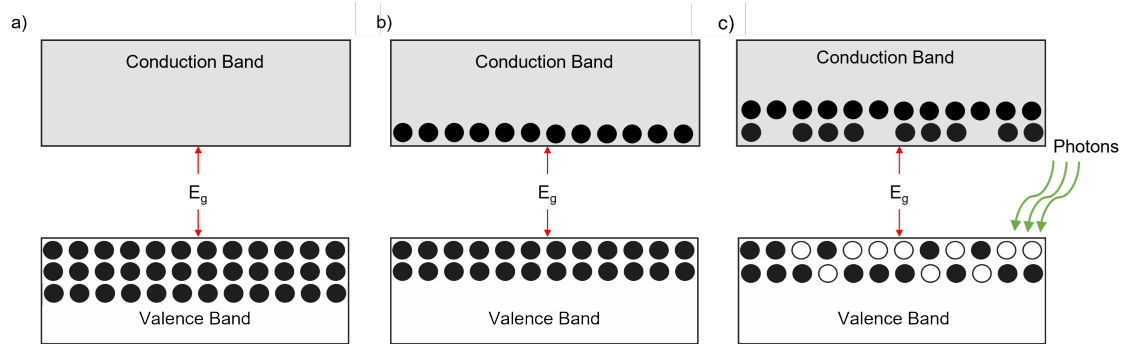

Figure 2.3: Energy band diagram for a semiconductor material at a) 0 K, b) 300 K and c) 300 K with incident light.

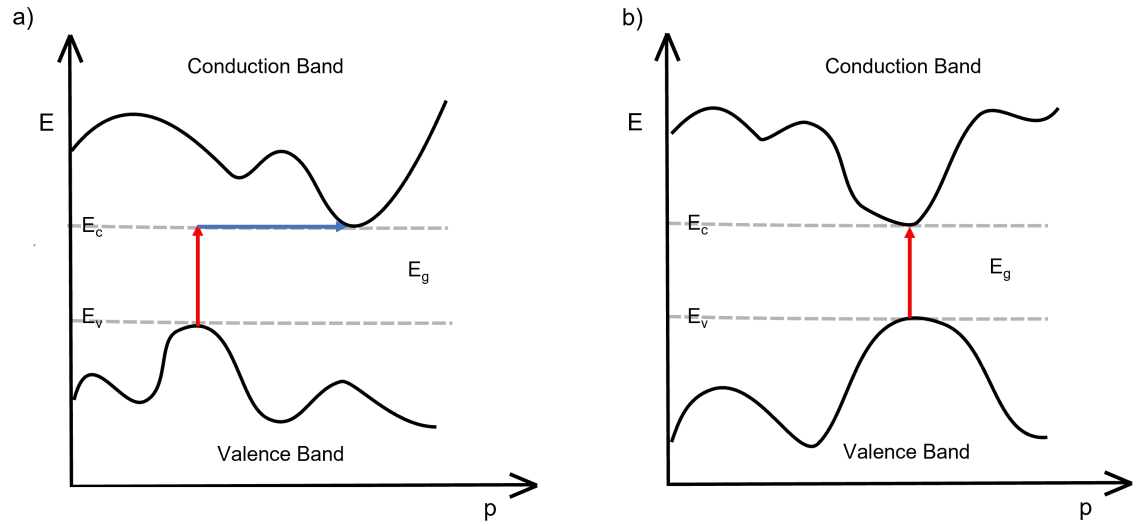

Figure 2.4: Energy-momentum diagram for a) an indirect band gap semiconductor and b) a direct band gap semiconductor.

electron with energy equal to E_g is able to be excited directly across the gap. This means, at energies above the band gap of the material, the absorption coefficient is very large in comparison to indirect band gap materials where the increase is small at the band edge. This results in much less material required for high light absorption and is the basis of thin film solar cells [40,41]. In the case of indirect band gap semiconductors, both energy and momentum are required for an electron to travel from VBM to CBM, shown in Figure 2.4a. This results in lower light absorption and therefore a thicker semiconductor layer is required for sufficient performance. Si is an example of this [42].

$$E = \frac{p^2}{2m_e}, \tag{2.4}$$

where m_e is the mass of an electron. When a semiconductor material acts as an insulator with a band structure shown in Figure 2.3a, the electrons occupy the valence band leaving

the conduction band free of any electrons and no charge is produced. Semiconductor materials exhibit a sensitivity to temperature and light. When a semiconductor material is at room temperature, shown in Figure 2.3b, the conductivity shows an increase with more electrons present within the conduction band. Illuminating the material enables incident photons to excite the electrons within the valence band and, with sufficient energy equal to or greater than the band gap energy, they are excited from the valence band to the conduction band, as seen in Figure 2.3c.

2.3.2 Carriers

Carriers under Equilibrium

As outlined in Section 2.3.1, when electrons are excited from the valence band to the conduction band, free carriers are observed in both bands. The concentration of these carriers are denoted as intrinsic carrier concentration (n_i). An intrinsic material is one in which no impurities have been added. The probability on an electron with a given E occupying an electronic state in an intrinsic semiconductor is described by the Fermi-Dirac distribution function *F(E)* given by Equation 2.5.

$$F(E) = \frac{1}{1+\exp((E-E_F)/kT)} \tag{2.5}$$

where E_F is the energy at the Fermi level, k is Boltzmann's constant and T is absolute temperature. When $(E\text{-}E_F)>3kT$, the electron density in the conduction band n and the hole density in the valence band p can be derived using Equations 2.6 and 2.7

$$n = N_c \exp(-(E_c - E_F)/kT), \tag{2.6}$$

$$p = N_v \exp(-(E_F - E_v)/kT). \tag{2.7}$$

Here, N_c and N_v are defined as the density of states in the conduction band and the valence band respectively. In an intrinsic semiconductor $n{=}p{=}n_i$, where every hole in the valence band corresponds to every exited electron in the valence band. From this, the intrinsic Fermi level E_i can be obtained using Equation 2.8.

$$E_i = \frac{E_c + E_v}{2} + \frac{kT}{2}\ln(\frac{N_v}{N_c}) \tag{2.8}$$

as $\ln\frac{N_\mathrm{V}}{N_\mathrm{C}} << \frac{E_c+E_v}{2}$, the Fermi level lies in the middle of the band gap at room temperature.

Doping

Artificially introducing impurities into the semiconductor forces the material to become extrinsic. This is achieved by introducing donors (electrons) or acceptors (holes) in the material. The majority carriers are used to determine the materials doping type. For example, introducing excess donors or 'donor doping' creates a n-type material and similarly introducing acceptors creates a p-type material. Materials such as CZTS are intrinsically doped by defects causing it to have p-type properties. With n or p-type doing, the Fermi level moves within the structure and is calculated using Equations 2.9 and 2.10.

$$E_c - E_F = kT \ln(\frac{N_c}{N_D}), \tag{2.9}$$

$$E_F - E_v = kT \ln(\frac{N_v}{N_A}) \tag{2.10}$$

N_D and N_A here denote the donor and acceptor concentration respectively. As the doping concentration increases, the Fermi level moves closer to the conduction band or the valence band dependant on the doping type. Excess donors create an isolated energy level E_D, similarly an excess of acceptors creates an energy level E_A. In very heavily doped situations, the Fermi level is above the conduction band and excited electrons must exceed the Fermi level energy. This widening of the semiconductor band gap is known as the Burstien-Moss effect [43].

The law of mass action dictates that the product of the majority and minority carrier concentration is constant, as in Equation 2.11

$$np = n_i^2. \tag{2.11}$$

Using Equations 2.11, 2.6 and 2.7, n and p can be expressed as the following Equations 2.12 and 2.13.

$$n = n_i \exp \frac{(E_F - E_i)}{kT}, \tag{2.12}$$

$$p = n_i \exp \frac{(E_i - E_F)}{kT} \tag{2.13}$$

the law of mass action is therefore applicable to both intrinsic and doped semiconductors in equilibrium conditions.

Generation and Recombination

Photons with energy E equal to or greater than the energy band gap of the semiconductor material E_g can excite an electron from the VBM to the CBM. The absorption of the pho-

ton produces minority and majority carriers, known as an electron hole pair. The distance light travels into the material before being absorbed is determined by the absorption coefficient α. The absorption coefficient is dependant on the wavelength of the incident light, with a strong absorption edge at the material band gap. α is obtained using Equation 2.14

$$\alpha = \frac{4\pi k}{\lambda}, \tag{2.14}$$

where k is the extinction coefficient in this case and λ is the wavelength. The absorption depth is given as the inverse of the absorption coefficient, and details the distance different wavelengths of light penetrate into the semiconductor material.

Based on the Beer-Lambert law, the intensity of light at any point in the material can be calculated using Equation 2.15.

$$I = I_0 \exp(-\alpha t), \tag{2.15}$$

where t is the thickness of the semiconductor and I_0 is the incident intensity. This is valid for the CZTSSe solar cells fabricated in this work with a thickness of approximately 1.1 µm. Assuming that the loss in intensity results in the generation of an electron hole pair in the semiconductor, the generation rate G is calculated using the photon flux at the surface of the material N_0 as a function of distance x into the material. The net generation is the sum of the calculated generation a each wavelength

$$G(\lambda) = \alpha(\lambda) N_0 \exp(-\alpha(\lambda) x). \tag{2.16}$$

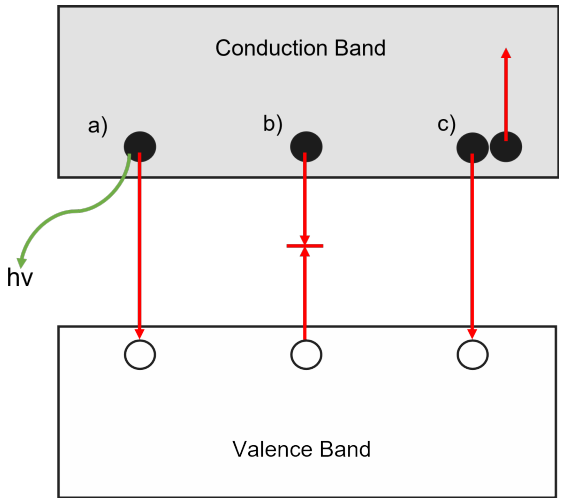

Figure 2.5: a) Radiative b) SRH and c) Auger recombination mechanisms in semiconductor materials.

An excess of carriers produced in a semiconductor material leads to a non equilibrium state. For this to be restored, recombination occurs in which an electron hole pair recombine. Two main types of recombination are present in semiconductor materials; radiative and non-radiative, shown in Figure 2.5. Examples of non-radiative include Auger and Shockley-Read-Hall (SRH). Radiative recombination dominates in direct band gap materials, as it is the process of an electron relaxing to a lower energy state, and recombining with a hole in the valence band, giving off a photon in the process. The direct recombination rate (R) can be calculated using Equation 2.17

$$R = \beta pn. \tag{2.17}$$

Here, β is a proportionality constant. In order to satisfy the mass action law, the rate of generation G_{th} and the rate of recombination R_{th} are balanced, also known as the thermal generation and recombination. Considering Equation 2.11 the recombination and generation must satisfy Equation 2.18.

$$G_{th} = R_{th} = \beta n_{p0} p_{p0}, \tag{2.18}$$

where n_{p0} and p_{p0} is the electron and hole density respectively at thermal equilibrium. When a semiconductor material is illuminated, carriers are generated at a generation rate of G_L. Under illumination therefore, the generation and recombination rate becomes;

$$G = G_L + G_{th}, \tag{2.19}$$

$$R = \beta (n_{p0} + \Delta n)(p_{p0} + \Delta p). \tag{2.20}$$

Where Δn and Δp are the generated carrier concentrations due to excitation from the incident light.

2.4 The p-n Junction

In order to separate charged carriers to contribute to a photocurrent, an electric field is required. A p-n junction is formed by joining a n-type material to a p-type material, shown in Figure 2.6. The p-type material has a high concentration of hole majority carriers, similarly the n-type material contains a large concentration of electrons. When the semiconductor materials are joined together, the electrons diffuse from the n-type material to the p-type material and simultaneously the holes from the p-type material flow into the n-type. This process would continue to occur if the majority carriers were not charged,

however when the carriers diffuse in this situation, they leave behind an exposed fixed ion core in the lattice of the semiconductor material. From the ion cores, an electric field (E) forms between the positive ion cores in the n-type and the negative ion cores in the p-type. The electric field sweeps free carriers close to the junction across, creating an area depleted of all carriers known as the depletion region. As shown in Figure 2.6a, electron and holes can either diffuse into the material or be swept across the depletion region known as drift current. When the drift and diffusion current are equal, the junction is in equilibrium and has a net zero current. Once a majority carrier does cross the junction however, it becomes a minority carrier and will continue to diffuse away from the junction and travel the minority carrier diffusion length until it recombines, defined as the average distance a carrier can travel between generation and recombination. Arising from E, a built in potential (V_{bi}) is observed as a electrostatic potential across the junction.

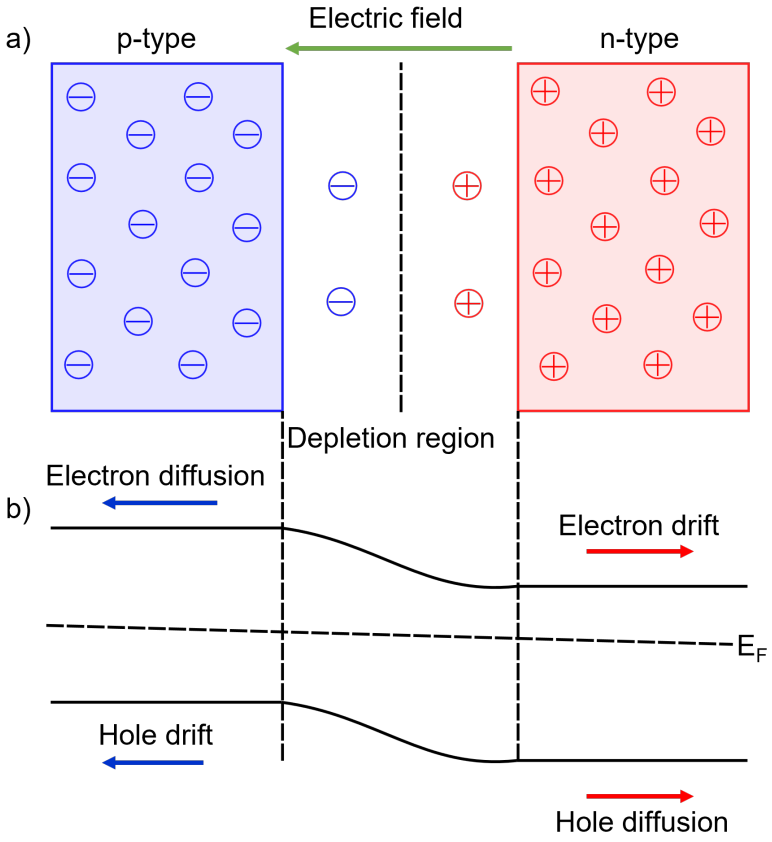

Figure 2.6: a) Diagram of a p-n junction at equilibrium and b) the energy band diagram of the p-n junction.

The total negative charge in the p-type semiconductor material is required to equal the positive charge in the n-type material to obtain charge neutrality, as in Equation 2.21.

$$N_A x_p = N_D x_n \tag{2.21}$$

where x_p and x_n is the distance the depletion region extends into the p and n-type materials respectively. The total width of the depletion region therefore, is obtained using Equation 2.22

$$W = x_n + x_p. \tag{2.22}$$

Equation 2.22 can be expressed as;

$$W = \sqrt{\frac{2\varepsilon_s}{q}(\frac{N_A + N_D}{N_A N_D})V_{bi}}, \tag{2.23}$$

where ε_s is the semiconductor material permitivity. With an increasing doping concentration in either the p or n-type material, the depletion width varies and extends further into the material with the lower doping concentration. When the p-type semiconductor material has a higher doping concentration Equation 2.23 is simplified to Equation 2.24

$$W = \sqrt{\frac{2\varepsilon_s V_{bi}}{qN_A}}. \tag{2.24}$$

2.4.1 Heterojunction

When a p and n-type material are joined to form a p-n junction which do not have the same energy band gap, unlike the previous example which is that of a homojunction, a heterojunction is formed. In addition to different energy band gaps, heterojunction materials demonstrate different electron affinities χ and work functions φ. The work function of the semiconductor material is the energy required to move an electron from the Fermi level. The work function is not constant, as the Fermi level fluctuates depending on doping density. The Fermi level can be obtained for a n-type semiconductor (E_{Fn}) in Equation 2.25 and similarly for p-type semiconductors (E_{Fp}) using Equation 2.26.

$$E_{Fn} = E_{Cn} - \delta_n, \tag{2.25}$$

$$E_{Fp} = E_{Vp} - \delta_p \tag{2.26}$$

where δ_n is the difference between the E_{Fn} and the bottom of the conduction band E_{Cn} and δ_p is the energy difference between E_{Fp} and the top of the valence band E_{Vp}. The electron affinity, however, is constant for an intrinsic semiconductor material and is used to obtain the energy difference between the conduction band edges (ΔE_c) of the two materials, given in Equation 2.27

$$\Delta E_c = q(\chi_p - \chi_n). \tag{2.27}$$

Using Equation 2.27, the difference in the valence band energy (ΔE_v) can be expressed as:

$$\Delta E_v = \Delta E_g - \Delta E_c. \tag{2.28}$$

When a heterojunction is formed, charge is transferred as in a homojunction, until the Fermi level is equal across the junction. The formed electric field is, however, non continuous due to the difference in the material dielectric constants. The built in potential of the electric field therefore becomes the sum of the electrostatic potentials of the n-type V_{bn} and p-type V_{bp} semiconductor materials when in equilibrium, given in Equation 2.29

$$V_{bi} = V_{bn} + V_{pn}. \tag{2.29}$$

The total depletion width of the depletion region is therefore given as:

$$W = \sqrt{\frac{2\varepsilon_n\varepsilon_p(N_A+N_D)^2(V_{bi}-V)}{qN_AN_D(\varepsilon_nN_D+\varepsilon_pN_A)}}. \tag{2.30}$$

Similarly to Equation 2.24 when the doping concentration is higher in one material, for example in the p-type semiconductor, Equation 2.30 is simplified to:

$$W = \sqrt{\frac{2\varepsilon_p(V_{bi}-V)}{qN_A}}. \tag{2.31}$$

2.4.2 Schottky Junction

In order to collect the photogenerated carriers from the p-n junction, completed solar cell devices require metal contacts for current extraction. A Schottky barrier is formed, illustrated in Figure 2.7, when a semiconductor material, in this example n-type, is in contact with a metal.

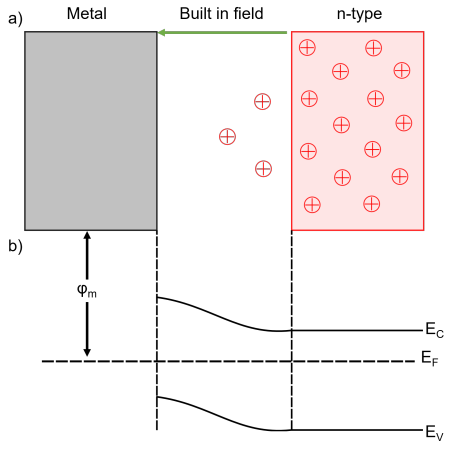

Figure 2.7: a) Schematic of a Schottky junction formed between an n-type semiconductor material and a metal and b) the energy band diagram of the Schottky junction.

The Fermi levels in an Schottky barrier must be equal to one another in thermal equilibrium. Electrons from the conduction band of the semiconductor are free to move into the metal until the Fermi levels are equal. This results in a positive charge at the semiconductor side of the junction and a negative charge at the metal, due to an increase in electron concentration. The depletion region is formed within the semiconductor material and a built in potential is formed, preventing electrons from continuously moving towards the metal contact. The built in potential is therefore calculated as the difference in the work function of the two materials, shown in Equation 2.32

$$V_{bi} = \varphi_m + \varphi_s. \tag{2.32}$$

2.5 Solar Cell Theory

2.5.1 The Ideal Diode Equation

A diode primarily allows for current to flow in one direction when a bias or voltage is applied. Diodes allow a reverse voltage up to a breakdown voltage before a significant increase in the leakage current is observed. The nature of a p-n junction allows for current to flow in one direction when a bias is applied due to the depletion region and built in voltage. For example, forward bias can occur when a voltage is supplied across the p-n junction which decreases the formed electric field. Therefore, in dark conditions a solar cell demonstrates the same characteristic behaviour as a diode.

In thermal equilibrium, we assume that the doping concentration in the depleted region and the majority carrier density are equal. Using the law of mass action, V_{bi} can be expressed as following:

$$V_{bi} = \frac{kT}{q} ln \frac{p_{p0} n_{n0}}{n_i^2}. \tag{2.33}$$

Where p_{p0} is the equilibrium density of holes in the p-type semiconductor and n_{n0} is the density of electrons in the n-type semiconductor. Rearranging Equation 2.33 results in an expression for both hole density and electron density:

$$p_{p0} = p_{n0} \exp(\frac{qV_{bi}}{kT}), \tag{2.34}$$

$$n_{n0} = n_{p0} \exp(\frac{qV_{bi}}{kT}). \tag{2.35}$$

When a bias voltage V is applied, the equation for both electron and hole density can be written as Equations 2.36 and 2.37. When applying a voltage, it is assumed, under

these conditions that the carrier density of the holes and electrons demonstrate the same behaviour with V_{bi} as that of the zero bias case.

$$p_p = p_n \exp(\frac{q(V_{bi} - V)}{kT}), \tag{2.36}$$

$$n_n = n_p \exp(\frac{q(V_{bi} - V)}{kT}) \tag{2.37}$$

where n_n and n_p are the carrier densities at the boundaries of the depletion region at the n-type side and the p-type side respectively. Similarly, p_p and p_n is the hole density at either side of the depletion region. Assuming p_p=p_{p0}, the injected carriers have no influence on the majority carrier density. Equations 2.35 and 2.34 can therefore be simplified using Equations 2.37 and 2.36 to give Equations 2.38 and 2.39

$$p_n = p_{n0} \exp(\frac{qv}{kT}), \tag{2.38}$$

$$n_p = n_{p0} \exp(\frac{qv}{kT}). \tag{2.39}$$

The majority carrier density under non equilibrium conditions flowing through depletion region or built in region is a function of the bias voltage. Assuming the generated current within the depletion region is zero, which is the optimal configuration, the steady state continuity equation is derived as:

$$\frac{d^2 p_n}{dx^2} - \frac{p_n - p_{n0}}{D_p \tau_p} = 0. \tag{2.40}$$

Where D_p is the is the diffusion coefficient and τ_p is the lifetime of the carrier, which in this case is holes. The general solution is obtained using Equation 2.38 as the boundary conditions

$$p_n - p_{p0} = p_{n0}(\exp(\frac{qV}{kT} - 1) \exp(\frac{-x - x_n}{L_p}). \tag{2.41}$$

Here L_p is the carrier diffusion length and can be obtained from D_p and τ_p Equation 2.42,

$$L_p = \sqrt{D_p \tau_p}. \tag{2.42}$$

When x=x_n, the current density from hole diffusion J_p at the n-type material boundary is given in Equation 2.43. Similarly the electron diffusion current on the p-type material boundary is obtained using Equation 2.44 when x=-x_p,

$$J_p = \frac{qD_p p_{n0}}{L_p}(\exp(\frac{qV}{kT}) - 1), \tag{2.43}$$

$$J_n = \frac{qD_n n_{p0}}{L_n}(\exp(\frac{qV}{kT}) - 1). \tag{2.44}$$

The total current density through the device therefore is obtained by summing J_p and J_n in Equation 2.45

$$J = (\frac{qD_n n_{p0}}{L_n} + \frac{qD_n p_{n0}}{L_p})(\exp(\frac{qV}{kT}) - 1). \tag{2.45}$$

Simplifying this equation, the first term is known as the saturation current density J_0, yielding Equation 2.46

$$J = J_0(\exp(\frac{qV}{kT}) - 1). \tag{2.46}$$

The current density exponentially increases with an increasing bias voltage arising from the p-type material. The current saturates under reverse applied bias to J_0, allowing it to be an accurate approximation of the recombination in the device.

2.5.2 Solar Cell under Illumination

When photons are incident on a solar cell, electron hole pairs are generated converting the incident solar energy into electrical energy. The strong electric field created from the p-n junction separates the generated carriers and forms a continuous current, known as light generated current or photocurrent J_L. The equivalent circuit of this process is given in Figure 2.8.

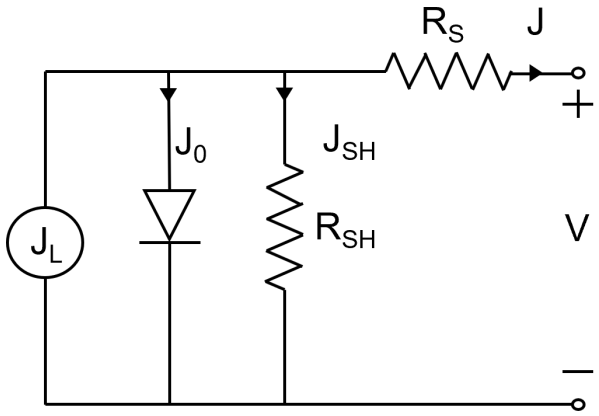

Figure 2.8: Circuit diagram equivalent of a solar cell with incident light.

When irradiated, the current density curve from an applied bias voltage shifts as J_L flows opposite to J_0. From Equation 2.46, under an applied forward bias the total current of the solar cell device with incident light is obtained using Equation 2.47.

$$J = J_0(\exp(\frac{qV}{nkT}) - 1) - J_L \tag{2.47}$$

where included here, is the diode ideality factor n. The diode ideality factor lies between 1 and 2 for most semiconductor devices and is equal to 1 in an ideal diode junction. The

voltage across the device can be obtained by rearranging Equation 2.47 yielding Equation 2.48

$$V = \frac{nkT}{q} ln(\frac{J_L + J}{J_0} + 1). \tag{2.48}$$

Solar Cell Parameters

The key solar cell parameters are defined as, the short circuit current density J_{sc}, the open circuit voltage V_{oc}, Fill Factor FF and efficiency η. J_{sc} is defined as the current through the cell when no voltage is applied. In an ideal solar cell, J_{sc}=J_L but in a non-ideal case, can be obtained by setting V=0 in Equation 2.47. Similarly, V_{oc} is the applied voltage resultant in no net current in the solar cell and can be calculated by setting the current equal to zero, yielding Equation 2.49:

$$V_{oc} = \frac{nkT}{q} \ln(\frac{J_L}{J_0} + 1). \tag{2.49}$$

The FF of a solar cell is defined as the ratio of the product of J_{sc} and V_{oc} and the maximum power density produced from the solar cell. The maximum power density point of the solar cell is obtained by setting $dJ/dV = 0$, resulting in a maximum voltage for maximum power V_{mp} and similarly a maximum current J_{mp}. The FF is therefore calculated using Equation 2.50:

$$FF = \frac{J_{mp} V_{mp}}{J_{sc} V_{oc}}. \tag{2.50}$$

The efficiency η of the solar cell calculated from the ratio of the power output from the device to the power input. The power into the device is the incident light power density P_s.

$$\eta = \frac{J_{sc} V_{oc} FF}{P_s}. \tag{2.51}$$

In practical examples, η and FF are lowered by dissipation of power due to internal resistances shown in Figure 2.8. Two resistances are introduced, the series resistance R_S and shunt resistance R_{SH}. In an ideal device, R_S=0 where R_{SH}=∞. R_S arises from the resistance of the current moving through the semiconductor material and the Schottky barrier formed between the semiconductor material and the metal contacts. The series resistance can be determined from the solar cell current density-voltage (JV) curve from the slope at V_{oc}. The shunt resistance of the device is commonly incident from manufacturing defects that cause current leakage or shunting, it is obtained from the slope of the JV curve at J_{sc}. Equation 2.47 can be rewritten, taking the parasitic resistances into consideration as

Equation 2.52

$$J = J_0(\exp(\frac{q(V - JR_S)}{nkT}) - 1) - J_L + (\frac{V - JR_S}{R_{SH}}). \tag{2.52}$$

Standard Illumination

When measuring solar cells experimentally, a standard air mass (AM) and illumination is used for comparison purposes. The solar constant has a value of 1000 Wm^{-2} and is defined as the intensity of solar radiation at an average distance from the sun to the earth [44]. The angle at which the sun hits the earth however, varies due to scattering and attenuation. This is defined as the AM. The average spectrum of light incident on the earths surface is AM 1.5 at the mid latitudes. This is, therefore, taken as a standard angle in which light from the sun travels and is used as a baseline for solar cell measurements.

2.6 Kesterite Material Properties and Solar Cells

2.6.1 History of CZTSSe Solar Cells

CZTS attracted attention as a photovoltaic absorber comprising of earth abundant and low cost elements with the addition of its similarity to CIGS, which has demonstrated a high PCE and significant progress. The atomic arrangement of CZTS is therefore the same as CIGS, replacing Ga cations with Sn cations and similarly In with Sn. The potential of CZTS was first reported by Shinshu University in 1988 who demonstrates an absorption coefficient of 3.8×10^4 cm^{-1} with a band gap value of 1.45 eV [45]. Arising from this, extensive research began into kesterite materials. The first CZTS device was fabricated using electron beam evaporation for thin film deposition followed by sulphurisation of the film. The devices yielded a PCE of 0.66% with a band gap of 1.5 eV [46]. Currently, the record CZTSSe solar cell demonstrates a PCE of 12.6% fabricated using a hydrazine solution approach [16].

2.6.2 Crystal Structure and Electronic Properties

CZTS crystallises in a tetragonal structure. In this structure, each sulphur anion is bonded to four cations and likewise a cation is bonded to 4 sulphur anions. The atomic packing in the crystal structures has different symmetries, causing a range of space groups in

the structures. CZTS films are found in 6 phases; kesterite, stanite, wurzite, eskbornite, PMCA and spalerite, illustrated in Figure 2.9 [47–52]. The most desirable phase for solar cell application is kesterite phase, shown to be the most stable [53] and is defined by alternate cation layers of CuSn/CuZn at z= 0, 1/4, 1/2 and 3/4 [54]. The stannite phase is the closest relation to the kesterite phase with the difference in alternate ZnSn and CuZn layers with zinc ions at z=0 and 1/2 and copper ions at z=1/4 and 3/4. Although kesterite and stannite have varying energy, they cannot be distinguished using X-Ray diffraction alone, but can be observed by neutron diffraction. Neutron diffraction shows that CZTS most commonly crystallises in a disordered kesterite structure [55]. The disorder arises from a mix of the Cu and Zn sites and therefore it is assumed that stannite structures are more likely partially disordered kesterite [56, 57]. The phase that the thin film CZTS forms changes the material band gap and the respective band gap energies. For each phase, the band gap variations are shown in Table 2.1 [58–61].

Considering band gap energy fluctuations from disordering in the fabrication process, the band gap ranges for kesterite CZTS lie within 1.4-1.6 eV [62]. The Shockley-Quessier limit states that a single junction solar cell can reach a PCE of 33% [37]. Kesterite CZTS has a near optimum energy band gap for over 30% efficiency at 1.5 eV. In addition to the close to ideal energy band gap, kesterite has a high absorption coefficient of $\sim 10^4$ cm^{-1} [13, 63]. This enables sufficient light absorption with material only a few microns thick and therefore reducing the device manufacturing cost [64, 65].

Table 2.1: Band gap variations of CZTS thin films with various crystal structures [47–52].

Structure	Band gap (eV)
Kesterite	1.56
Stannite	1.42
Eskebornite	1.46
PMCA	1.21
Wurzite	1.4

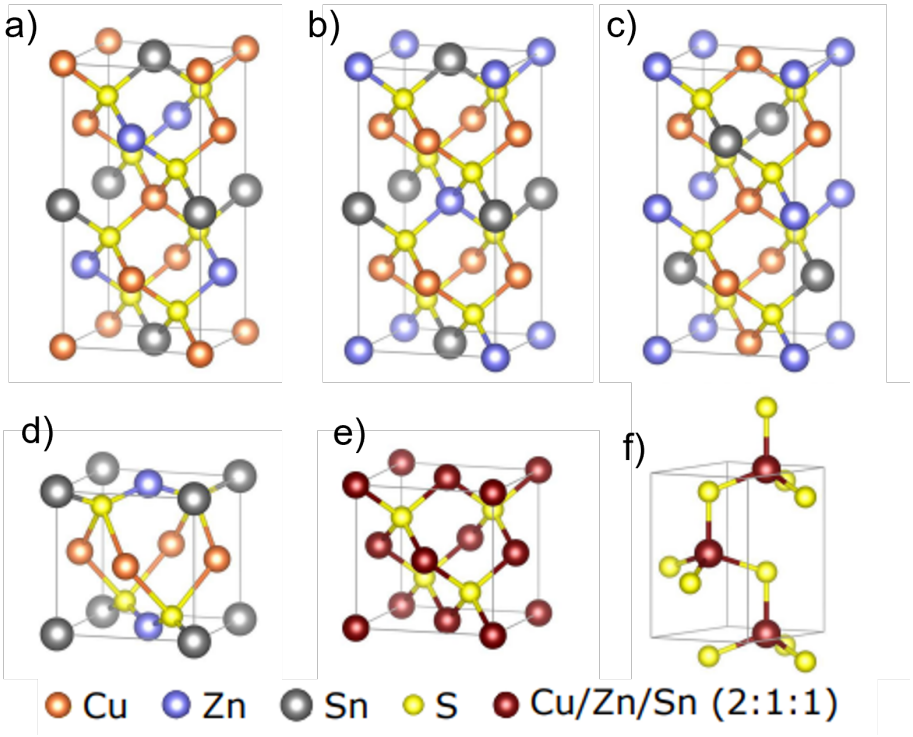

Figure 2.9: Crystal structure of a) kesterite b) stannite c) eskebornite d) PMCA e) sphalerite and f) wurzite phases of CZTS thin films [47–52].

2.6.3 Loss Mechanisms

In comparison to other thin film materials, such as CIGS and CdTe, CZTS demonstrates a more significant V_{oc} deficit. One of the contributing factors to this is the formation of defect clusters in CZTS [66–70]. Antisite defect Cu_{Zn} forms when copper atoms occupy the zinc lattice sites which, due to the similar atomic radii, has low formation energy [71]. The Cu_{Zn} defect dominates in Cu-rich Zn-poor composition conditions. To avoid losses caused by the defect, a Cu-poor Zn-rich composition is favourable for CZTSSe devices [72–74]. The presence of the antisite defects near the conduction band and valence band edges of the material cause band gap fluctuations. This causes band tailing in the material which results in a lower V_{oc} [75]. Additionally, Cu_{Zn} defects can cause Fermi level pinning, where the semiconductor material undergoes band bending allowing the Fermi level to become independent of the metal contact, regardless of the work function [76]. This, creates a barrier for electron hole pairs through band bending due to a deep acceptor level formed in the band gap [12]. CZTSSe has a high possibility of defects and exhibits intrinsic p-type doping as a result of the different defects present in the material.

In addition to the aforementioned defects, some deep level defects lie in the centre of the band gap where SRH recombination is at a maximum [77]. Deep defects in CZTS have been identified at around 0.5 and 0.8 eV above the VBM [78, 79].

Grain Boundaries

An additional contributing factor to the low V_{oc} in CZTSSe cells is defects and recombination centres found at grain boundaries (GB). The effect of GB in kesterite devices is not yet fully understood but have been shown to promote recombination centres [80]. An explanation for this is, GB's cause an upwards and downwards bending in the conduction and valence band respectively which creates a strong depletion region due to repulsion of electrons by the upward band bending, and repulsion of holes by the downwards band bending, reducing recombination at the grain boundaries. Liu *et al.* observe that grain boundaries present in CZTSSe act as electron flow channels rather than recombination centres. But, also report sodium passivisation of the GB and a resultant increase in V_{oc} [12].

2.6.4 Fabrication of CZTS

When fabricating CZTS films, there is a small window to achieve the desired phase chemistry due to the large number of secondary phases [81]. There are a wide variety of techniques used to fabricate CZTS, including sputtering, chemical vapour deposition, chemical bath deposition, solution processing of molecular precursors, co-evaporation, pulsed laser deposition and hot injection of metallic precursors in surfactant [11]. Each method demonstrates advantages and specialism in, for example, grain growth, stoichiometry and purity. These deposition methods are based mainly on either vacuum or solution based processes. Vacuum techniques demonstrate an advantage in the repeatability of the films, specifically with regards to composition. However, vacuum based processes require significant energy input and are a costly method of fabrication. Alternatively, solution based processes provide a lower energy and cheaper solution. The majority of solution based methods, mainly those that achieve high efficiency devices, rely on the use of hydrazine which is an toxic solvent. Elimination of this solvent, to produce CZTS through a low cost, low energy and low toxic route, is achieved using of hot injection of metallic pre-

cursors to create nanoparticle inks. Fabrication through nanoparticle inks demonstrate advantages for phase stability, as the desired phase can be achieved before the film deposition. The kesterite structure can be easily achieved through careful control of the CZTS nanoparticles reaction [82]. Kesterite nanoparticles are formed within the liquid itself, allowing a thermodynamic stability to be achieved in the early stages of fabrication. This results in the nanoparticle ink method producing a reliable and achievable CZTS photovoltaic absorber layers.

Chapter 3

Experimental Methodology

3.1 Solar Cell Fabrication

Kesterite solar cells were fabricated from solution-based nanoparticle inks to create a p-type CZTSSe absorber layer. Solar cell devices were completed in substrate configuration with the structure: substrate (Mo Foil or SLG)/Mo/CZTSSe/Cadmium Sulphide (CdS)/Zinc Oxide (ZnO)/Indium Tin Oxide (ITO)/Nickel and Aluminium contacts. The devices were then characterised using a range of techniques outlined within this chapter.

3.1.1 Substrate Preparation

For the rigid solar cells fabricated as reference devices, SLG (Thermo Scientific) was the chosen substrate. The flexible devices were fabricated on Mo Foil (99.99% Sigma Aldrich) with thickness of 0.05 mm. Mo foil was chosen due to its thermal stability with a coefficient of thermal expansion 5.5×10^{-6} K^{-1}, providing a robust material during high temperature fabrication steps, and high conductivity [83].

To prepare the substrates, each slide was brushed using a solution of 20% Decon 90 and 80% de-ionised water (DI water). The brushing was completed in circular motions up and down the substrate before rinsing in DI water to remove any of the cleaning solution. This cleaning step was then repeated before the samples were sonicated in an ultrasonic bath in a solution of 5% Decon 90 and 95% DI water for 15 minutes. The samples were again rinsed in DI water and two sequential ultrasonic cleaning steps implemented using acetone and iscopropanol (IPA) respectively for 15 minutes each. The samples were then dried in nitrogen (N_2) to remove any contaminants.

A thin layer of Mo was sputtered onto the substrate as the back contact material and to improve adhesion between the substrate and the CZTSSe absorber layer. In addition to this, sputtering a layer of Mo onto the Mo foil before absorber deposition improves the shunt resistance of the final solar cell device [84]. Using a Teer Coatings UDP 350 magnetron sputtering system a Mo layer was deposited by direct current (DC) sputtering. The samples were loaded vertically into the chamber parallel to the target alongside a glass slide with a portion covered for film thickness analysis, and left for 12 hours to reach a base pressure of 6×10^{-6} mbar. A 20 minute cleaning treatment was used to clean the surface of the target pre sputter. The sputtering process of Mo was completed at room temperature under 1.5×10^{-2} mbar of pressure in Ar (70.1 sccm) at 750 W with a direct current of 3 A. Mo was coated onto the substrate by varying the deposition time to achieve a desired thickness. Measuring the coating rate in the same conditions yielded a deposition rate of 25 nm/min, allowing the deposition time to be changed to 40 minutes to deposit a 1 μm Mo layer. Using a Bruker DektakXT stylus profiler, the thickness of the Mo was calculated by moving the stylus over the glass Mo boundary multiple times and calculating average. The resistivity (ρ) of the Mo was measured using a Janedel 4-point probe setup and a Kiethley 2600 series source meter. The resistivity was calculated using Equations 3.1 and 3.2;

$$Thickness \cdot R_s = \rho, \tag{3.1}$$

$$\frac{\pi}{\ln 2} \cdot \frac{dV}{dI} = R_s \tag{3.2}$$

where R_S is the sheet resistance.

3.1.2 Nanoparticle Ink Fabrication

Fabrication of CZTS nanoparticle inks was completed using the metallic cation precursors: copper(II) acetylacetonate ($Cu(C_5H_7O_2)_2$, 99.99% Sigma Aldrich), zinc (II) acetylacetonate ($Zn(C_5H_7O_2)_2$, 99.995% Sigma Aldrich) and tin(IV) bis(acetylacetonate) dichloride ($Sn(CH_7O_2)_2Cl_2$, 98% Sigma Aldrich). Elemental sulphur (S, 99.98% Sigma Aldrich) was used as the anion precursor. To prevent aggregation and enable dispersion of the fabricated nanoparticles, oleylamine (OLA, $CH(CH_{-2})_{-8}NH_2$, Sigma Aldrich) was used as the solvent and surfactant in this method [85]. The quantities of the chemicals were chosen to yield precursor molar ratios of Cu/(Zn+Sn)=0.79 and Zn/Sn=1.27. The quantities used were varied slightly throughout the project to obtain ratios repeatably

within the desired range of Cu/(Zn+Sn)=0.75 to 0.85 [86]. The precursor masses used to achieve this were Cu=300, Zn=250 and Sn=285 mg. The three metallic precursors were mixed with 10 ml OLA in a three neck glass flask shown in Figure 3.1. 1 M sulphur in 10 ml OLA was prepared into a separate three neck flask. Both solutions were heated to 70 °C to allow the precursor materials to dissolve and then degassed to ensure the system was air tight.

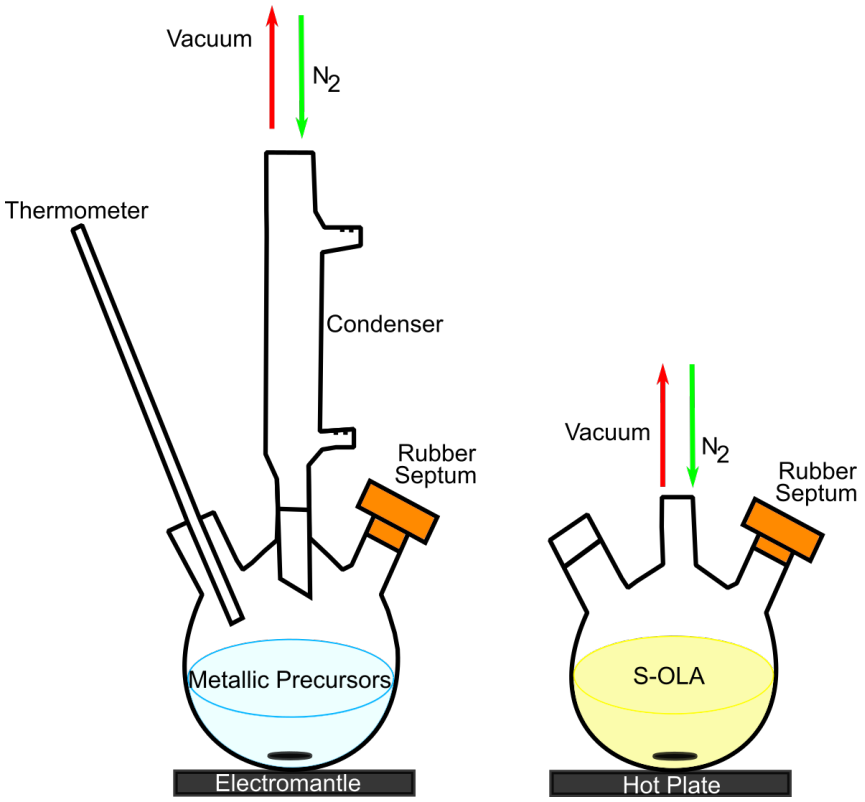

Figure 3.1: Precursor materials in OLA mixed into three neck flasks for nanoparticle ink synthesis.

Once a low vacuum was established (< 1 mbar), two vacuum and purge routines were implemented. Initially, the metallic precursors were stable at 100 °C, and the sulphur at 70 °C. A 15 minute degas and a 15 minute purge in N_2 was then completed. For the second iteration of the routine, the metallic precursors were stabilised at 200 °C while the sulphur was allowed to cool to room temperature for the injection. The vacuum step was repeated until boiling was observed in the metallic surfactant. Once boiling, the vacuum was held for a further 5 minutes to remove any remaining O_2 and impurities and then purged with N_2. The N_2 was held constant throughout the reaction process. The cation

precursor solution was heated to 225 °C before 3 ml of S-OLA was injected just above the surface. The solution was heated once again to 225 °C as S was injected at room temperature thus lowering the overall solution temperature. Once at 225 °C, the temperature was held constant for 30 minutes for the reaction to occur. The CZTS solution was then left to cool in ambient lab conditions under N_2 until below 70 °C. Using this method, specifically the time and temperature, ensures that the nanoparticles are of the desired kesterite phase [82].

To separate and purify the fabricated CZTS nanoparticles from any unreacted residuals, 5 ml of Toluene (Sigma Aldrich) and 20 ml of IPA was added. Toluene is used to absorb the nanoparticles and IPA to condense them. The mixture was decanted into two centrifuge tubes and subject to a centrifuge step at 8500 rpm for 10 minutes, separating the nanoparticles from the solution and large agglomerates. The liquid was discarded and the nanoparticles dispersed in 10 ml toluene and sonicated in an ultra sonic bath for 10 minutes. Repeating this process of centrifuging the ink in 20 ml of IPA and then dispersing in toluene further removed large agglomerates and unwanted bi-products. Finally, the nanoparticle inks were dispersed and subject to a final centrifuge step at 7000 rpm for 3 minutes to achieve fine nanoparticles suspended in IPA.

The collected ink containing the fine nanoparticles was subject to a final centrifuge step at 8450 rpm for 10 minutes with 25 ml of IPA, to condense the inks for further concentration. The nanoparticles collected were dissolved in 1.5 ml of 1-Hexanethoil (95% Sigma Aldrich) and sonicated for 30 minutes to ensure the nanoparticles were fully dispersed. The nanoparticle inks were then passed through a 1 μm Whatman syringe filter to remove any large agglomerates yielding a final concentration of 100 mg/ml.

3.1.3 Ink Deposition

CZTS nanoparticle inks were deposited using two methods in this work, spin coating and slot die coating, to achieve a CZTS precursor thin film layer.

Spin Coating

Prior to depositing the ink, the substrate was first cleaned, achieved by two simultaneous clean runs of IPA and DI water in the ultra sonic bath for 15 minutes. The samples were

dried under a compressed N_2 gun. The substrates were cut into 25×25 mm^2 squares and loaded onto the spin coater. Using a micro-pipette, 30 µl of ink was dropped onto the centre of the substrate followed by spinning for 3-5 seconds at 1200 rpm. The sample was subject to a soft baking process of 150 °C for 30 seconds then 300 °C for 30 seconds. This removes any remaining surfactants from the surface of the sample and prevents shock from a sudden temperature increase. These steps were repeated 10 times to obtain a film thickness of $\sim$ 1 µm of densely packed uniform nanoparticles, shown in Figure 3.2a. This process was identical for both SLG and Mo foil cell fabrication.

Slot Die Coating

Slot die deposition was completed on substrates 25×75 mm^2. The surface is required to be flat for control over ink thickness, which demands Mo foil samples to be mounted onto a glass slide to remove any curvature. The substrate was loaded onto the slot dye coater (Ossila) with a 'coat hanger' head manifold. A uniform and densely packed CZTS nanoparticle precursor was achieved by depositing 4 sequential layers with a substrate speed of 40 mm/s and a ink feed speed of 18.2 µl/s where each individual layer yields a thickness of $\sim$ 200 nm. The substrate was heated to 80 °C during deposition to evaporate any residual solvent and baked at 300 °C in air on a precision hotplate between successive layers. The resultant thin films are shown in Figure 3.2b.

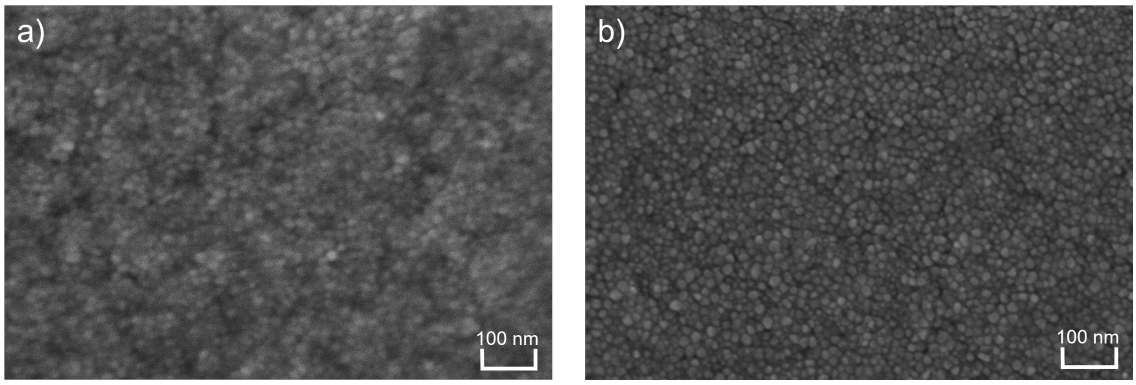

Figure 3.2: CZTS nanoparticles deposited using a) spin coating and b) slot die coating.

3.1.4 Selenisation

Selenisation is the process in which the nanoparticles undergo recrystallisation forming large, compact, uniform grains required for efficient light absorption. Reacting the CZTS

thin films in a Se-rich atmosphere induces large grain growth as S and Se undergo anion exchange forming a sulfoselenide regime.

300 mg of selenium pellets (Se, 99.99% trace metal basis Sigma Aldrich) were loaded into a small channel in a graphite cylinder (tube). The as-deposited thin film was then placed directly above this channel, face down within the tube. The graphite box was then sealed and loaded into a tube furnace to undergo annealing. The furnace was evacuated to 6×10^{-3} mbar completed by three vacuum and purge steps with Ar to remove any residual O_2, and then back filled with Ar to a pressure of 9.5 mbar. The temperature was increased from room temperature to the desired selenisation temperature of 500 °C at a continuous rate of 20 °C per minute. The furnace was then held constant at 500 °C for 20 minutes for selenisation to occur [87]. The samples were then fan cooled rapidly within the furnace before being removed when below 40 °C. The resultant films were densely packed uniform CZTSSe grains as seen in Figure 3.3, with a thickness of 1-2 μm. From Figure 3.3a, the average grain size is 850 nm which shows significant growth on the nanoparticles presented previously, which have an average diameter of 10-20 nm. The characteristic bi layer structure was also observed in CZTSSe cells fabricated from nanoparticle inks (Figure 3.3b). The bi-layer structure is comprised of a carbon-rich fine grain layer with a larger CZTSSe grain structure above, resultant of the nanoparticle ink synthesis method [84].

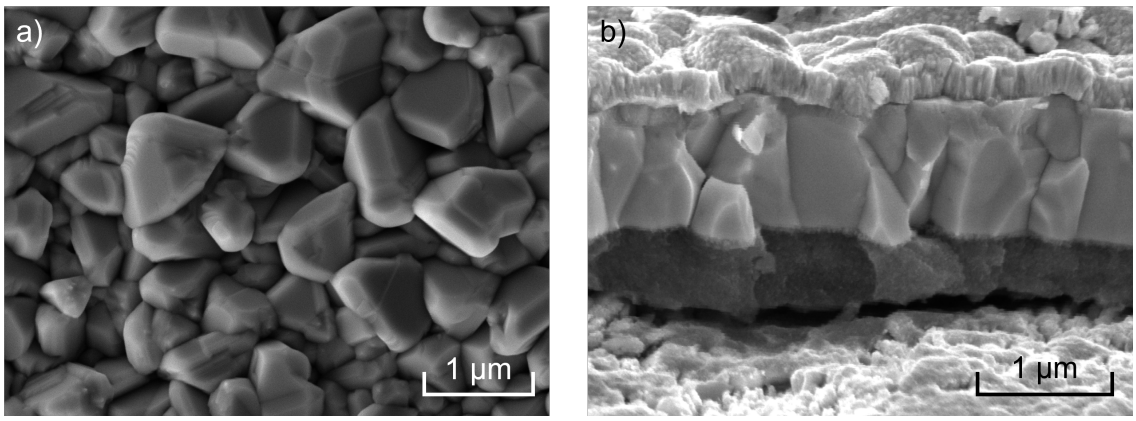

Figure 3.3: a) Top down morphology of a CZTS absorber layer and b) cross sectional images of CZTSSe thin film device fabricated from selenisation of CZTS nanoparticle inks deposited by spin coating.

3.1.5 Chemical Bath Deposition

To fabricate a p-n junction outlined in Section 2.4, a n-type buffer layer is required. Typically, in CZTSSe, CIGS and CdTe solar cells, the chosen buffer layer is CdS. This is due to its high electron mobility and high band gap of 2.4 eV [88–90]. In this work chemical bath deposition (CBD) was used to deposit a thin CdS buffer layer onto the CZTSSe absorber. The benefits of this include appropriate growth conditions for consistent thin layer and the energy required for the process is low intensity. To control the reaction temperature, a double walled beaker was connected to a water bath and set to 70 °C. 318.6 ml of DI water was added to the beaker alongside a magnetic stirrer and the solution was stirred constantly and allowed to heat to 70 °C. 144.6 mg of $CdSO_4$(Sigma Aldrich) was added to the DI water and left to dissolve for 1 minute before adding 36 ml of 28% ammonium hydroxide (NH_4OH, Sigma Aldrich). The NH_4OH is used to control the pH of the solution in the desired range of 10.8-11. At this point, the samples were added vertically into the centre of the beaker using a sample holder. 355.9 mg of thiourea (CH_4N_2S, Sigma Aldrich) was added as the sulphur source creating CdS. The reaction was held for 20 minutes to obtain a 70 nm layer of CdS on the surface of the samples. After the deposition, the samples are rinsed in DI water and dried in N_2 before annealing in air at
200 °C for 10 minutes.

3.1.6 CO_2 'Snow' Jet

CO_2 'snow' jet cleaning involves the high pressure expansion of CO_2 forming 'snow' which can be used to clean the surface of both the CTZSSe absorber layer and the CdS layer post deposition. During this work the use of a 'snow' jet cleaning step was evaluated. The snow jet cleaning method has been reported to not only remove particles such as dust from the CdS interface, but also agglomerates formed during the CBD process [91]. The impact on the pressurised 'snow' jet stream and interaction between particles and contamination result in particulate removal.

To evaluate this procedure, two solar cell devices were fabricated, one with CO_2 cleaning post buffer layer deposition and one without. The optoelectronic properties can be seen in Table 3.1. The average cell efficiency of the devices was improved by an absolute value of 0.86% with cleaning and therefore completed on all sequential device batches. The CO_2 cleaning step was completed by initially loading the sample post CdS deposition onto a

hot plate to evaporate any forming condensation. The CO_2 canister is fitted with a nozzle and run across the surface of the sample for 1 minute.

Table 3.1: Impact of CO_2 cleaning on optoelectronic properties of completed CZTSSe solar cells.

	V_{oc} (mV)	J_{sc} (mA/cm^2)	FF (%)	η (%)	Rs (Ωcm^2)	Rsh (Ωcm^2)
No CO_2	260	29.1	47.8	3.6	3.2	46.2
CO_2	270	33.0	50.2	4.5	2.9	61.3

3.1.7 Window Layer Deposition using Direct Magnetron Sputtering

Two window layers are utilised within this work, intrinsically doped zinc oxide (i-ZnO) and indium tin oxide (ITO) which are deposited using magnetron sputtering (Teer Coatings UDP 350). Using magnetron sputtering allows for deposition of high purity layers with good coverage on rough surfaces, high adhesion and good uniformity [92].

The i-ZnO layer was first deposited using pulse DC magnetron sputtering. The samples were loaded vertically into the teer coating system and evacuated to a base pressure of 6×10^{-6} mbar. A 20 minute pre-sputtering cleaning step was used to clean the target (99.99% ZnO) before a 35 minute deposition at room temperature. The deposition was completed at a plasma pressure of 2×10^{-6} mbar in an Ar:O_2 mix of 35:1 sccm at 600 W and 2 A with a rotation of 5 rpm to create a homogeneous film of 50 nm thickness.

ITO was then deposited sequentially using RF sputtering without opening the chamber of the system. The target (In_2O_3/SnO_3 99.99%) was cleaned using a 20 minute plasma clean before the chamber was heated to 150 °C for a 200 nm ITO deposition. The deposition was completed at 200 W for 90 minutes with substrate rotation at 5 rpm in Ar (70.1 sccm). The system was then cooled before the samples removed.

3.1.8 Deposition of Electrical Contacts using Electron Beam Evaporation

Deposition of the front electrical contact grid was achieved using electron beam (EB) evaporation. An electron beam is generated from passing a current through tungsten filament. High voltage was applied between the filament and crucible housing the metallic source to accelerate the electrons. Once the beam is incident on the material, it vaporises the metal in the crucible, the metal is then deposited onto the surface of the samples held within the chamber. This allows for a high deposition rate and low contamination of the sources. The samples were mounted into a holder with designed shadow masks for the grid pattern desired shown in Figure 3.4. The EB evaporator used was the Moorfield Minilab 080, this machine allowed the samples to be loaded into a smaller chamber first and evacuated before moving into the deposition chamber, avoiding contaminants in the main deposition chamber. The loading chamber was evacuated to a pressure below 1×10^{-5} mbar before transferring the samples into the deposition chamber at a pressure of 5×10^{-7} mbar and rotating them at 10 rpm. The electron beam was then focused onto the centre of the source material in the crucible, using a magnetic field to control the movement, to eliminate any residual oxides on the surface before the deposition. Nickel (Ni) and aluminium (Al) were deposited as front contacts. 50 nm of Ni was deposited first at a rate of 1 Å/s then 1 μm of Al at a deposition rate of 0.5 Å/s. The thickness of the material was measured via a crystal quality monitor present in the deposition chamber.

3.1.9 Scribing

Solar cell devices were scribed using a mechanical scriber to yield 9 devices per substrate each with an area of 0.16 cm^2. Following deposition of the front contacts using EB, a single back contact was created by removing all device layers on one side of the sample, shown in Figure 3.4. The substrate has a Mo(S,Se) layer, which has high resistance; not desired at the back contact. This layer was removed by scrubbing with alumina micro polish. Silver paint was then added to the created back contact to increase conductivity. The final devices can be seen in Figure 3.4.

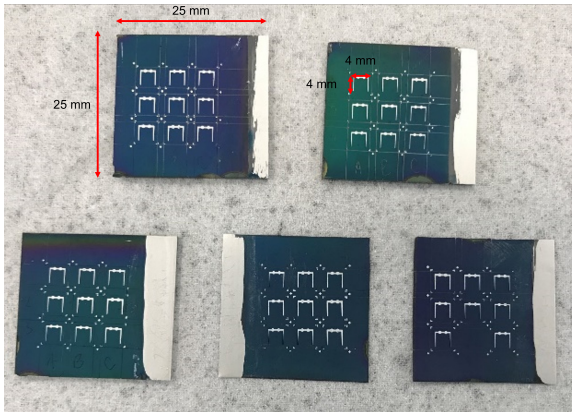

Figure 3.4: Complete CZTSSe solar cell devices.

Fabricating the solar cell devices in this way yields 9 devices per substrate. When the devices are measured, using a variety of techniques either the average across the 9 devices is reported or the champion (best performing device). Once measured using the solar simulator (see Section 3.2.3) the champion device is identified and can be plotted and used for further analysis. Another aspect to consider, is the small loss in active area from the Ni/Al contacts. The area lost, is calculated to be 7.97% of the total cell area. When calculating area based parameters, such as J_{sc}, this is considered but can be directly compared to J_{sc} obtained from External Quantum Efficiency (EQE) spectra (Section 3.2.4), which eliminates this loss in active are by obtaining the quantum efficiency from a small laser point on the device. Finally, when using this contact architecture, shadowing can occur during the measurement process from the probes. This shadowing is eliminated as much as possible but cannot be eliminated for JV measurements so contributes to a almost negligible loss, but does not contribute any losses again with EQE measurements.

3.2 Characterisation

3.2.1 Scanning Electron Microscopy (SEM) and Energy Dispersive X-ray Spectroscopy (EDS)

Surface morphology and cross sectional images were taken using a Tescan MIRA 3 scanning electron microscope, a system featuring a high brightness Schottky emitter allowing high resolution low noise images [93]. An electron beam is emitted from an electron gun and passed through a number of lenses to create a focused beam that hits the surface of the

loaded sample. The beam interacts with the atoms on the surface of the sample, causing various forms of radiation to be emitted, shown in Figure 3.5. For topographic images, the secondary electrons (SE) emitted are used due to their low energy and low travel distance from the sample to the detector [94]. For CTZSSe absorber morphology imaging, the In-Beam detector was used with a working distance of $\sim$ 15 mm with a accelerating beam voltage of 10 kV. The beam spot size was also minimised to capture sharp topographical features.

The Tescan MIRA 3 scanning electron microscope is also fitted with EDS from Oxford Instruments (X-Max). Once the electron beam is incident on the sample, X-rays of various energies are emitted from the sample and used to determine the elemental composition. Each element produces an emission spectra according to its atomic structure [94]. The EDS was collected using a detector operating in dark conditions to eliminate interference. A working distance of 15 mm was used with an accelerating voltage of 20 kV to observe the characteristic radiated X-rays. For elemental mapping, EDS line scans were used with a lower accelerating voltage of 10 kV with a 10 mm working distance.

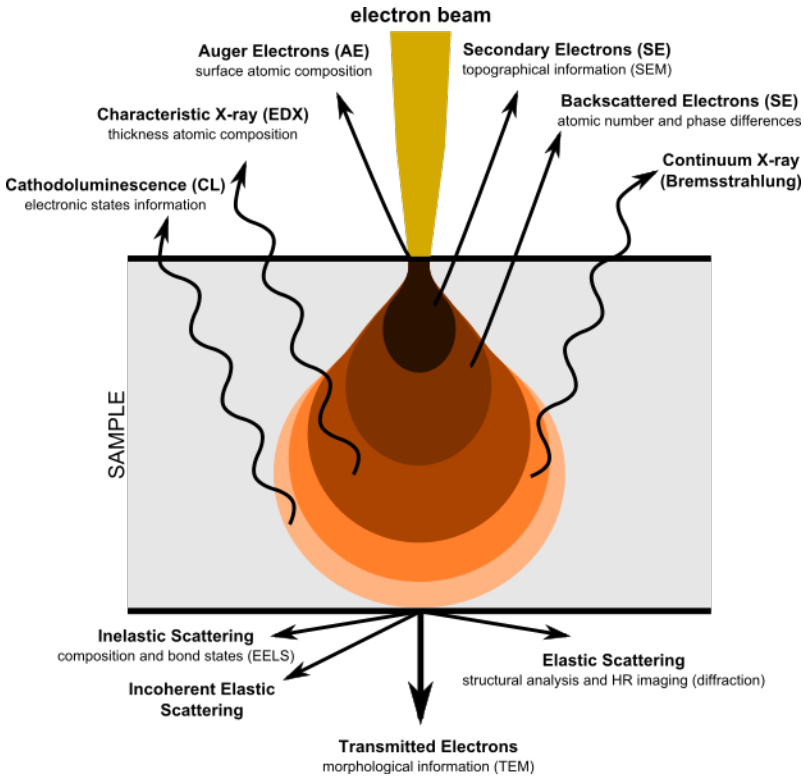

Figure 3.5: Interaction of electrons with matter showing the incident beam and the radiation given off from interaction with the sample surface [95].

3.2.2 Secondary Ion Mass Spectroscopy (SIMS)

SIMS is a technique used to analyse the composition of a thin film by subjecting the surface to a focused ion beam and collecting secondary ions radiated from the sample. The mass-to-charge ratio of the ejected ions determines the elemental composition of the surface [96]. Elemental depth profiles were achieved through SIMS using a Hiden Analytical gas ion gun and quadruple detector. A primary Ar^+ ion beam at an energy of 4 keV was focused on the surface of the sample to collect ejected secondary ions.

3.2.3 Current Density-Voltage (JV)

Current density-voltage measurements were used to observe the electrical properties of CZTSSe solar cell devices. The JV characteristics were measured under standard AM 1.5 and illumination (100 $mWcm^{-2}$) using an Abet Technologies Sun 2000 solar simulator. The irradiance was calibrated using a certified Si solar cell as a reference sample. The sample was loaded into a mount and measured using a 4 point probe configuration. A Kiethley 2400 source meter was used to apply a voltage sweep from -0.5 V to 0.5 V measuring the current with a compliance of 0.1 A. From the JV measurements, V_{oc}, J_{sc}, FF, η, R_S and R_{SH} were determined.

3.2.4 External Quantum Efficiency (EQE)

EQE is defined as the ratio of the carriers collected at a given energy, to the number of photons incident at that same energy. EQE is a measure of the absorption of the incident light on the active area of a device alongside the collection of charges once electron-hole pairs are generated. Obtaining EQE spectra from a solar cell device enables absorption to be identified in the different layers of the cell alongside defects and recombination and J_{sc} to be obtained with no shadowing or contact active area loss. EQE measurements were performed using a Bentham instruments TM300 double grating monochromator and chopped light source. CZTSSe solar cell devices were measured in dark conditions in 5 nm increments from 400 nm to 1400 nm after calibration using certified Si and Ge photo-diodes. From EQE analysis, the internal quantum efficiency (IQE), defined as the ratio of charge carriers collected by the cell to the absorbed photons in the semiconductor material, can be determined using Equation 3.3 alongside J_{sc} using Equation 3.4.

$$IQE(\lambda) = \frac{EQE(\lambda)}{1 - R(\lambda)}, \tag{3.3}$$

$$J_{sc} = \Sigma(F(\lambda) \cdot \lambda \cdot EQE(\lambda)) \cdot (\frac{\Delta\lambda}{hc} \cdot q) \tag{3.4}$$

where F is the standard AM 1.5 spectrum.

EQE Modelling

Modelling a solar cell EQE device spectra enables extraction of key parameters such as interface recombination (h') and minority carrier diffusion length (L_{eff}) [97]. In this work, the Gärtner equation (Equation 3.5) was used as the base of the model, designed in MATLAB. The model can be applied to qualitatively assess the effect of experimental variables.

$$EQE = h' \cdot \exp(-\alpha_{CdS} \cdot d_{CdS}) \cdot \exp(-_{ZnO} \cdot d_{ZnO}) \cdot (1 - \frac{\exp(-\alpha_{CZTSSe} \cdot W)}{_{CZTSSe} \cdot L_{eff} + 1}) \tag{3.5}$$

where α is the absorption coefficient, d is the thickness of the material, W is the depletion width. The prefactor h' represents the interface recombination in the devices, observed in non-optimised interfaces and is given in Equation 3.6.

$$h' = (1 + \frac{S}{\mu_e E_o}) \tag{3.6}$$

where S is the interface recombination velocity, μ_e is electron mobility and E_0 is the maximum electric field at the p-n junction. The model uses the parasitic absorption terms of the window and buffer layers alongside the thickness of the corresponding layer. The current absorption in the absorber material is calculated using α of the semiconductor material, W and L_{eff} [97].

The model generates a calculated EQE curve based on Equation 3.5 which can be directly compared to the experimental EQE curve. The root mean square of the difference between the experimentally measured EQE spectra and the simulated spectra is obtained to find the corresponding L_{eff} and h' values to obtain the closest possible calculated curve.

3.2.5 Capacitance-Voltage (CV)

CV is the technique of applying a voltage to a p-n junction and measuring the output capacitance to obtain solar cell device parameters such as the depletion width (W) and

doping concentration (N_A). The Mott Schottky equation shows the relationship between the applied voltage bias and the measured capacitance, Given in Equation 3.7 [98].

$$C(V)^{-2} = \frac{2(V_{bi} - V)}{q\varepsilon\varepsilon_0 A^2 N_A} \tag{3.7}$$

where q is elementary charge, ε_0 is the vacuum permitivity, ε is the kesterite dielectric constant [60] and A is the device area. The built in voltage of the device V_{bi} was obtained by taking the slope intercept of the x-axis on the C^{-2} versus bias voltage plot. N_A was obtained by rearranging Equation 3.7, yielding Equation 3.8

$$N_A = \frac{-2}{q\varepsilon\varepsilon_0 A^2 (\frac{d(1/C^2)}{dV})}. \tag{3.8}$$

Furthermore, using Equation 3.9 the junction capacitance can be expressed as a function of distance from the junction (x). To obtain W, Equation 3.9 is rearranged and taken at zero bias arriving at Equation 3.10 [72]

$$C = \frac{\varepsilon\varepsilon_0 A}{x}, \tag{3.9}$$

$$W = \frac{\varepsilon\varepsilon_0 A}{C}. \tag{3.10}$$

CV profiles were obtained in dark conditions using a Agilent E4980A Precision LCR meter using a two probe measurement design. Versa Studio software was used to apply both forward and reverse voltage bias across the device.

3.3 Mechanical Bending

To evaluate device performance for CZTSSe thin film flexible cells during bending, a bespoke experimental rig was designed and implemented.

The experimental set up was comprised of two metal plates loaded onto a turning screw driven by a DC motor. The solar cell device was clamped into the rig at horizontally at either side and tightened into place using screws, shown in Figure 3.6. The stages were then driven together, shown on Figure 3.6, using the DC motor at a constant speed of 0.27 mm/s and therefore bending the cell. A code to control the motor was created in Arduino and uploaded to an Arduino Uno which was connected to the DC motor for ease and repeatable control. The experimental set up allowed for JV, EQE and CV measurements to be conducted during the bending process. Figure 3.7 shows a global view of the set

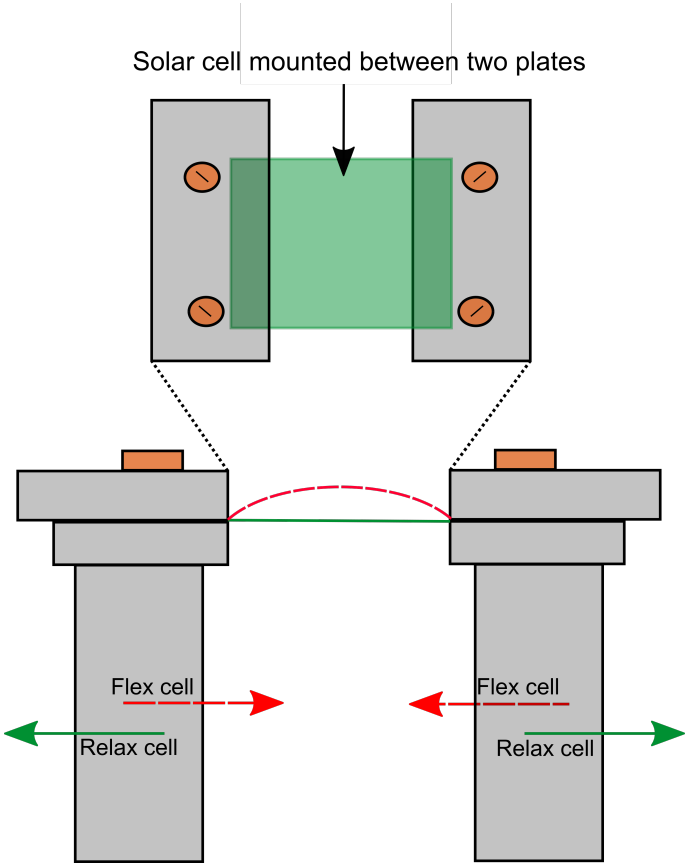

Figure 3.6: Diagram of the experimental rig designed to bend flexible solar cells.

up. To quantify the effect of bending on CZTSSe cells, the DC motor was run for 10 s, a side profile image of the solar cell device was taken, and the JV measurements were performed. Taking a side view image is vital in analysing the ROC of the device. The image was then imported into Inkscape and manually fitting a circle to obtain ROC of the cell, as shown in Figure 3.8. By controlling the time the motor ran for allowed for precise control over the ROC the device was bent to.

The bending induced strain for a multi layer structure is calculated using Equation 3.11. Where for a ROC (R) the strain inducted (ε) and the position z in the cell is a linear function between the distance of z and the neutral axis z_{NA} given in Equation 3.12 [99, 100].

$$\varepsilon(z,R) = \frac{z - z_{NA}}{R} \tag{3.11}$$

$$Z_{NA} = \frac{\sum Z_i(E_i \cdot t_i)}{\sum E_i \cdot t_i} \tag{3.12}$$

where each layer in the structure (i) has a respective thickness t_i, a Young's modulus E_i and a reduced layer thickness of the i^{th} layer of Z_i. To complete 100 cycle tests, the Arduino Uno was coded to run the DC motor forwards for 60 s obtaining a desirable radius of curvature, stop and then reverse the direction for another 60 s. This cycle was

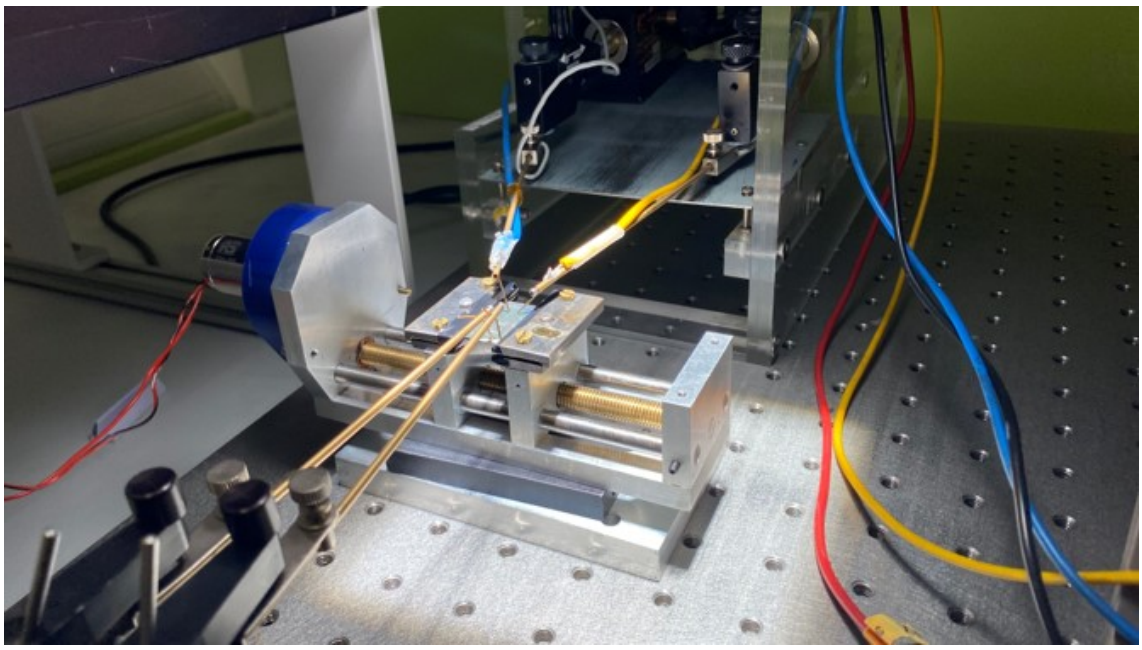

Figure 3.7: Flexible CZTSSe solar cell during JV analysis whilst bending in the designed experimental rig.

set to run 10 times initially to ensure reputability and then the code adapted to run for 100 cycles uninterrupted.

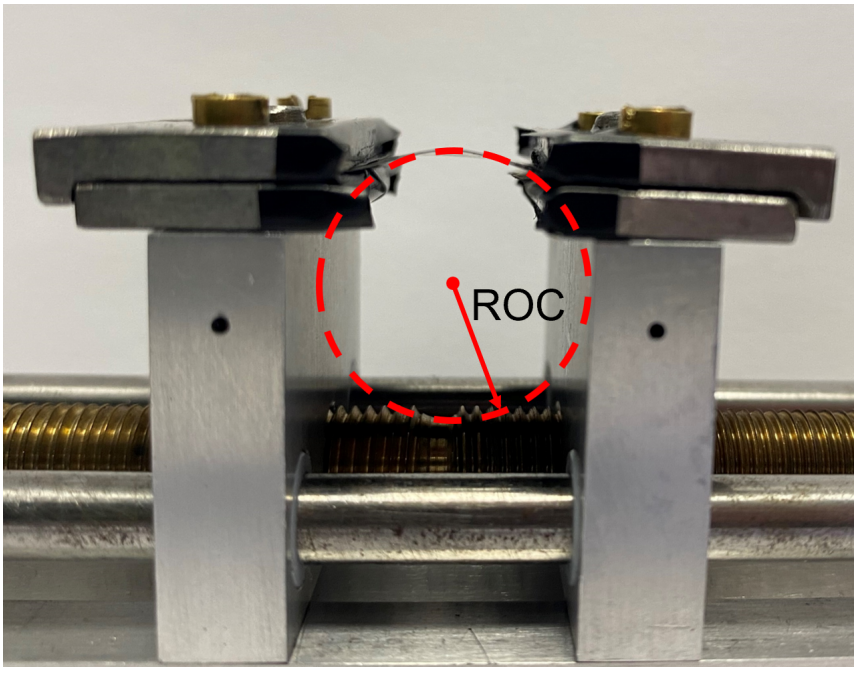

Figure 3.8: Side view image of a CZTSSe solar cell during a bending regime to analyse the ROC.

Chapter 4

Doping of CZTSSe solar cell devices on flexible Mo foil substrates

4.1 Solution Based NaF Doping

Integration into new state of the art devices and small scale distributed energy relies on development of low cost, sustainable and high performing flexible solar cell devices. Despite of recent advancements of flexible CZTSSe technology, achieving 10.3% PCE on Mo foil [4], there still remains a considerable performance deficit in comparison to flexible CIGS which demonstrates 20.4% PCE on flexible polyimide (PI) substrates [101]. In addition to this, the processes used to achieve this performance are vacuum based, which raises sustainability and scaleability issues. There remains, therefore, a pressing need for advancements in CZTSSe solar cell performance. One route to achieve this is alkali doping. It has been reported that alkali doping is crucial in both CZTSSe and CIGS solar cells to achieve high performance regardless of the flexible substrate used. Doping materials used to increase PCE include Na, K, Rb, Cs and Li [102, 103]. All have had relative success, and Li has shown more effective to incorporate into kesterite structure due to its smaller atomic radii and therefore lower formation energy [104]. Despite this, the greatest device improvement still arises from the use of Na doping and therefore making it the most commonly used dopant with research. Na has demonstrated a reduction in non-radiative recombination arising from passivisation of grain boundaries [105, 106]. On SLG, typically used as the rigid substrate for kesterite and CIGS cells, devices are intrinsically doped with Na that diffuses from the SLG substrate during high temperature processing [107]. In order to provide this Na source in flexible substrates, devices must

be actively doped which has been achieved using MoNa back contacts [108, 109], Na layers above or below the CZTSSe light absorbing layer [110, 111] or the inclusion of NaF within the nanoparticle inks used to fabricate the absorber [112]. The latter, provides a sustainable solution based process with low toxicity and crucial for advancing the field. In this work, NaF in varying amounts, is used during the concentration of CZTS nanoparticle inks to optimise a low cost solution based method.

4.1.1 Experimental Method

In this study, CZTSSe solar cells are fabricated with the discussed structure described in Section 3.1 on 0.1 mm Mo foil. CZTS nanoparticle inks were fabricated according to the procedure outlined in Section 3.1.2. The inclusion of Na, in this work, was achieved by dissolving NaF crystals into the concentrated nanoparticle inks. 1.9, 3.8 and 6.3 mg of NaF crystals were added to separate centrifuge tubes of nanoparticle inks. The inks were then sonicated for 60 minutes to ensure the NaF had dissolved. We assume all of the NaF added is dissolved into the ink. Using this method, achieves a NaF concentration of 0.03, 0.06 and 0.1 mol/L respectively. As 0.03 mol/L demonstrated good cell performance and is similar to alkali doping ratios reported in the literature [84,113–115] this value was used as a basis. Additionally here, a reference CZTSSe solar cell on Mo foil was fabricated with no doping and a device with SLG doping was fabricated to compare the two doping methods. SLG doping, here, is the process of including a slide of SLG in the graphite box during the high temperature selenisation step of solar cell fabrication given in more detail in Section 3.1.4. Excluding the doping induced, the cells were fabricated identically.

4.1.2 Morphology and Composition

To investigate the effects of various Na doping values on the composition of the CZTSSe absorber layer, the atomic precursor composition is mapped on the ternary diagram given in Figure 4.1. This data shows that, irrespective of the doping the CZTSSe absorbers have a consistent composition of metallic precursors that is within the ideal range for device performance identified by the hexagon. This has been identified here, to ensure there are no additional losses during the nanoparticle fabrication or selenisation step, in which the metallic elements can be lost or replaced.

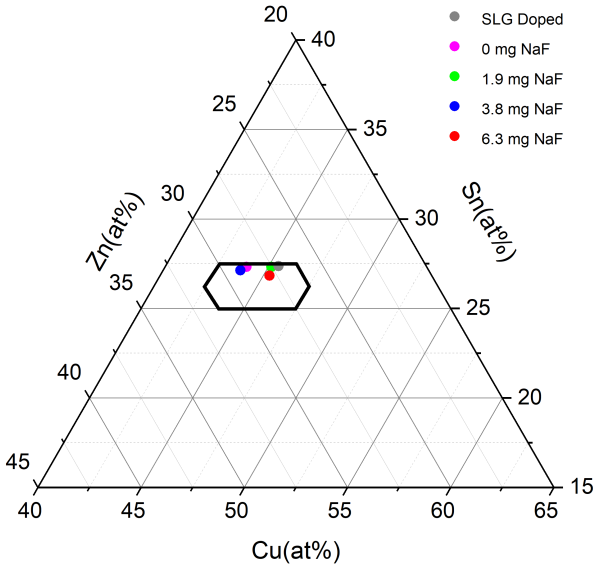

Figure 4.1: Ternary diagram of the atomic percentage of metallic precursors with different amounts of sodium doping for CZTS fabricated on Mo foil. The ideal area for high efficiency devices is outlined as the hexagon area on the diagram.

To investigate the morphology and structure of the absorber layers, top down and cross sectional SEM images were taken and presented in Figure 4.2. From the top down images, given in Figures 4.2a, c, e, g and i, it is shown that the CZTSSe film doped with SLG within the furnace demonstrates the largest average grain size of 0.95 µm. Whereas, the NaF doped samples have a considerably smaller average grain size, for example, the sample doped with 6.3 mg of NaF demonstrates an average of 0.5 µm. The assumed reasoning for this is Na mechanics. Na is free to move within the SLG and therefore free to move from the substrate into the precursor layer. However, with NaF doping, it is known that Na can occupy the V_{Cu} sites [21]. This limits non radiative recombination in the cell but, is assumed, to limit the movement of Na in the absorber required for grain growth. It is seen that doping with NaF has a very little effect on the grain sizes and morphology of the absorber layer. Across the samples, from non-doped to 6.3 mg of NaF included, little to no change is seen in the grain size and homogeneity of the grains.

Similarly, from cross sectional images Figure 4.2, doping shows little effect of the characteristic fine grain layer [116]. It can be seen that with an increasing in dopant amount, the fine grain layer remains consistently ∼500 nm. Interestingly, there is little change observed in the size of the grains from cross sectional images. With the grain thickness

comparable, it can be assumed that any improvement in J_{sc} within the completed devices arises from improved charge extraction rather than light absorption.

4.1.3 Solar Cell Device Performance

Figure 4.3 shows the extracted champion JV curves from the completed solar cell devices under AM 1.5 conditions. The average optoelectronic properties from 9 devices per doping concentration are summarised in Table 4.1. It can be seen that the increase in doping amount in the CZTSSe device relates to a small increase in power conversion efficiency. The device with 6.3 mg of NaF almost matches the SLG doped device, demonstrating PCE values of 2.9% and 3%, respectively, and is an improvement on the non-doped case. However, even with high doping amount of 6.3 mg, the NaF doped device still lags behind the SLG doped device performance, driven by R_{SH}. The increase in PCE arises from both an increase in V_{oc}, J_{sc} and FF. The increase in J_{sc} is assumed to be from an increase in carrier collection as previously discussed and supported by EQE data discussed in Section 4.1.4. Na is known to passivate the grain boundaries within CZTSSe solar cells, eliminating deep level donor defects and therefore improving carrier collection [106]. In addition to this, doping also improves the R_{SH}. We also attribute this to elimination of non-radiative recombination centres. The SLG doped sample demonstrates a R_{SH} value similar to that of rigid devices, however the other doped devices do not. A conclusion can be drawn that there is a mechanism being achieved through SLG that improves device resistance, this could be due to solubility issues using NaF and therefore devices yield less doping than initially designed. This aspect requires further investigation. Finally, the V_{oc} of the devices shows improvement with doping, we assume this to be due to Na occupying the V_{Cu}, which, can result in a Cu depleted surface which in turn improves the CZTSSe/CdS interface and may result in fewer losses in the CdS layer [117]. To further investigate this hypothesis, the EQE spectra of the devices was obtained.

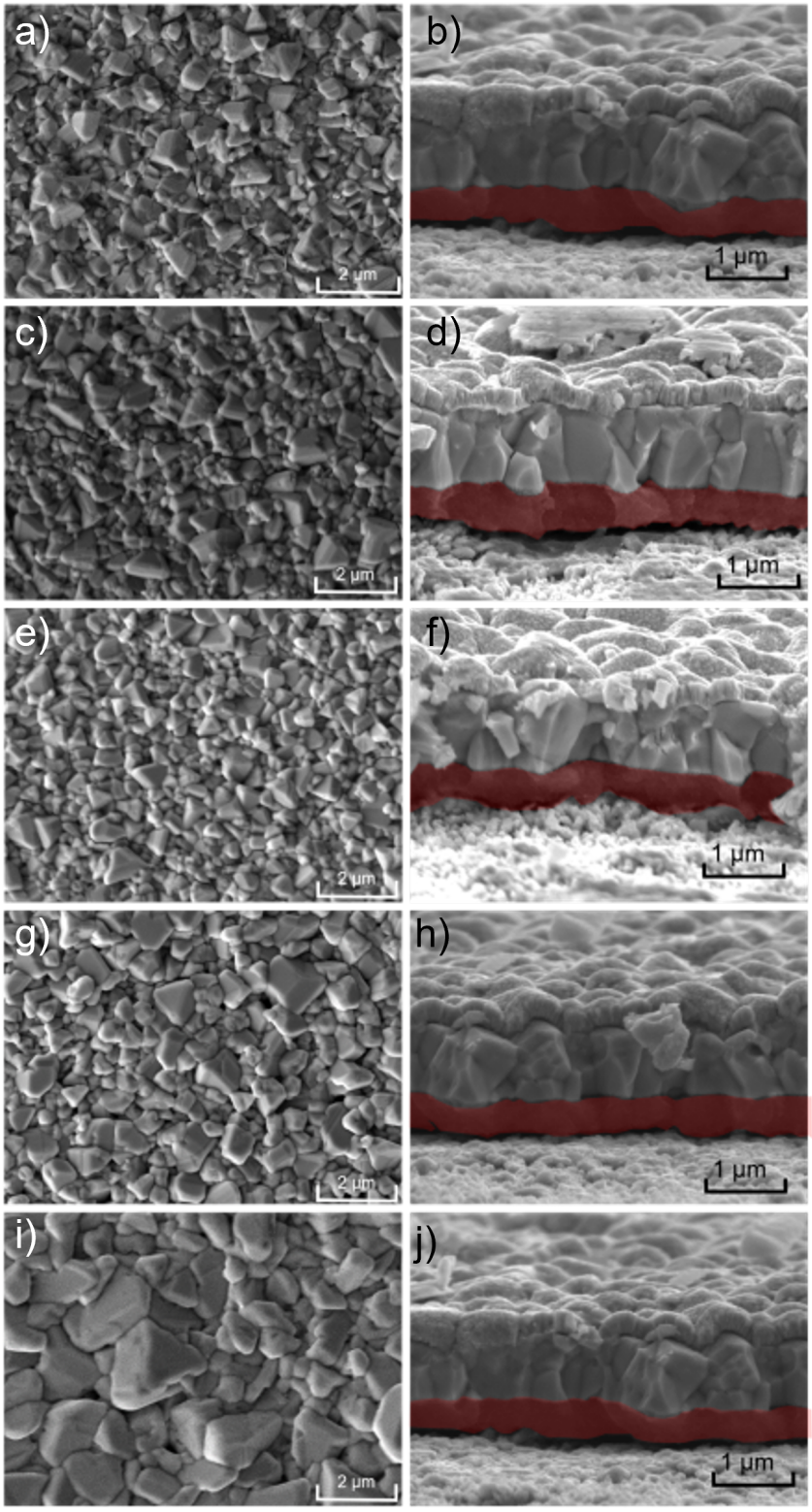

Figure 4.2: SEM images of CZTSSe absorbers with various doping amounts and inclusion methods. Parts a) and b) show the top down morphology and the cross sectional image respectively with no doping. Similarly parts c) and d) have 1.9 mg of NaF doping, e) and f) have 3.8 mg of NaF included, g) and h) have 6.3 mg of NaF and finally i) and j) have SLG present in the furnace as a doping source.

Table 4.1: Average parameters across 9 devices of CZTSSe flexible solar cell devices fabricated with various Na doping amounts obtained from JV data.

	V_{oc} (mV)	J_{sc} (mAcm^{-2})	FF(%)	η (%)	R_s (Ωcm^2)	R_{sh}(Ωcm^2)
0 mg	200 $\pm$9.5	28.3 $\pm$2.2	36.3 $\pm$3.6	2.2 $\pm$0.1	3.8 $\pm$0.6	19.2 $\pm$1.5
1.9 mg	200 $\pm$8.2	30.2 $\pm$1.1	29.5 $\pm$2.6	2.4 $\pm$0.1	3.8 $\pm$0.7	9.4 $\pm$2.3
3.8 mg	210 $\pm$10.6	30.9 $\pm$2.8	36.9 $\pm$3.7	2.7 $\pm$0.2	4.1 $\pm$1.2	20.3 $\pm$4.1
6.3 mg	240 $\pm$9.9	31.4 $\pm$1.5	41.0 $\pm$5.2	2.9 $\pm$0.2	3.9 $\pm$1.1	30.8 $\pm$4.2
SLG Doped	230 $\pm$7.2	31.6 $\pm$1.2	45.7 $\pm$3.1	3.0 $\pm$0.1	2.8$\pm$0.5	62.7 $\pm$2.2

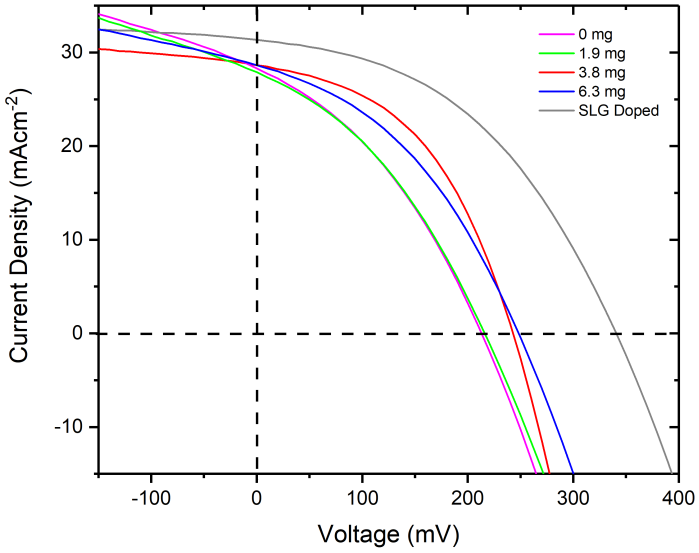

Figure 4.3: JV characteristic curves for champion CZTSSe solar cell devices fabricated with the structure outlined in Section 3.1 with varying Na doping amounts.

4.1.4 EQE Spectra and Extracted Parameters

The measured EQE spectra of the devices is given in Figure 4.4a. As hypothesised in the previous section, Na is thought to improve the CZTSSe/CdS interface and limit losses in the CdS layer from the observed results. Looking at the CdS wavelength range (400-600 nm) this is supported by the EQE data. In the higher doped cells, greater collection is seen in the CdS layer. An improvement is also seen in the higher wavelength range with an increasing amount of Na added to the device, similarly to JV, the device doped with SLG has the greatest EQE in this region. This is attributed again to the reduction

in recombination centres and therefore a longer carrier diffusion length in addition to the promoted grain growth [115, 118]. Additionally, the EQE curves are integrated to obtain the J_{sc} to compare it with the values measured through JV measurements. Table 4.2 shows a comparison of the two varying J_{sc} values. The values obtained from the EQE integration show that, as discussed previously, the J_{sc} values obtained are higher than those obtained from JV measurements arising from the elimination of losses from shadowing and the contact area. The EQE values also provide a justification of the JV measurements as, with increasing doping, the same relationship is observed of a rise in J_{sc}.

Table 4.2: Extracted J_{sc} values from EQE measurements compared to those from JV measurements.

	EQE J_{sc} (mAcm^{-2})	JV J_{sc} (mAcm^{-2})
0 mg	29.1	28.3
1.9 mg	31.0	30.2
3.8 mg	32.6	30.9
6.3 mg	33.1	31.4
SLG Doping	33.5	31.6

To quantify the improvement seen within the experimental EQE curves, the EQE model described in Section 3.2.4 was applied to the spectra and the extracted parameters are given in Table 4.3 alongside the fitted curves in Figure 4.4b.

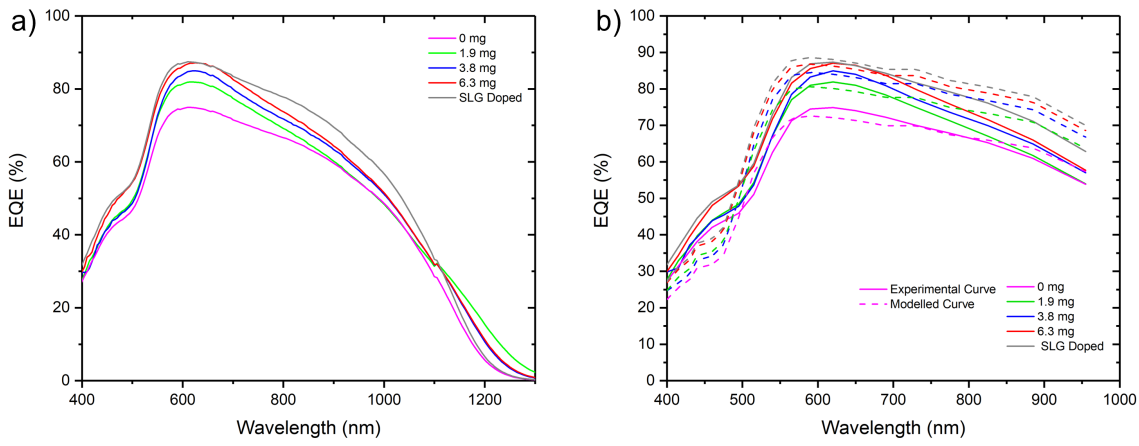

Figure 4.4: a) EQE spectra for CZTSSe solar cell devices with varying amounts of Na doping alongside b) modelled EQE curves to the experimental spectra.

The relative improvement in carrier diffusion length can be seen, with the increase in dopant increasing the L_{eff}. Additionally, the surface recombination decreases with the doping and this is assumed to be due to an improvement in the device mobility due to grain boundary passivisation from Na. From the EQE spectra, no change in the band gap is observed. To complete the EQE modelling, the depletion width W_d was input for each doping amount. This was obtained from CV measurements described in the following Section 4.1.5.

Table 4.3: Extracted properties from applying EQE modelling to the obtained experimental EQE spectra of Na doped CZTSSe cells.

	h′ (%)	L_{eff} (cm)
0 mg	95.6	9.5×10^{-6}
1.9 mg	94.1	1.6×10^{-5}
3.8 mg	94.0	1.6×10^{-5}
6.3 mg	91.1	5.1×10^{-5}
SLG Doping	91.0	4.9×10^{-5}

4.1.5 CV Characteristics

Finally, to assess the doping concentration achieved through the various doping amounts, the device capacitance was measured as a function of an applied bias voltage. The data was plotted using the Mott-Schottky equation, outlined in Section 3.2.5 and given in Figure 4.5. Additionally, the doping concentration (N_A) and the depletion width (W_d) are extracted and given in Table 4.4.

Table 4.4: Extracted properties from Na doped CZTSSe cell Mott-Schottky plots.

	W_d (nm)	N_A (cm^{-3})
0 mg	78	9.37×10^{15}
1.9 mg	61	1.12×10^{16}
3.8 mg	89	2.30×10^{16}
6.3 mg	139	5.56×10^{16}
SLG Doping	238	9.50×10^{16}

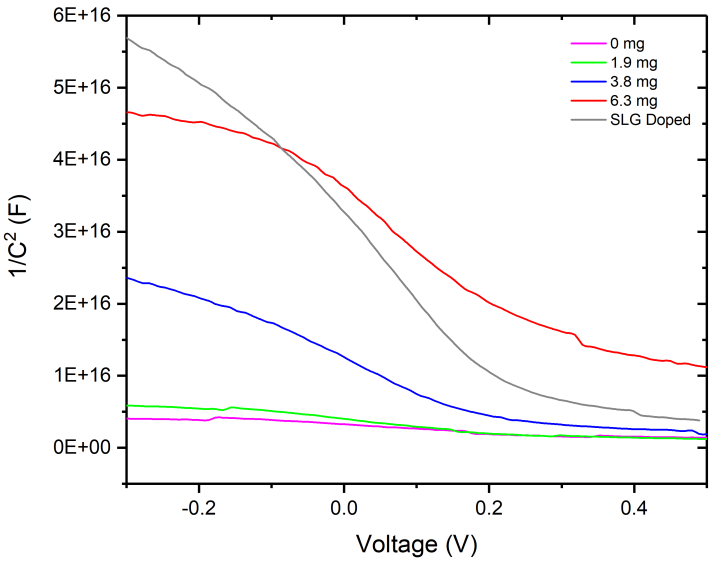

Figure 4.5: CV measurements for CZTSSe solar cell devices doped with various amounts of Na.

It is evident from Table 4.4 with an increase in added NaF into the nanoparticle inks, the doping concentration of the final device also increases. This supports this method as a solution based alternative method for doping flexible CZTSSe solar cells on Mo foil. In addition, the increase in Na causes a widening of the depletion width. The improvement of device performance with increasing doping is therefore, attributed to increasing carrier concentration and mobility.

4.2 Doping Using Antimony Selenide

Whilst Na is well-established as a doping material to improve the performance of CZTSSe solar cells, a new approach to promote grain growth is based on Sb_2Se_3. At high temperatures, such as those used during fabrication of CZTSSe devices, a thin film of Sb_2Se_3 can form a semi-liquid phase [119]. This semi-liquid Sb_2Se_3 can diffuse into the CZTS absorber layer and result in a promoted grain growth of the CZTSSe grains. There is limited literature on this work, one vacuum based processes has been demonstrates elsewhere outlining the potential of Sb_2Se_3 as a dopant material for CZTSSe in which layers of varying thickness' are deposited on the substrate prior to the deposition of CZTSSe and analysed with regards to the CZTSSe morphology and performance with the addition of added Sb_2Se_3 [119]. In this work, the foundation results are obtained for a solution based

alternative by using layers of various thickness' underneath the CZTSSe layer.

4.2.1 Experimental Method

To investigate firstly the optimum amount of Sb_2Se_3 for encouraged grain growth; 50, 100 and 200 nm layers of Sb_2Se_3 were deposited onto Mo coated Mo foil substrates. This was achieved using thermal evaporation, but in future work, could be replaced with a Sb_2Se_3 solution based method. A reference CZTSSe solar cell device with no doping was also fabricated, for comparison. The CZTSSe solar cells were then completed to normal procedure outlined in Section 3.1.

4.2.2 Composition

Using elemental analysis, the quantity of Sb present in the CZTSSe absorber layer after selenisation was obtained. In addition, the S/(S+Se) was determined to asses the effect of inclusion of the extra Se source from the Sb_2Se_3 layer.

Table 4.5: CZTSSe absorber composition with a Sb_2Se_3 doping layer beneath the precursor.

Layer Thickness (nm)	Se/(Se+S)	Average % Sb (at%)
0	0.931	0
50	0.930	0.79
100	0.931	1.43
200	0.928	2.12

From the EDS data, given in Table 4.5, an increase in the amount of antimony diffused into the absorber is observed with a thicker Sb_2Se_3 precursor layer. This is yet to be optimised but shows good promise for easy tailoring of the amount of doping included in the CZTSSe cells. Observing the Se/(S+Se) relationship, the amount of Se within the device remains around the same, even with an increase in Se provided by a thicker Sb_2Se_3 layer. The reasoning for this is yet to be understood as with a constant S amount and an increase in Se, an increase would be expected. To fully understand this, further investigation is required.

4.2.3 Morphology

Top down SEM images quantify the effect of the various Sb_2Se_3 layers on the completed CZTSSe absorber morphology, Figure 4.6.

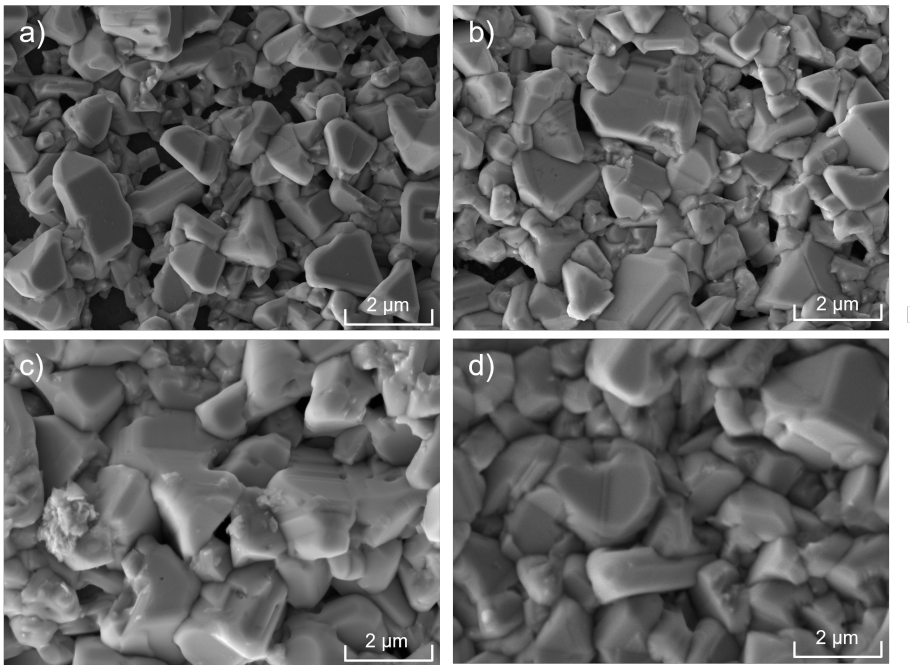

Figure 4.6: Top down SEM images of CZTSSe photovoltaic absorbers with Sb_2Se_3 layers of thickness a) 0, b) 50, c) 100 and d) 200 nm deposited before the absorber layer.

The CZTSSe absorbers were observed to be more compact and demonstrate larger grain sizes in with an increasing thickness of Sb_2Se_3. Figure 4.6a, the reference sample, demonstrates a non homogeneous pin hole surface with smaller grain sizes. Increasing the doping amount yields homogeneous, smooth large grain structure as seen in Figure 4.6d. This shows large potential for Sb_2Se_3 as a doping layer within CZTSSe cells and further work is required to quantify these improvements on device performance.

4.3 Summary

This chapter presents an optimisation of the amount of Na required for scaleable, solution based Na doping in flexible CZTSSe solar cells. The work finds that, an increasing amount of NaF dissolved into nanoparticle ink yields improving device performance. However, in this work we show that although this method is successful in improving the device parameters, a more achievable way to increase device performance is through SLG doping during the selenisation process. The SLG doped flexible CZTSSe provides a rela-

tive high efficiency low cost and scalable route to Na doping. In order to further improve this work, a different source of solution based Na is to be considered alongside larger doping quantities. In addition to Na, this chapter also shows the potential for Sb_2Se_3 doping in CZTSSe flexible solar cells. Doping with a 200 nm layer of Sb_2Se_3 beneath the cell absorber layer demonstrates large grain growth with a pin hole free surface. To fully quantify this work, solar cell devices are required.

Chapter 5

Mechanical Bending of CZTSSe Devices Deposited using Slot Die Coating

5.1 Mechanical Bending of Solar Cells

Various applications require flexible PV devices that are mechanically stable and perform competitively under mechanical loading and bending, for example in the automotive industry. PV devices are typically designed in a planar state, and demonstrate performance change when bent [120]. It is, therefore, key to investigate flexible solar cell behaviour during bending whilst still considering the sustainability and cost effectiveness of the device. Despite the advantages and breadth of applications outlined with CZTSSe solar cells in Section 2.6, there has been little work reported on the performance of CZTSSe solar cell devices during mechanical bending. The literature current has testing CZTSSe solar cells using manual bending techniques and show only a degradation in device performance [121, 122]. In contrast, comparable thin film CIGS in which bending tests are widely reported [100, 123]. CIGS devices show a degradation in cell performance under curvature resulting in irreversible damage to the device when returned to a planar state as a result of deterioration and cracking of the semiconductor materials resultant in a decrease in V_{oc} [123]. In this work, we demonstrate CZTSSe cells fabricated on Mo foil can be curved up to a ROC of 64 mm without degradation of the PV performance. Notably, this exceeds the typical ROC for an automotive roof. The evolution of the device performance is reported alongside cyclic testing to evaluate cell longevity.

5.2 Experimental Method

CZTSSe solar cell devices were fabricated in a substrate configuration as given in Section 3.1. A 1 μm layer of Mo was coated onto the 0.05 mm foil substrate using direct magnetron sputtering to reduce R_S and provide a high-quality interface with the CZTSSe PV absorber layer [124]. CZTS nanoparticle inks were deposited on the substrate using slot die coating. For this step, the 25×75 mm Mo foil substrate was mounted on to a glass slide to ensure a flat surface for deposition. A uniform and densely packed CZTS nanoparticle precursor was achieved by depositing 4 sequential layers with a substrate speed of 40 mm/s and a ink feed speed of 18.2 μL/s. Each layer provides a thickness of $\sim$ 200 nm and during the deposition. Using slot dye is advantageous in comparison to the traditional method of spin coating, as it substantially reduces the amount of material wastage. It also provides a inexpensive and rapid route to thin film fabrication over a relatively large area which is for scaling-up PV technologies. In order to promote the formation of a high-quality polycrystalline CZTSSe PV absorber, as outlined in Section 4.1.1, a slide of SLG was introduced to the furnace as source of Na during the selenisation. The 25×75 mm substrate was then mechanically scribed to give 33 individual devices each with a total cell area of 0.16 cm^2.

Completed solar cells were tested mechanically using a bespoke experimental set-up which involved clamping a cell between two aluminium arms which were simultaneously actuated using a DC motor. The motor was controlled using an Arduino Uno which could be programme to repeatedly bend the solar cells, outlined in Section 3.3.

5.3 Composition and Morphology

To establish the absorber composition, EDS was performed and analysed with respect to the metallic precursors, Cu, Zn and Sn. The composition of the fabricated CZTSSe films is shown in Figure 5.1, with the addition of an hexagonal region which denotes the most common composition region for high efficiency devices lie [86]. CZTSSe absorber films deposited in this work using slot die coating lie within this region on the ternary diagram with a metallic ratio of Cu/(Zn+Sn)= 0.77. For high efficiency devices, this ratio should ideally be between 0.75 and 0.85 [86]. The selenium to sulphur ratio is also calculated as Se/(S+Se)= 0.93, indicating that 93% of the sulphur has undergone anion exchange with

Se during the selenisation. This limits the amount of recombination centres within the material, by preventing pin holes on the absorber surface.

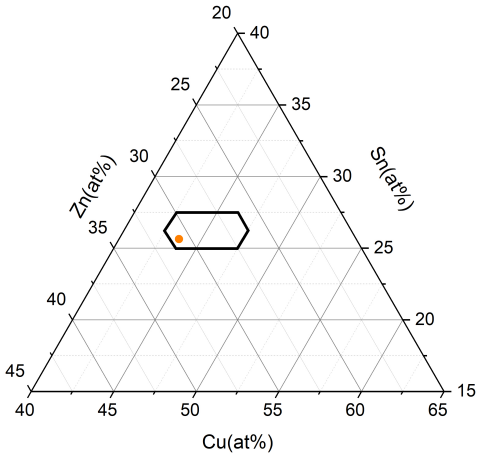

Figure 5.1: Ternary phase diagram of the CZTSSe absorber fabricated for mechanical bending tests. The dark hexagon region within the diagram outlines the desired range for high efficiency devices.

To further analyse the absorber, thin film morphology images were obtained as shown in Figure 5.2. Top view images of the CZTSSe grain layer show the film is composed of densely packed micron sized grains, reducing current pathways that can form at the grain boundaries. The average grain size of the slot die coated absorber films is calculated at 1.00 $\pm$ 0.15 μm, compared to that of spin coated of 0.95 $\pm$ 0.2 μm and spin coating on SLG (Figures 5.2e and 5.2f) of 0.98 $\pm$ 0.3 μm. The average elemental composition and grain size values were broadly consistent across the whole film demonstrating the uniformity of the slot-die fabrication technique.

5.4 Cutting of Solar Cells

5.4.1 Optoelectronic Properties before Cutting

The average of photovoltaic performance of 27 slot-die coated CZTSSe devices on a Mo foil substrate is given in Table 5.1 with the champion device shown in Figure 5.3. Under air mass 1.5 conditions, the PCE is 4.5% which is comparable with the highest reported efficiency for a CZTSSe solar cell on Mo foil made using the nanoparticle ink method [84]. The highest reported efficiency for CZTSSe solar cells on a Mo foil substrate is $\sim$ 10%

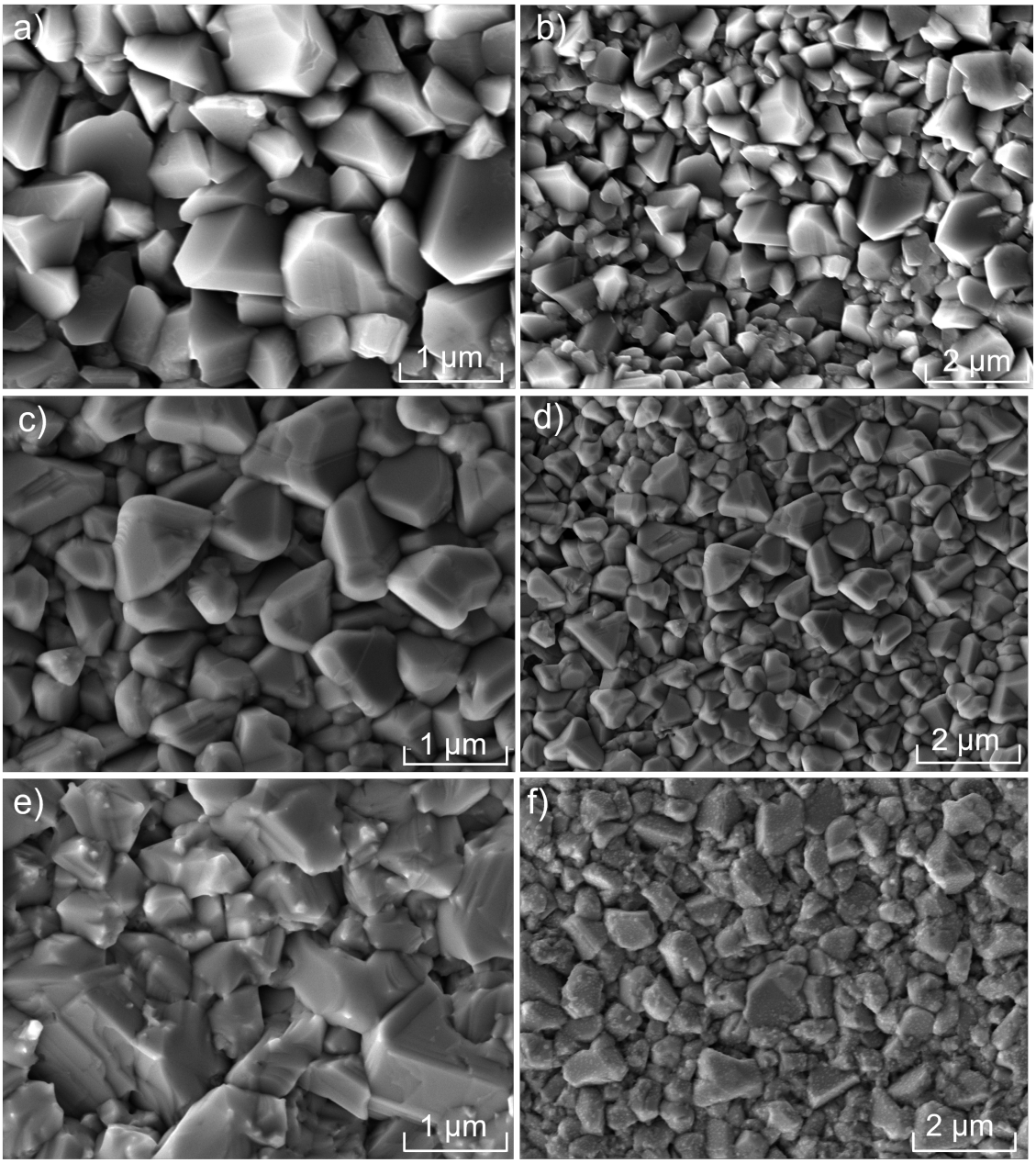

Figure 5.2: Top down surface morphology of CZTSSe thin film absorber layers a) and b) deposited using slot dye coating on Mo foil c) and d) deposited on Mo foil using spin coating and e) and f) deposited on SLG using spin coating.

and was fabricated using sputtering [4]. Compared to sputtering, the nanoparticle ink approach to fabricating the CZTSSe PV absorber is less energy-intensive and requires less capital equipment to make the absorber. Furthermore, using slot-die deposition of the CZTS nanoparticle ink offers the potential for industrial scale-up and reduces waste.

Table 5.1: Average device performance for 27 CZTSSe solar cell devices deposited using slot-die coating.

V_{oc} (mV)	J_{sc} ($mAcm^{-2}$)	FF(%)	η (%)	R_s (Ωcm^2)	R_{sh}(Ωcm^2)
295 $\pm$15	29.3 $\pm$2.2	45 $\pm$4.6	3.9 $\pm$0.6	2.5 $\pm$1.3	68.8 $\pm$6.4

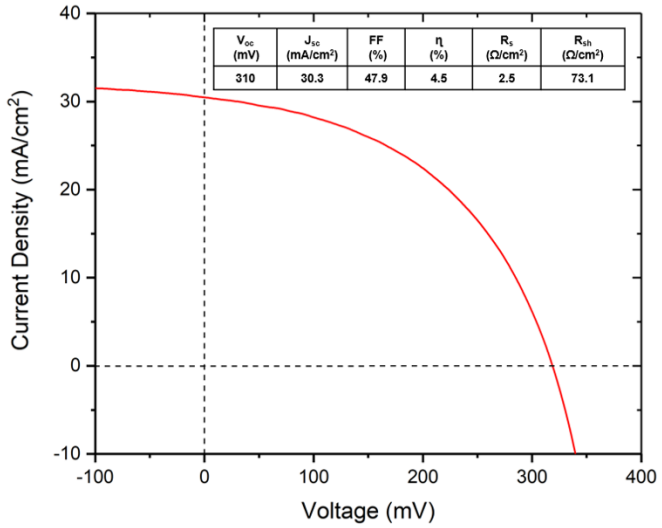

Figure 5.3: JV curve of the champion CZTSSe device deposited using slot die coating on Mo foil.

5.4.2 Cutting of Solar Cell Devices

A feature of the devices fabricated using slot die coating is that they can be cut to any desired size upon completion of the devices without causing performance degradation. This is advantageous for application specific requirements and potentially offers product designers more flexibility in the creation of autonomous devices. To illustrate this functionality, the 25$\times$75 mm substrate was cut, using sharp scissors, into three sections once the device layers were completed. The efficiencies of all the devices on this substrate

were measured before and after this action and Figure 5.4 shows the change in efficiency as a result of cutting. The devices demonstrate little or no degradation once cut resulting in relatively stable device performance across the whole substrate. Note that when the devices are measured on a single 25×75 mm substrate before cutting, there is a single back contact located on the far left of the substrate. Once cut, each substrate requires a back contact and this current pathway is shorter, yielding small differences in contact resistance across the three substrates. This explains the small increase in efficiency observed for some devices after cutting.

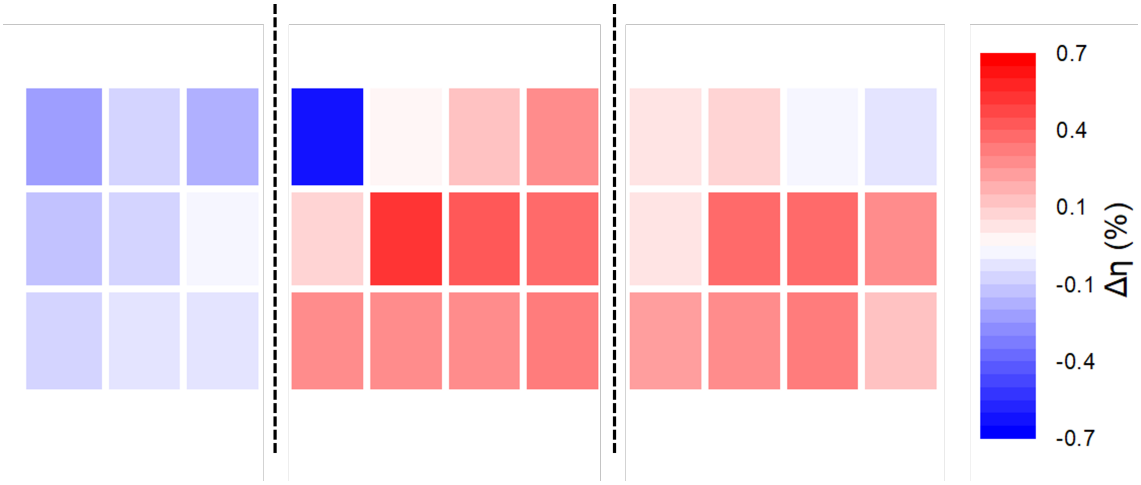

Figure 5.4: Absolute percentage change in measured solar cell PCE values before and after a cutting procedure to produce three smaller solar cell substrates from one large substrate.

5.5 Mechanical Bending

The location of the neutral axis (Z_{NA}) is critical when bending a multi-layer structure and is the point at which the structure does not change with bending. All layers below Z_{NA} are subject to compression where as the layers above Z_{NA} are subject to tension. The location of Z_{NA} in our CZTSSe solar cells was calculated according to Equation 5.1.

$$Z_{NA} = \frac{\sum Z_i(E_i \cdot t_i)}{\sum E_i \cdot t_i} \tag{5.1}$$

where each layer i has a thickness of t_i and a Young's modulus E_i with Z_i taken to be the middle of the layer within the device. The values for these parameters are given in Table 5.2. Using equation 5.1, Z_{NA} is calculated to be 24 µm from the bottom of the substrate as shown as the dashed red line in Figure 5.5a. Z_{NA} therefore lies approximately halfway into the Mo foil substrate and all device layers are thus subject to tensile stress

during bending. The evolution of the device performance during bending is observed by increasing the ROC, which was qualitatively determined by fitting a circle to images of the experimental setup as shown in Figure 5.5b, and measuring the optoelectronic properties at each curvature value.

Table 5.2: Parameters used to calculate the location of the neutral axis in a CZTSSe solar cell structure.

	t_i (nm)	E_i (GPa)	Z_i (nm)
Mo Foil	50000	330	2500
Mo Layer	1000	315	500
CZTSSe	1000	80	1500
CdS	70	46	2035
ZnO	50	117	2095
ITO	200	141	2220

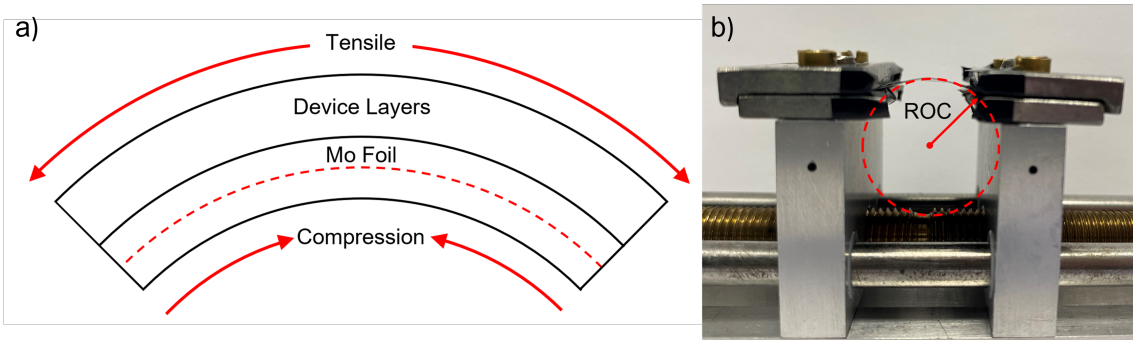

Figure 5.5: a) Schematic of CZTSSe solar cell during bending with the neutral axis location highlighted and b) with an image of a CZTSSe during mechanical bending experiment with a fitted circle to determine the ROC.

Figure 5.7 shows the evolution of the device parameters of one solar cell. The cell had not been used previously for bending tests and was bend incrementally, with measurements taken at several points of the bending regime. In order to do this, the central cell on the device is used, this eliminates changes in device performance due to angle of incidence and additionally is the most experimentally suitable due to placement of the cell contacts. The device PCE changed from 3.0% to 4.16% when the device was bent from the flat state to a ROC of 64 mm before decreasing at higher ROC. This change is accompanied

by a large change in J_{sc} (Figure 5.7c) which is proposed to be due to suppression of current shunting pathways on the micro-scale when the cell is bent. Internal stress cause by mismatch of layers in the cell, induced in fabrication, are suggested to be eliminated during bending [120]. The relatively large change in J_{sc} drives an improvement in the device FF as shown in 5.7b. In addition to this change an increase in the device R_{SH} is observed which requires further investigation to be conclusive but can also be theorised to be due to the current shunting pathways. The changes observed in this cell have also been observed in multiple CZTSSe devices in this work. The rise in J_{sc} and therefore η is consistently measured. Beyond an ROC of 64 mm, the device PCE begins to degrade and this is thought to be a consequence of cracking in the ITO layer at the top of the device. To investigate this hypothesis further, a series of optical microscope images were obtained in the initial flat, curved to an ROC of 56 mm and flat state following bending and these are shown in Figure 5.6. While Figure 5.6a shows a relatively smooth surface in the initial flat state, cracks appears perpendicular to the bending direction in 5.6b at an ROC=56 mm. The cracks appear on the very top surface of the solar cell and additionally the ITO layer is the thickest and most brittle in the solar cell, concluding that the cracks form first within the ITO layer. This limits the current collection and accounts for the drop in efficiency at ROC $>$ 64 mm in Figure 5.7a. Upon returning the device to the flat state the cracks in the ITO are no longer evident in 5.6c indicating that they have closed on the resolution of the optical microscope.

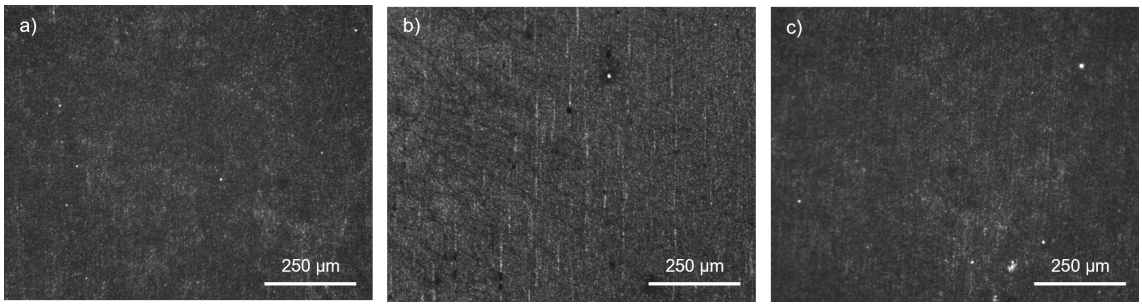

Figure 5.6: Optical microscope images of a CZTSSe device in a) planar state b) at a bending radius of 56 mm and c) returned to planar state.

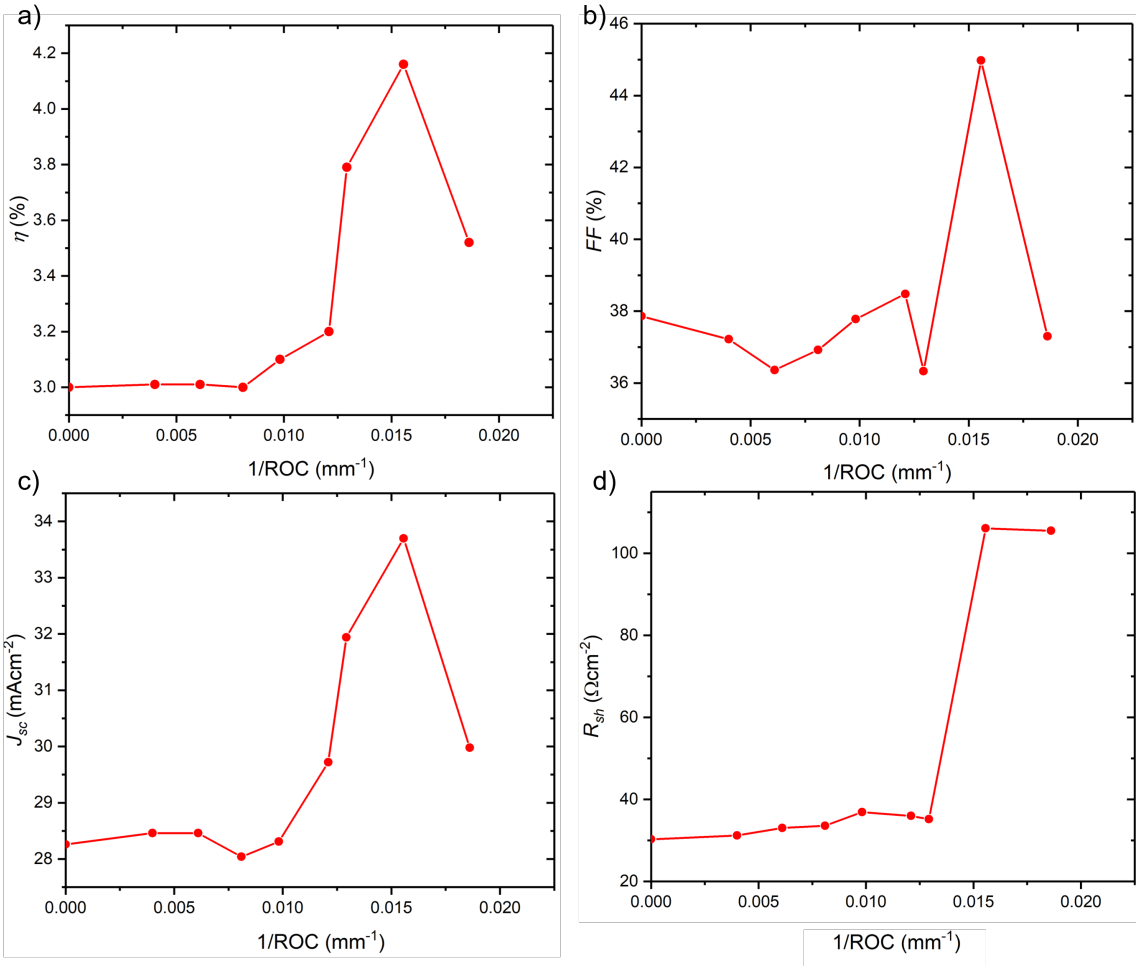

Figure 5.7: The evolution of key solar cell characteristics during bending.

5.6 Cycle Testing

Having studied the evolution of the device performance as a function of bending, we also studied the device performance during cyclic loading i.e. starting from a initial flat state, the device was curved and then returned to flat. This was done for 100 cycles and to a ROC of 64 mm. This was done to determine the device stability and identify if the observed performance changes are reversible. The results of these measurements are shown in Figure 5.8 with the extracted photovoltaic parameters given in Table 5.3.

The cycle test was completed on a newly fabricated device, and the 100 cycles were ran immediately in order to eliminate any degradation from other factors, such as ageing. During the first cycle the cell performance was consistent with Figure 5.7d with an initial small increase in PCE driven by an increase in J_{sc} and R_{SH}. This increase was preserved upon returning the cell to the flat state and again measuring the cell. No further change

Table 5.3: Optoelectronic properties of a CZTSSe solar cell device subject to a 100 cycle bending regime.

	V_{oc} (mV)	J_{sc} (mAcm^{-2})	FF (%)	η (%)	R_s (Ωcm^2)	R_{SH} (Ωcm^2)
Planar	310	32.01	39.39	3.91	4.85	40.75
64 mm ROC	310	33.23	41.84	4.31	4.87	49.01
100 Cycle (Flat)	310	33.21	42.25	4.35	3.93	46.60

was observed in the following 99 cycles. We conclude, therefore, that the initial bending cycle causes irreversible changes in the shunting pathways to improve the device performance, and CZTSSe solar cells fabricated using the nanoparticle ink method are robust during cyclic testing. This is in contrast to the cracking in the ITO layer which appears to be a reversible change that does not present a significant problem to the device performance up to 100 cycles for bending to an ROC that is below the failure point observed in Figure 5.7.

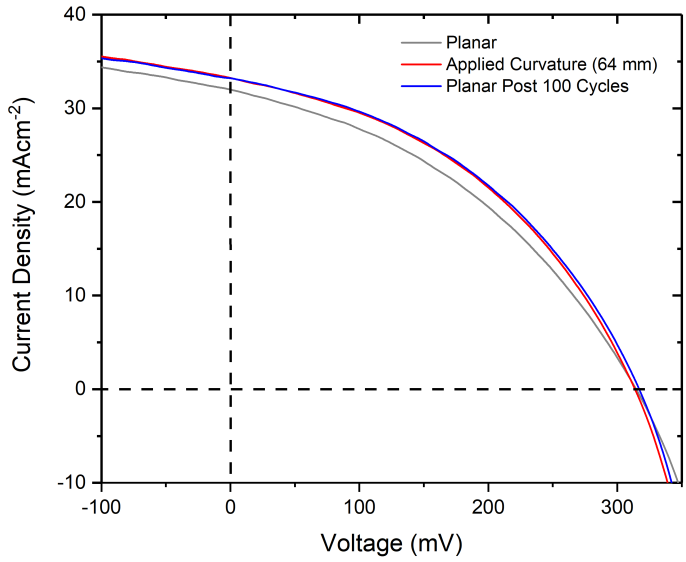

Figure 5.8: JV curves for a flexible CZTSSe cell in planar state, with an applied ROC of 64 mm and post 100 cycle testing returned to planar state.

5.7 Summary

In this chapter, flexible CZTSSe thin film solar cells were fabricated using slot die deposition of CZTS nanoparticle inks on Mo foil substrates. The fabrication process allows the creation of solar cells which can be cut-to-size for application specific requirements. During bending, the cell performance improves slightly as a consequence of an increase in J_{sc} assumed to be driven by a reduction in the current shunting pathways on the micro-scale increasing current collection. This characteristic is preserved over cyclic bending tests up to a ROC which is useful for applications such as vehicle integrated photovoltaics. Beyond a critical ROC, the cell performance degrades as a consequence of cracking due to tension in the ITO layer at the top of the cell structure. To fully characterise these effects, more investigation is required into the changes in each layer of the solar cell when under an bending regime however the work shows promise for the suitability of CZTSSe as a semiconductor material for lightweight flexible solar cell applications.

Chapter 6

Heat Treatment of Kesterite Solar Cells

6.1 Heat Treatment of CZTSSe Solar Cell Devices

Kesterite solar cells demonstrate significant device degradation over time [125]. There is limited reported research as to why this degradation happens, although it has been modelled that the separation of Cu and Zn may contribute to this [126]. Additionally, it was established by Samieipour *et al.* that copper diffusion from the surface of the CZTSSe absorber into the CdS layer acts as a recombination centre in the device therefore lowering performance [127]. Another arising issue, For deployment into the PV market and long term stability, the scale of this degradation and routes in which to recover device performance are crucial. To explore this, the scale of the degradation and ways in which to recover device performance, of CZTSSe solar cells fabricated from nanoparticle inks, is investigated. The mechanism for device recovery is achieved through a post deposition heat treatment (HT) of 150 °C is completed on CZTSSe solar cells. The recovery and properties contributing to this are addressed. Additionally, the degradation and recovery of CZTSSe cells is also investigated with consideration of Na doping, which is a crucial element in achieving high efficiency kesterite cells on flexible substrates.

6.2 Experimental Methods

Fabricated CZTSSe solar cells were allowed to age, at 21 °C in a nitrogen atmosphere under dark conditions for 6-12 months. The CZTSSe solar cells were then subject to a 150 °C HT in an Ar atmosphere. The devices were first measured using techniques such as JV, EQE and CV given in detail in Section 3.2. For annealing, the CZTSSe devices were

loaded into a Carbolite Gero tube furnace on a designed aluminium foil holder to ensure they lie in the centre of the furnace. The tube furnace has a three zone heating design, in which the centre zone was used for the HT process. Once loaded, the furnace was flushed with Ar for 5 minutes to eliminated any O_2 in the tube from sample loading. The temperature was then increased to the desired value and then held at constant temperature for 10 minutes under constant Ar flow of 0.5 L/min. Once the HT was complete, the samples were removed from the heating zone into a cool zone of the furnace and rapidly cooled under the same Ar flow. Once the temperature had reached below 100 °C the Ar flow was cut off and the samples were left in the furnace overnight to cool to room temperature. The samples were then removed and analysed.

6.3 Degradation Analysis

Kesterite solar cells demonstrate degradation over time [126, 127]. This has been attributed to many possible causes such as oxidisation, photo-oxidation and the breaking down of the kesterite structure due to diffusion of elements. The mechanisms in which this degradation happens is still a highly researched topic, as the driving force is still not defined. Here, a CZTSSe solar cell device left for 6 weeks in the dark, at room temperature and in a nitrogen atmosphere with standard humidity. The degradation is monitored using JV measurements to observe changes in the optoelectronic properties.

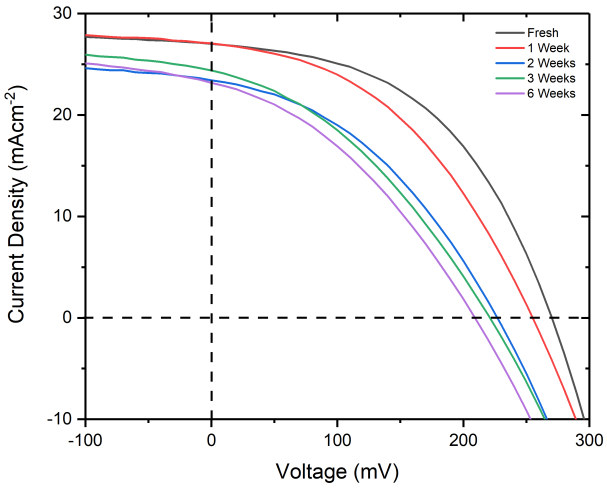

Figure 6.1: JV Curves for a CZTSSe solar cell left in ambient laboratory conditions for 6 weeks.

Figure 6.1 shows the optoelectronic properties of a singular CZTSSe solar cell device when fabricated (within 1 hour of the final scribing process outlined in Section 3.1.9) and than again weekly up to 6 weeks after fabrication. Within one week the device begins to degrade, specifically the V_{oc}, J_{sc} and FF. This could be attributed in the early stages to a non ohmic barrier at the back side of the device but this proves difficult to conclude as cells are not encapsulated [126]. Notably, after 2 weeks the device begins to degrade in all properties and then continue to degrade for up to 6 weeks at a slower level than initially. To observe this closer, the optoelectronic properties over time are plotted in Figure 6.2. An increase in R_S and decrease in R_{SH} is observed. Another potential cause of the device degradation is the oxidisation of the front Ni and Al contacts which causes a lowered J_{sc} due to poor current collection and increased resistance, further work is required to quantify this effect. In comparison to the lifetime of solar cell devices commercially (5-10 years), the degradation in CZTSSe devices is initially very quick but begins to show a plateau relatively quickly. This however, makes CZTSSe less desirable for high level solar cell deployment in industry. The mechanisms which cause this degradation are not investigated here, but observed for rectification purposes using HT.

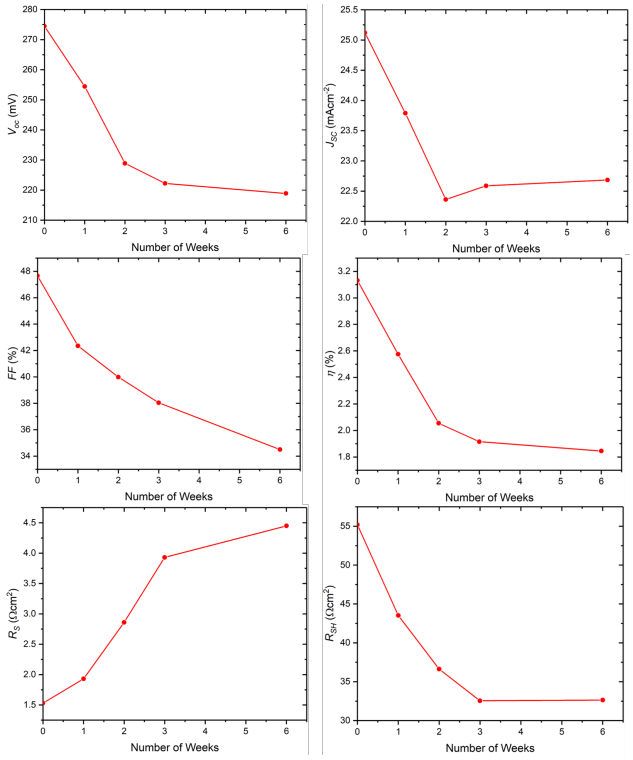

Figure 6.2: Evolution of optoelectronic properties of an average across 9 CZTSSe solar cells stored in ambient laboratory conditions for 6 weeks.

6.4 Temperature Investigation

It has been well cited that a post absorber deposition HT improves device performance [128–133] with specific interest in the mitigation of a V_{oc} deficit through elimination of defects. However, here the effect of HT on the completed device structure in Ar on time-degraded CZTSSe cells for device stability and recovery purposes is investigated. To determine the optimal temperature for device rectification, four CZTSSe solar cells were subject to a systematic HT process at varying temperatures (100-250 °C) for 10 minutes, with 9 devices on each cell. All cells were fabricated on SLG in this study. The JV characteristics of the devices were measured in the aged state and then again after HT shown in Figure 6.3. The aged solar cell devices show a significant loss in *FF* leading to a loss in all optoelectronic properties. Shown in Figure 6.3 and Table 6.1 the *FF* is recovered during HT, but notably the best performance change is observed at 150 °C. The HT recovery process for following devices was therefore carried out at 150 °C for 10 minutes. Table 6.1 shows the absolute change in the average device properties across 9 devices. This is given as, the cells can only be subject to one HT to accurately quantify the change due to the HT alone. Therefore, for the temperature analysis study 4 CZTSSe solar cells were used each of which were fabricated and ages identically, but demonstrate varying initial and aged performance.

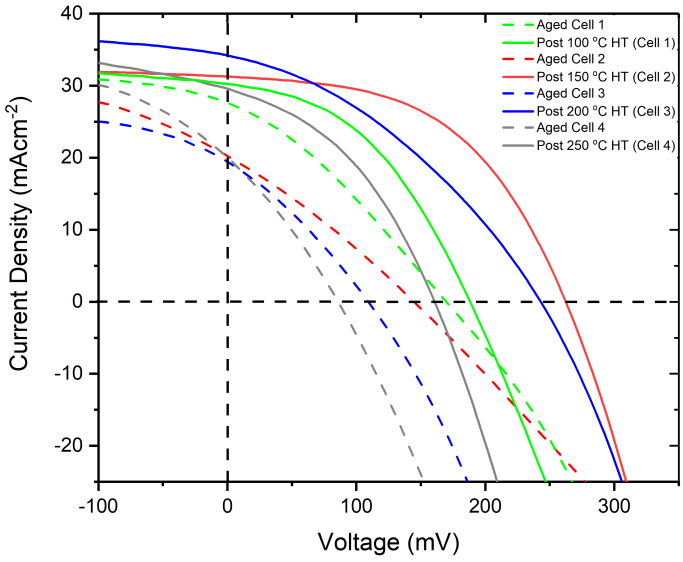

Figure 6.3: JV curves for devices subject to varying HT temperatures when aged and after the HT process.

Table 6.1: Absolute difference in average solar cell device properties across 9 devices subject to varying HT. The change is given from the ages state of the devices to the device performance once heated. All HT processes were held for 10 minutes.

Temp(°C)	ΔV_{oc}(mV)	ΔJ_{sc}(mAcm^{-2})	ΔFF(%)	$\Delta\eta$(%)	ΔR_S(Ωcm^2)	ΔR_{SH}(Ωcm^2)
100	20	0.94	12.4	1.6	0.76	24.03
150	30	4.3	18.55	2.39	5.7	41.7
200	16	2.92	14.81	1.13	4.33	25.41
250	50	3.76	10.84	2.33	4.78	16.55

6.5 Recovery Mechanisms

To investigate the HT recovery mechanism, CV and EQE measurements are given of the device in aged state and after the HT at 150 °C in Figure 6.4 and 6.5. Additionally, the optoelectronic properties can be seen in Table 6.2.

Table 6.2: Average optoelectronic properties of 9 CZTSSe solar cell devices in aged state (6 months) and after a HT of 150 °C for 10 minutes.

	V_{oc} (mV)	J_{sc} (mAcm^{-2})	FF (%)	η (%)	R_S (Ωcm^2)	R_{SH} (Ωcm^2)
Aged	270 ±23	26.37 ±2.14	32.64 ±2.7	2.32 ±0.59	7.80 ±1.3	23.30 ±3.4
Post HT	300 ±11	30.67 ±1.5	51.19 ±4.6	4.71 ±0.38	2.10 ±0.98	65.00 ±6.8

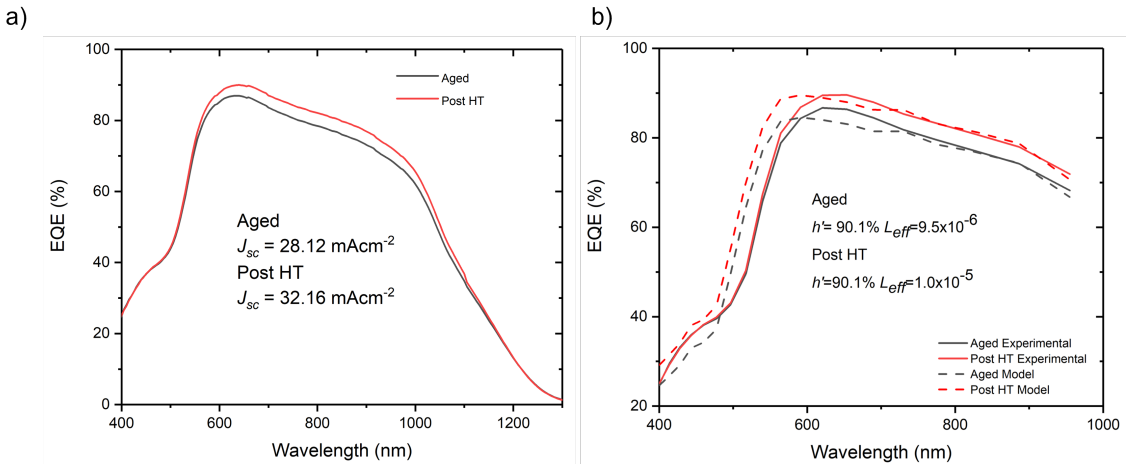

Figure 6.4: EQE spectra for a CZTSSe solar cell when aged and after a HT process of 150 °C for 10 minutes with b) EQE modelling to extract device parameters.

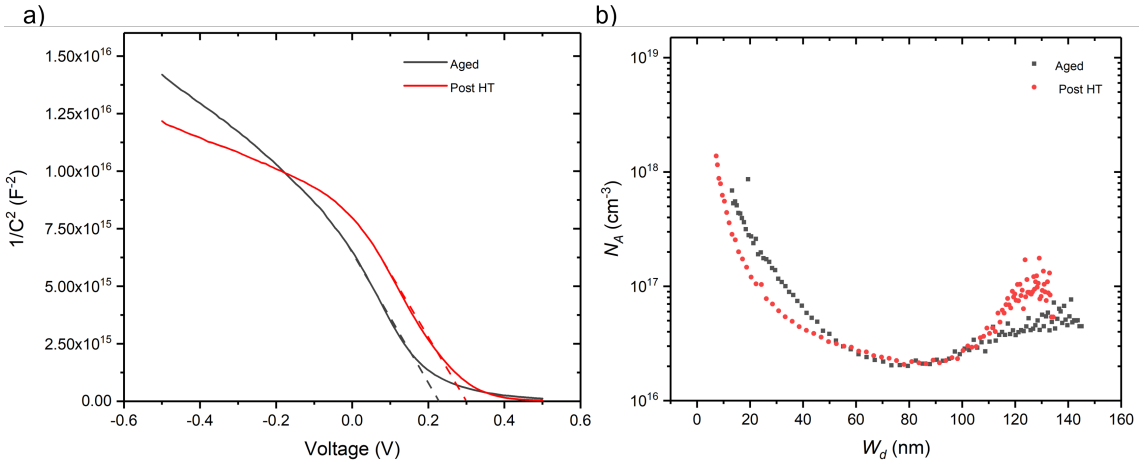

Figure 6.5: a) Mott-Schottky plot and b) depletion width versus the doping concentration plot of a CZTSSe solar cell subject to a HT process of 150 °C for 10 minutes from an aged state to after the HT.

From Table 6.2, the aged device shows poor R_S and R_{SH}, which are detrimental to current extraction. After HT both values are improved. The HT also improves the J_{sc} which is supported by the EQE spectra given in Figure 6.4a. Once annealed, the device demonstrates higher current collection in the 600-1000 nm region, otherwise the EQE spectra can be seen to be the same. In this range, we can assume that the mechanism of recovery in the device arises from the semiconductor absorber layer and the two interfaces that surround it (Mo/CZTSSe and CZTSSe/CdS). Extracting E_g from the EQE measurements yields values of 1.012 eV when aged and 1.024 eV post anneal, suggesting that there is a small change in the absorber composition in order to vary the band gap. One potential cause of this is Na accumulation in the Cu states of the material, yielding a band gap increase [128]. Applying the EQE model detailed in Section 3.2.4 and shown in Figure 6.4b, h' and L_{eff} are calculated for both the annealed cell and the aged cell. L_{eff} is almost identical with L_{eff}=9.5$\times 10^{-6}$ cm for the aged cell and 1.0$\times 10^{-5}$ cm for the annealed cell meaning there is little to no change in the effective lifetime of the carriers in the device. The aged cell demonstrates a h'=90.1% where as in the annealed cell h'=93.5%. This change in surface recombination suggests an improvement at the CZTSSe/CdS interface alongside the improvement of the absorber material seen from JV and EQE analysis. This is attributed to diffusion across the hetero junction of Zn and Cd and therefore Cd alloying in the absorber layer, which is seen in this work [21, 125, 128]. Additionally Na accumulation within the heterojunction region also improve device performance with HT [128, 130]. Both of which show a reduction in interface recombination leading to an

improved J_{sc}.

CV measurements are shown in Figure 6.5a and b to investigate these mechanisms further. The V_{bi} is extracted from the linear fit of a Mott-Schottky plot, shown in Figure 6.5a, taking the intercept of the x axis given in further detail in Section 3.2.5. The V_{bi} shows an increase with HT from 0.23 to 0.30 V. This explains the increase in V_{oc} observed with HT, as a higher voltage in the depletion layer of the device yields a higher overall V_{oc}. An increase in V_{bi} can be attributed to an increase in the W_d, which can be calculated using Equation 3.10 at 0 bias. Here, an increase in W_d is seen from the aged device to the post HT device of 97 nm to 108 nm respectively. The improvement in W_d is assumed to be from a reduction in recombination in the space charge region (SCR) of the device resultant of an improvement of the CZTSSe/CdS interface as previously discussed. The increase in V_{bi} can also be attributed to charge separation which again, improves the V_{oc}. To quantify the alloying or reordering at the hetero junction, the carrier concentration N_A was calculated and plotted across the depletion width shown in Figure 6.5b. It is observed that N_A increases with HT from 2×10^{16} to 4×10^{16} cm^{-3}. This supports the theory presented here that the improvement and recovery of the device performance can be attributed to diffusion of Zn and Cd during the HT process and outlines the importance of the CZTSSe/CdS junction interface and provides a route to aged device recovery supported through TEM measurements detailed elsewhere [125].

6.6 Heat Treatment on Mo Foil

As previously discussed in Chapter 1, there is a crucial importance in developing flexible solar cell devices for deployment and long term solar cell use. An important aspect of this, is the degradation seen in flexible cell devices and their stability. The previously reported sections presented a methodology to recover aged devices and propose a mechanism in which to explain how this is done on SLG cells, however, it is not currently understood how a HT affects flexible device performance and whether any degradation can be recovered.

The optoelectronic properties can be seen below in Table 6.3 of a flexible CZTSSe device newly fabricated (New), aged to 6 months and post 150 °C HT for 10 minutes in pure Ar atmosphere. Notably here, the aged devices had been left in ambient lab condi-

tions the same of that of the CZTSSe fabricated on SLG device measured in Section 6.3 but for a much longer time (5 months) in comparison. It can be seen that the degradation that occurs in Mo foil cells is not as significant as in SLG cells. The mechanism as to why this happens is not yet fully understood. Also to note, in Table 6.3 the highlighted row outlines the cell performance after HT which is among one of the highest efficiency values for CZTSSe cells fabricated on Mo foil with nanoparticle inks, specifically without any alkali doping.

Table 6.3: Average optoelectronic properties of a CZTSSe solar cell when first fabricated (New), then aged and then finally after a HT of 150 °C for 10 minutes (post HT).

	V_{oc} (mV)	J_{sc} (mAcm^{-2})	FF (%)	η (%)	R_S (Ωcm^2)	R_{SH} (Ωcm^2)
New	270 $\pm$20.0	28.1 $\pm$3.2	29.5 $\pm$5.1	2.2 $\pm$0.9	8.1	17.6
Aged	267 $\pm$12.3	24.1 $\pm$2.5	33.7 $\pm$3.2	2.2 $\pm$0.70	7.6	26.8
Post HT	325 $\pm$19.0	31.9 $\pm$1.5	44.08 $\pm$4.6	4.56 $\pm$1.0	3.7	57.9

CZTSSe solar cell devices on Mo foil show an improvement in the measured optoelectronic properties once subject to a 150 °C HT after ageing. Interestingly, we also show that the device performance after HT not only recovers the initial reading from when the device was first fabricated, but exceeds the initial optoelectronic properties. The Mo foil device generates a V_{oc} of 325 mV, which could be attributed to reduced recombination and improvement of the CZTSSe/CdS interface as previously discussed. To investigate the role Na plays with HT of flexible solar cells, a systemic study was completed detailed in Section 6.6.1.

6.6.1 Sodium Doping effects with HT

Highly cited in literature [112, 134, 135] and discussed in this work in Chapter 4, is the device improvement seen when CZTSSe solar cells fabricated on Mo foil are doped with Na. Xie *et al*, propose that sodium within the device is a key factor in the HT process, causing passivisation of grain boundaries by saturation of dangling bonds at the surface further improving the CZTSSe/CdS interface and producing a favourable band allignment [128, 130]. To assess the impact Na doping has on HT, 6 CZTSSe devices were fabricated on Mo foil, four of which using the NaF doping method outlined in Section

4.1.1 with varying amounts of NaF powder added (0, 1.9, 3.2 and 6.3 mg). Additionally, a device was fabricated with the SLG doping method also outlined in Section 4.1.1. The devices were allowed to age for 6 months for the degradation process to occur and were then subject to a HT process in Ar at 150 °C for 10 minutes. The JV characteristics of the devices before and after the HT are shown in Figure 6.6. Similarly to previously, the JV curves are given with relation to the aged curve as each cell is fabricated identically but demonstrates variation in properties when measured. The devices with smaller NaF doping amounts (1.9 and 3.2 mg) alongside the SLG doped device yield the best improvement in optoelectronic properties with HT, however the 6.3 mg doped device shows significantly less improvement. An excess of Na in the active region of the absorber is found to significantly decrease the device *FF* which is assumed to be the cause in the poor performance of the device doped it 6.3 mg of NaF powder. The device doped with SLG yields the highest normalised percentage increase in the optoelectronic properties, with the PCE increasing from 2.62% when first fabricated, to 2.32% when aged and then finally 4.1% post HT. This increase in PCE is attributed to an increase in V_{oc} which is increased from 240 to 300 mV in the champion device. Similarly to cells on SLG discussed earlier, this correlates with an increase in W_d arising from Cd/Zn diffusion and improvement in the CZTSSe/CdS interface and Na accumulation at the junction interface, also seen with the SLG solar cell devices and extracted from the EQE simulations.

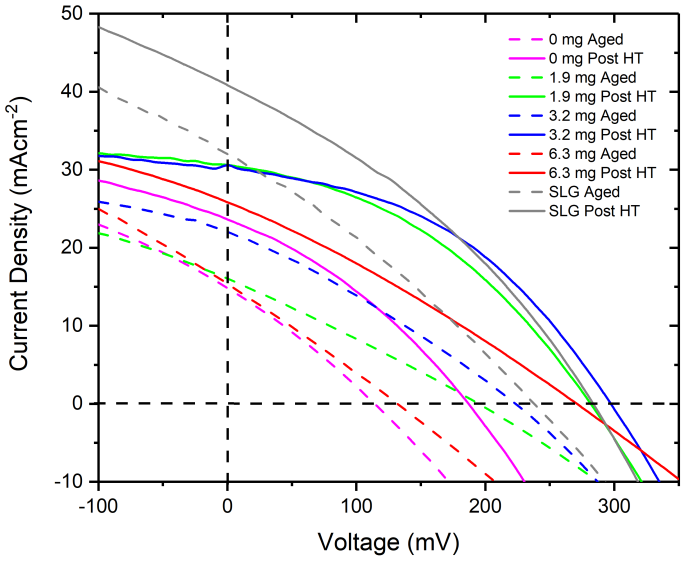

Figure 6.6: JV properties for the champion devices of CZTSSe solar cells with various doping amounts and inclusion methods subject to a HT of 150 °C for 10 minutes.

Finally, the two best performing devices from the HT process on Mo foil are compared here to understand the main driving mechanism of device recovery on Mo foil solar cells. Which here, is a Mo foil device with no doping and a Mo foil device with SLG doping. The normalised percentage increase in the optoelectronic properties from newly fabricated to post HT in Figure 6.7a and from aged to post HT in Figure 6.7b.

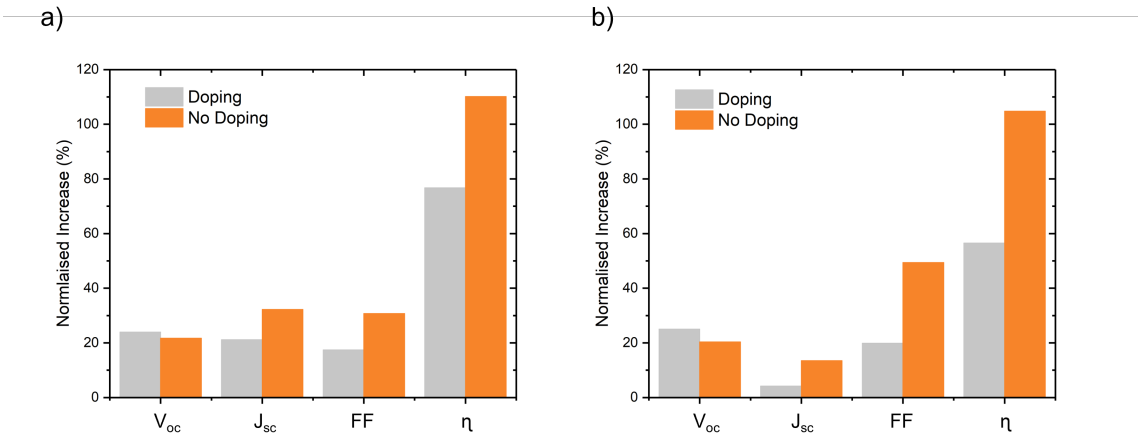

Figure 6.7: Normalised change in percentage optoelectronic properties of devices fabricated on Mo foil with and without doping after a HT process. The comparison between a) new fabricated to post HT and b) aged to post HT is shown.

The Mo foil device with no doping shows a greater performance recovery and improvement across the optoelectronic properties. It is from this, it is assumed the main driving force behind device recovery on CZTSSe solar cells fabricated from Mo foil is the diffusion of Zn and Cd and improvement of the CZTSSe/CdS interface that arises from this, as previously reported [125]. Na incorporation plays a limited role here, as the doped cell shows a significantly less performance improvement to that of the non doped equivalent. However, V_{oc} values show very close comparisons between doped and no doping, with the percentage increase being higher for the doped cell from aged state to post HT. The mechanism thought to be behind the increase in V_{oc} is the charge separation and increase in the depletion width. It is assumed here that this is affected by doping as an increase in Na concentration is formed in the bulk of the material.

As an additional study, newly fabricated devices were tested with the HT process identical to that the ages cells are subject. Newly fabricated devices, regardless of substrate, showed no improvement when subject to HT and demonstrated identical optoelectronic properties before and after the HT process. The conclusion can then be drawn, that the

HT demonstrated is a key recovery process, and not an improvement in the CZTSSe solar cell devices.

6.7 Summary

In summary, due to an improvement in device resistances and poor charge extraction, a degradation is seen in CZTSSe solar cells fabricated from nanoparticle inks on both SLG substrates and Mo foil substrates. The degradation however, is not as severe on the Mo foil substrate which does not contain any Na. After application of HT in a pure Ar atmosphere at 150 °C for 10 minutes, all devices show improvement in their optoelectronic properties. Devices on Mo foil are found to even exceed the newly fabricated properties. This improvement has been attributed to an improvement at the absorber/buffer layer interface alongside Cd and Zn diffusion yielding a favourable band alignment. This study outlines the importance of a HT process for competitive device performance on Mo foil and highlights the importance of elemental inter diffusion.

Chapter 7

Conclusion and Outlook

7.1 Thesis Summary

This thesis presents new research in thin film kesterite solar cells focusing on Mo foil substrates. The devices were synthesised using CZTS nanoparticle inks prepared using a hot injection of metallic precursors in surfactant method for low toxicity, highly scalable and low cost solar cell fabrication. In particular, three aspects were explored: alkali doping of flexible devices; mechanical testing for a wide application range; and device recovery mechanisms.

CZTSSe solar cells demonstrate higher performance with alkali doping. This is because Na is reported to passivate grain boundaries and therefore reduce non-radiative recombination within the absorber layer. One route to including Na doping on Mo foil, which does not supply an intrinsic Na source as SLG does, devices is through solution based NaF dissolved into the nanoparticle inks or through SLG present during a high temperature fabrication step. In Chapter 4, an investigation of the NaF powder method is presented and compared with a SLG during selenisation doping method. Both doping methods were shown to have no effect on the CZTSSe absorber composition, allowing the absorbers to remain within the idealised area for high efficiency devices using the pre existing fabrication methods. It was shown using CV measurements, that using NaF powder or SLG as a doping source is an effective doping method resulting in a higher doping concentration compared to an non-doped reference. It was found that, an increasing amount of NaF powder added to the CZTS nanoparticle inks during concentration yields a PCE increase from 2.2% with no doping to 2.9% with a 0.1 mol/L doping amount. By inclusion of

SLG in the annealing furnace during the conversion of S to Se to create a thick CZTSSe absorber layer also demonstrated an improved PCE of 3%. The increase in PCE was found to be driven by an increase in V_{oc}, J_{sc} and R_{SH}. The driving mechanism behind the increase in both J_{sc} and R_{SH} is the reduction in non-radiative recombination via passivisation of grain boundaries in the semiconductor film. This is supported by a decrease in h' and an increase in L_{eff} obtained from EQE modelling. EQE experiments also showed fewer losses in the CdS buffer layer with higher Na doping, arising from an improved CZTSSe/CdS interface. Na can occupy the V_{Cu} site, resulting from Cu-depleted surface and thereby improving the interface and device.

In addition to Na doping Chapter 4 also presented a method of doping CZTS thin films using a Sb_2Se_3 layer deposited beneath the absorber layer. Sb_2Se_3 forms a semi-liquid phase at high temperatures, in the range used for CZTSSe selenisation, and therefore has been shown to diffuse into the CZTSSe absorber layer. This diffusion increases the percentage of Sb in the device and is shown here to promote grain growth using SEM images. Doping a CZTSSe absorber layer with a 200 nm layer of Sb_2Se_3 yielded a homogeneous large grain thin film that was free from pin-holes or voids.

Having established a method to introduce Na to flexible foil based devices, Chapter 5 assessed the device performance under mechanical bending and load cycle testing. Bending CZTSSe solar cells up to a ROC of 64 mm showed no degradation in the device performance and at a 64 mm ROC a slight increase in device performance is seen. This was quantitatively attributed to a reduction in current shunting pathways in the device supported by an increase in R_{SH}. The CZTSSe devices show a PCE of 3.91% when flat increasing to 4.31% when bent. Above an ROC of 64 mm the device performance degrades and this was shown to be due to cracking of the brittle ITO layer observed by optical microscope images. In addition, the evolution of the device performance after a 100 cycle bending test to 64 mm ROC was presented: A higher R_{SH} is preserved and a PCE of 4.35% is shown without any degradation in performance. This provides evidence that the devices are robust and may be suited to new application.

The cutting of CZTSSe solar cells to desired sizes upon cell completion is also detailed in Chapter 5. The devices were fabricated by slot-die deposition of a CZTS nanoparticle ink onto a flexible Mo foil substrate 25 $\times$ 75 mm. The completed devices were then cut

into three 25 × 25 mm and demonstrated that the devices can be cut without degradation. This work shows potential for specific application requirements and designer freedom.

Chapter 6 showed the effect of a post-annealing heat treatment on aged CZTSSe devices that recovered the initial device performance. Degradation was observed in all of the optoelectronic properties when CZTSSe solar cells are aged in ambient laboratory conditions. Over 6 weeks, the device PCE fell from 3.1% to 1.9%. An annealing step of 150 °C for 10 minutes in Ar was found to recover the initial device performance characteristics. In particular, R_{SH} and R_S demonstrated an improvement with heat treatment. In addition, JV, EQE and EQE modelling, showed recovery of J_{sc}, assumed to arise from an improvement in the absorber layer due to Cd alloying. The increase in V_{oc} stems from an increase in V_{bi} observed from CV measurements. CZTSSe devices fabricated on Mo foil show less degradation over time to those on SLG. The Mo foil devices do, however, show the same recovery process as the SLG samples. It is also shown in this work that Na has a limited role in the recovery process of these devices. Mo foil devices with no doping show comparable recovery to the doped devices. The main driving force of the recovery is therefore concluded to be the interface diffusion.

7.2 Future Work

From the work completed in this thesis, several areas for further work have identified. Suggestions to further the flexible CZTSSe progression include further investigating into Sb_2Se_3 doping of flexible CZTSSe solar devices. The work achieved in Chapter 4 shows potential for a higher PCE on completed devices for which, further work is needed. In addition to this, investigation into different alkali doping materials to be incorporated into the nanoparticle inks such as Rb and K merits investigation.

Secondly, the device degradation of a flexible CZTSSe in curved state is a potential for further investigation. Mo foil devices, when flat, are shown here to degrade at a slower level to rigid SLG devices. For long term use of CZTSSe solar cells in flexible application, this degradation in curved state is crucial to understand and mitigate.

Flexible CZTSSe devices still lag behind the rigid alternatives in terms of optoelectronic

properties and PCE. Further work is required to address this and achieve comparable performance. One route to achieving this is various flexible substrates to avoid impurities from the Mo foil diffusing into the absorber layer or a barrier layer on the foil to block diffusion.

The CdS buffer also lacks optimisation. There is potential to explore alternative buffer layers to improve the absorber/buffer interface whilst eliminating toxic materials from the device. Alternatives based on Zn or Ti can be introduced to the solar cell fabrication process.

Finally, there remains limited to no experimental work completed on creating a CZTSSe tandem cell, either combined with other CZTSSe layers with a tuned band gap or other materials such as perovskites. Due to the flexibility of the CZTSSe band gap makes it an attractive candidate for tandem cell application. In addition to this, a tandem cell on a flexible substrate is also yet to be observed and could be key for advancing the VIPV and BIPV markets.

Bibliography

[1] Royal Dutch Shell, "Shell Scenarios: Sky - Meeting the goals of the Paris agreement," *Royal Dutch Shell Strategic Report*, 2018.

[2] F. Kessler and D. Rudmann, "Technological aspects of flexible CIGS solar cells and modules," *Solar Energy*, vol. 77, no. 6, pp. 685–695, 2004.

[3] X. Li, P. Li, Z. Wu, D. Luo, H.-Y. Yu, and Z.-H. Lu, "Review and perspective of materials for flexible solar cells," *Materials Reports: Energy*, vol. 1, no. 1, p. 100001, 2021.

[4] K.-J. Yang, S. Kim, S.-Y. Kim, K. Ahn, D.-H. Son, S.-H. Kim, S.-J. Lee, Y.-I. Kim, S.-N. Park, S.-J. Sung, D.-H. Kim, T. Enkhbat, J. Kim, C.-W. Jeon, and J.-K. Kang, "Flexible $Cu_2ZnSn(S,Se)_4$ solar cells with over 10% efficiency and methods of enlarging the cell area,"

[5] M. A. Green, E. D. Dunlop, J. Hohl-Ebinger, M. Yoshita, N. Kopidakis, and X. Hao, "Solar cell efficiency tables (version 59)," *Progress in Photovoltaics: Research and Applications*, vol. 30, pp. 3–12, Jan 2022.

[6] M. Nakamura, K. Yamaguchi, Y. Kimoto, Y. Yasaki, T. Kato, and H. Sugimoto, "Cd-Free $Cu(In,Ga)(Se,S)_2$ Thin-Film Solar Cell With Record Efficiency of 23.35%," *Ieee*, vol. 9, no. 6, pp. 1863–1867, 2019.

[7] S. Giraldo, Z. Jehl, M. Placidi, V. Izquierdo-Roca, A. Pérez-Rodríguez, and E. Saucedo, "Progress and Perspectives of Thin Film Kesterite Photovoltaic Technology: A Critical Review," 2019.

[8] W. Chen, Y. Zhu, J. Xiu, G. Chen, H. Liang, S. Liu, H. Xue, E. Birgersson, J. W. Ho, X. Qin, J. Lin, R. Ma, T. Liu, Y. He, A. M.-C. Ng, X. Guo, Z. He, H. Yan, A. B. Djurišić, and Y. Hou, "Monolithic perovskite/organic tandem solar cells with

23.6% efficiency enabled by reduced voltage losses and optimized interconnecting layer," *Nature Energy*, 2022.

[9] D. B. Straus, S. Guo, M. Abeykoon, R. J. Cava, D. B. Straus, S. Guo, R. J. Cava, and A. M. Abeykoon, "Understanding the Instability of the Halide Perovskite CsPbI3 through Temperature-Dependent Structural Analysis," *Advanced Materials*, vol. 32, no. 32, p. 2001069, 2020.

[10] Z. Shi and A. H. Jayatissa, "Perovskites-Based Solar Cells: A Review of Recent Progress, Materials and Processing Methods.," *Materials (Basel, Switzerland)*, vol. 11, May 2018.

[11] S. A. Khalate, R. S. Kate, and R. J. Deokate, "A review on energy economics and the recent research and development in energy and the Cu_2ZnSnS_4 (CZTS) solar cells: A focus towards efficiency," *Solar Energy*, vol. 169, pp. 616–633, 2018.

[12] X. Liu, Y. Feng, H. Cui, F. Liu, X. Hao, G. Conibeer, D. B. Mitzi, and M. Green, "The current status and future prospects of kesterite solar cells: a brief review," *Progress in Photovoltaics: Research and Applications*, vol. 24, no. 6, pp. 879–898, 2016.

[13] H. Katagiri, K. Jimbo, W. S. Maw, K. Oishi, M. Yamazaki, H. Araki, and A. Takeuchi, "Development of CZTS-based thin film solar cells," *Thin Solid Films*, vol. 517, no. 7, pp. 2455–2460, 2009.

[14] D. B. Mitzi, O. Gunawan, T. K. Todorov, K. Wang, and S. Guha, "The path towards a high-performance solution-processed kesterite solar cell," *Solar Energy Materials and Solar Cells*, vol. 95, no. 6, pp. 1421–1436, 2011.

[15] K. S. Gour, V. Karade, P. Babar, J. Park, D. M. Lee, V. N. Singh, and J. H. Kim, "Potential Role of Kesterites in Development of Earth-Abundant Elements-Based Next Generation Technology," *Solar RRL*, vol. 5, no. 4, p. 2000815, 2021.

[16] W. Wang, M. T. Winkler, O. Gunawan, T. Gokmen, T. K. Todorov, Y. Zhu, and D. B. Mitzi, "Device Characteristics of CZTSSe Thin-Film Solar Cells with 12.6% Efficiency," *Advanced Energy Materials*, vol. 4, p. 1301465, May 2014.

[17] W. Li, J. M. R. Tan, S. W. Leow, S. Lie, S. Magdassi, and L. H. Wong, "Recent Progress in Solution-Processed Copper-Chalcogenide Thin-Film Solar Cells," *Energy Technology*, vol. 6, pp. 46–59, Jan 2018.

[18] C. J. Hages, M. J. Koeper, C. K. Miskin, K. W. Brew, and R. Agrawal, "Controlled Grain Growth for High Performance Nanoparticle-Based Kesterite Solar Cells," *Chemistry of Materials*, vol. 28, no. 21, pp. 7703–7714, 2016.

[19] C. Y. Peng, T. P. Dhakal, P. Rajbhandari, S. Garner, P. Cimo, S. Lu, and C. R. Westgate, "Flexible CZTS solar cells on flexible Corning® Willow® Glass substrates," in *2014 IEEE 40th Photovoltaic Specialist Conference, PVSC 2014*, pp. 409–412, Institute of Electrical and Electronics Engineers Inc., 2014.

[20] K. W. Brew, S. M. McLeod, S. M. Garner, and R. Agrawal, "Improving efficiencies of Cu_2ZnSnS_4 nanoparticle based solar cells on flexible glass substrates," *Thin Solid Films*, 2017.

[21] K. Sun, F. Liu, C. Yan, F. Zhou, J. Huang, Y. Shen, R. Liu, and X. Hao, "Influence of sodium incorporation on kesterite Cu_2ZnSnS_4 solar cells fabricated on stainless steel substrates," *Solar Energy Materials and Solar Cells*, vol. 157, pp. 565–571, 2016.

[22] Y. Zhang, Q. Ye, J. Liu, H. Chen, X. He, C. Liao, J. Han, H. Wang, J. Mei, and W. Lau, "Earth-abundant and low-cost CZTS solar cell on flexible molybdenum foil," *RSC Advances*, vol. 4, pp. 23666–23669, 2014.

[23] J.-H. Min, W.-L. Jeong, K. Kim, J.-S. Lee, K.-P. Kim, J. Kim, M. Gil Gang, C. Woo Hong, J. Hyeok Kim, and D.-S. Lee, "Flexible High-Efficiency CZTSSe Solar Cells on Diverse Flexible Substrates via an Adhesive-Bonding Transfer Method," *ACS Appl. Mater. Interfaces*, vol. 12, pp. 8189–8197, 2020.

[24] A. Wang, N. L. Chang, K. Sun, C. Xue, R. J. Egan, J. Li, C. Yan, J. Huang, H. Rong, C. Ramsden, and X. Hao, "Analysis of manufacturing cost and market niches for Cu_2ZnSnS_4(CZTS) solar cells," *Sustainable Energy Fuels*, vol. 5, no. 4, pp. 1044–1058, 2021.

[25] A. Becquerel, "Recherches sur les effets de la radiation chimique de la lumiere solaire au moyen des courants electriques," *Comptes Rendus de LAcademie des Sciences*, vol. 9, pp. 145–149, 1839.

[26] W. G. Adams and R. E. Day, "The Action of Light on Selenium.," *Source: Proceedings of the Royal Society of London*, vol. 25, pp. 113–117.

[27] J. Perlin, "From Space to Earth: The Story of Solar Electricity," 1999.

[28] W. Schottky, "Zur Halbleitertheorie der Sperrschicht- und Spitzengleichrichter," *Zeitschrift für Physik 1939 113:5*, vol. 113, pp. 367–414, May 1939.

[29] N. F. Mott and F. R. S. H. H. Wills Physical, "The theory of crystal rectifiers," *Proceedings of the Royal Society of London. Series A. Mathematical and Physical Sciences*, vol. 171, pp. 27–38, May 1939.

[30] J. Nelson, "The Physics of solar cells," *Journal of Applied Physics*, vol. 50, no. 8, pp. 5356–5370, 2003.

[31] R. T. Tung, "The physics and chemistry of the Schottky barrier height," *Applied Physics Reviews*, vol. 1, no. 1, 2014.

[32] D. Chapin, C. S. Fuller, and G. L. Pearson, "A New Silicon p-n Junction Photocell for Converting Solar Radiation into Electrical Power," *Journal of Applied Physics*, vol. 25, no. 5, pp. 676–677, 1954.

[33] P. S. Jha, "Dawn of the solar age : an end to global warming and to fear," p. 280.

[34] V. Petrova-Koch, "High-Efficient Low-Cost Photovoltaics," *Springer*, vol. 140, 2008.

[35] I. E. AGENCY, "Renewables 2021: Analysis and forecast to 2026," 2021.

[36] "Photovoltaic Research — NREL." https://www.nrel.gov/pv/. Accessed: 2021-12-20.

[37] W. Shockley and H. J. Queisser, "Detailed Balance Limit of Efficiency of p-n Junction Solar Cells," *Journal of Applied Physics*, vol. 32, no. 3, pp. 510–519, 1961.

[38] S. Rühle, "Tabulated values of the Shockley–Queisser limit for single junction solar cells," *Solar Energy*, vol. 130, pp. 139–147, 2016.

[39] W. Bauer and G. Westfall, *University Physics with Modern Physics*. McGraw-Hill, 2011.

[40] R. W. Miles, G. Zoppi, and I. Forbes, "Inorganic photovoltaic cells," *Materials Today*, vol. 10, no. 11, pp. 20–27, 2007.

[41] C. Hu and R. M. White, "Solar cells : from basics to advanced systems," 2012.

[42] R. van. Overstraeten and R. P. Mertens, "Physics, technology and use of photovoltaics," p. 278, 1986.

[43] E. Burstein, "Anomalous Optical Absorption Limit in InSb," *Physical Review*, vol. 93, no. 3, p. 632, 1954.

[44] R. W. Miles, K. M. Hynes, and I. Forbes, "Photovoltaic solar cells: An overview of state-of-the-art cell development and environmental issues," *Progress in Crystal Growth and Characterization of Materials*, vol. 51, pp. 1–42, Jan 2005.

[45] K. Ito and T. Nakazawa, "Electrical and optical properties of stannite-type quaternary semiconductor thin films," *Japanese Journal of Applied Physics*, vol. 27, no. Part 1, No. 11, pp. 2094–2097, 1988.

[46] H. Katagiri, N. Sasaguchi, S. Hando, S. Hoshino, J. Ohashi, and T. Yokota, "Preparation and evaluation of cu_2znsns_4 thin films by sulfurization of eb evaporated precursors," *Solar Energy Materials and Solar Cells*, vol. 49, no. 1, pp. 407–414, 1997.

[47] S. R. Hallt, J. T. Szyma, and J. M. Stewart, "Kesterite, Cu_2(Zn,Fe)SnS+, and stannite, Cuz(FeZn)nsa, structurally similar but distinc materials,"

[48] C. J. Bosson, M. T. Birch, D. P. Halliday, K. S. Knight, A. S. Gibbs, and P. D. Hatton, "Cation disorder and phase transitions in the structurally complex solar cell material Cu_2ZnSnS_4," *Journal of Materials Chemistry A*, vol. 5, no. 32, pp. 16672–16680, 2017.

[49] J. BOSSON, CHRISTOPHER, "Understanding Cu_2ZnSnS_4 as a Photovoltaic Absorber for the Future of Solar Electricity," 2018.

[50] M. Jiang and X. Yan, "Cu_2ZnSnS_4 Thin Film Solar Cells: Present Status and Future Prospects," 2013.

[51] M. N. Dimitrievska, F. Boero, A. P. Litvinchuk, S. Delsante, G. Borzone, A. Perez-Rodriguez, and V. Izquierdo-Roca, "Structural Polymorphism in "Kesterite"

Cu_2ZnSnS_4: Raman Spectroscopy and First-principles Calculations Analysis," 2017.

[52] L. E. Valle Rios, K. Neldner, G. Gurieva, and S. Schorr, "Existence of off-stoichiometric single phase kesterite," *Journal of Alloys and Compounds*, vol. 657, pp. 408–413, 2016.

[53] S. Chen, X. G. Gong, A. Walsh, and S. H. Wei, "Electronic structure and stability of quaternary chalcogenide semiconductors derived from cation cross-substitution of II-VI and I-III-VI2 compounds," *Physical Review B - Condensed Matter and Materials Physics*, vol. 79, no. 16, p. 165211, 2009.

[54] X. Zhang, "Solution-processed nanomaterials for applications in photoelectrochemical solar cells," 2015.

[55] S. Siebentritt and S. Schorr, "Kesterites—a challenging material for solar cells," *Progress in Photovoltaics: Research and Applications*, vol. 20, no. 5, pp. 512–519, 2012.

[56] B. Mendis, M. Shannon, M. Goodman, J. Major, R. Claridge, D. Halliday, and K. Durose, "Direct observation of Cu, Zn cation disorder in Cu_2ZnSnS_4 solar cell absorber material using aberration corrected scanning transmission electron microscopy," *Progress in Photovoltaics: Research and Applications*, vol. 22, 2014.

[57] A. Shavel, J. Arbiol, and A. Cabot, "Synthesis of Quaternary Chalcogenide Nanocrystals: Stannite $Cu_2Zn_xSn_ySe_{1+x+2y}$," *Journal of the American Chemical Society*, vol. 132, no. 13, pp. 4514–4515, 2010. PMID: 20232869.

[58] J. B. Li, V. Chawla, and B. M. Clemens, "Investigating the role of grain boundaries in CZTS and CZTSSe thin film solar cells with scanning probe microscopy," *Advanced Materials*, vol. 24, no. 6, pp. 720–723, 2012.

[59] X. Xu, Z. Zhuang, Q. Peng, and Y. Li, "Wurtzite Cu_2ZnSnS_4 nanocrystals: a novel quaternary semiconductor," *Chemical Communications*, vol. 47, no. 11, pp. 3141–3143, 2011.

[60] C. Persson, "Electronic and optical properties of Cu_2ZnSnS_4 and $Cu_2ZnSnSe_4$," *Journal of Applied Physics*, vol. 107, no. 5, 2010.

[61] J. Paier, R. Asahi, A. Nagoya, and G. Kresse, "Cu_2ZnSnS_4 as a potential photovoltaic material: A hybrid Hartree-Fock density functional theory study," *Physical Review B - Condensed Matter and Materials Physics*, vol. 79, no. 11, 2009.

[62] A. Crovetto, O. Hansen, and J. Schou, "Cu_2ZnSnS_4 solar cells: Physics and technology by alternative tracks," 2016.

[63] K. Jimbo, R. Kimura, T. Kamimura, S. Yamada, W. S. Maw, H. Araki, K. Oishi, and H. Katagiri, "Cu_2ZnSnS_4-type thin film solar cells using abundant materials," *Thin Solid Films*, vol. 515, pp. 5997–5999, May 2007.

[64] Y. Wei, D. Zhuang, M. Zhao, Q. Gong, R. Sun, G. Ren, Y. Wu, L. Zhang, X. Lyu, X. Peng, and J. Wei, "An investigation on the relationship between open circuit voltage and grain size for CZTSSe thin film solar cells fabricated by selenization of sputtered precursors," *Journal of Alloys and Compounds*, vol. 773, pp. 689–697, 2019.

[65] T. Kohl, G. Brammertz, J. de Wild, M. Neuwirth, M. Meuris, J. Poortmans, and B. Vermang, "Fabrication of high band gap kesterite solar cell absorber materials for tandem applications," *Thin Solid Films*, vol. 660, pp. 247–252, 2018.

[66] T. Maeda, S. Nakamura, and T. Wada, "First principles calculations of defect formation in in-free photovoltaic semiconductors Cu_2ZnSnS_4 and $Cu_2ZnSnSe_4$," *Japanese Journal of Applied Physics*, vol. 50, 2011.

[67] S. Chen, J. H. Yang, X. G. Gong, A. Walsh, and S. H. Wei, "Intrinsic point defects and complexes in the quaternary kesterite semiconductor Cu_2ZnSnS_4," *Physical Review B - Condensed Matter and Materials Physics*, vol. 81, no. 24, p. 245204, 2010.

[68] S. Chen, X. G. Gong, A. Walsh, and S. H. Wei, "Defect physics of the kesterite thin-film solar cell absorber Cu_2ZnSnS_4," *Applied Physics Letters*, vol. 96, p. 021902, Jan 2010.

[69] S. Chen, A. Walsh, X. G. Gong, and S. H. Wei, "Classification of lattice defects in the kesterite Cu_2ZnSnS_4 and $Cu_2ZnSnSe_4$ earth-abundant solar cell absorbers," *Advanced materials (Deerfield Beach, Fla.)*, vol. 25, no. 11, pp. 1522–1539, 2013.

[70] A. Nagoya, R. Asahi, R. Wahl, and G. Kresse, "Defect formation and phase stability of Cu_2ZnSnS_4 photovoltaic material," *Physical Review B - Condensed Matter and Materials Physics*, vol. 81, no. 11, p. 113202, 2010.

[71] T. Gokmen, O. Gunawan, T. K. Todorov, and D. B. Mitzi, "Band tailing and efficiency limitation in kesterite solar cells," *Applied Physics Letters*, vol. 103, no. 10, p. 103506, 2013.

[72] A. Guchhait, Z. Su, Y. F. Tay, S. Shukla, W. Li, S. W. Leow, J. M. R. Tan, S. Lie, O. Gunawan, and L. H. Wong, "Enhancement of Open-Circuit Voltage of Solution-Processed Cu_2ZnSnS_4 Solar Cells with 7.2vol. 1, no. 6, pp. 1256–1261, 2016.

[73] A. G. Kannan, T. E. Manjulavalli, and J. Chandrasekaran, "Influence of Solvent on the Properties of CZTS Nanoparticles," in *Procedia Engineering*, 2016.

[74] S. Schorr, "Crystallographic Aspects of Cu_2ZnSnS_4 (CZTS)," *Copper Zinc Tin Sulfide-Based Thin-Film Solar Cells*, pp. 53–74, Jan 2015.

[75] W.-C. Huang, S.-Y. Wei, C.-H. Cai, W.-H. Ho, and C.-H. Lai, "The role of Ag in aqueous solution processed $(Ag,Cu)_2ZnSn(S,Se)_4$ kesterite solar cells: antisite defect elimination and importance of Na passivation," *Journal of Materials Chemistry A*, vol. 6, no. 31, pp. 15170–15181, 2018.

[76] A. J. Bard, A. B. Bocarsly, F. R. F. Fan, E. G. Walton, and M. S. Wrighton, "The concept of fermi level pinning at semiconductor/liquid junctions. consequences for energy conversion efficiency and selection of useful solution redox couples in solar devices," *Journal of the American Chemical Society*, vol. 102, no. 11, pp. 3671–3677, 1980.

[77] C. T. Sah, R. N. Noyce, and W. Shockley, "Carrier Generation and Recombination in P-N Junctions and P-N Junction Characteristics," *Proceedings of the IRE*, vol. 45, no. 9, pp. 1228–1243, 1957.

[78] S. Levcenko, J. Just, A. Redinger, G. Larramona, S. Bourdais, G. Dennler, A. Jacob, and T. Unold, "Deep Defects in $Cu_2ZnSn(S,Se)_4$ Solar Cells with Varying Se Content," *Phys. Rev. Applied*, vol. 5, p. 024004, 2016.

[79] D. Miller, C. Warren, O. Gunawan, T. Gokmen, D. Mitzi, and D. Cohen, "Electronically active defects in the $Cu_2ZnSn(Se,S)_4$ alloys as revealed by transient photocapacitance spectroscopy," *Applied Physics Letters*, vol. 101, p. 142106, 2012.

[80] Y. Ma, W. Li, Y. Feng, Z. Li, X. Ma, X. Liu, X. Wu, Y. Zhang, C. Yang, X. Lu, K. Wang, and X. Xiao, "Band bending near grain boundaries of $Cu_2ZnSn(S,Se)_4$ thin films and its effect on photovoltaic performance," *Nano Energy*, vol. 51, pp. 37–44, 2018.

[81] S. Kumar, M. Altosaar, M. Grossberg, and V. Mikli, "Effect of alkali ions (Na+, K+, Cs+) on reaction mechanism of CZTS nano-particles synthesis," *Superlattices and Microstructures*, vol. 116, pp. 54–63, 2018.

[82] Y. Qu, G. Zoppi, R. W. Miles, and N. S. Beattie, "Influence of reaction conditions on the properties of solution-processed Cu_2ZnSnS_4 nanocrystals," *Materials Research Express*, vol. 1, no. 4, p. 045040, 2014.

[83] P. Hidnert and W. B. Gero, "Thermal Expansion of Molybdenum,"

[84] X. Xu, Y. Qu, S. Campbell, M. Le Garrec, B. Ford, V. Barrioz, G. Zoppi, and N. S. N. Beattie, "Solution processing route to Na incorporation in CZTSSe nanoparticle ink solar cells on foil substrate," *Journal of Materials Science: Materials in Electronics*, 2019.

[85] Y. Qu, "$Cu_2ZnSn(S,Se)_4$ Solar cells prepared from $Cu_2ZnSn(S,Se)_4$ nanoparticle inks," *Doctoral Thesis*, 2014.

[86] Y. Qu, G. Zoppi, and N. S. Beattie, "The role of nanoparticle inks in determining the performance of solution processed $Cu_2ZnSn(S,Se)_4$ thin film solar cells," *Progress in Photovoltaics: Research and Applications*, vol. 24, no. 6, pp. 836–845, 2016.

[87] Y. Qu, G. Zoppi, and N. S. Beattie, "Selenization kinetics in $Cu_2ZnSn(S,Se)_4$ solar cells prepared from nanoparticle inks," *Solar Energy Materials and Solar Cells*, vol. 158, pp. 130–137, 2016.

[88] Q. Guo, G. M. Ford, W. C. Yang, B. C. Walker, E. A. Stach, H. W. Hillhouse, and R. Agrawal, "Fabrication of 7.2% efficient CZTSSe solar cells using

CZTS nanocrystals," *Journal of the American Chemical Society*, vol. 132, no. 49, pp. 17384–17386, 2010.

[89] B. E. McCandless and S. S. Hegedus, "Influence of CdS window layers on thin film CdS/CdTe solar cell performance," *undefined*, vol. 2, pp. 967–972, 1991.

[90] B. L. Williams, J. D. Major, L. Bowen, L. Phillips, G. Zoppi, I. Forbes, and K. Durose, "Challenges and prospects for developing CdS/CdTe substrate solar cells on Mo foils," *Solar Energy Materials and Solar Cells*, vol. 124, pp. 31–38, May 2014.

[91] P. Jackson, R. Würz, U. Rau, J. Mattheis, M. Kurth, T. Schlötzer, G. Bilger, and J. H. Werner, "High quality baseline for high efficiency, $Cu(In_{1-x},Ga_x)Se_2$ solar cells," *Progress in Photovoltaics: Research and Applications*, 2007.

[92] S. Swan, "Magnetron sputtering," *1988 Physics in Technology 19 67*.

[93] Tescan, "Sem-mira3," 1999.

[94] J. I. Goldstein, D. E. Newbury, J. R. Michael, N. W. Ritchie, J. H. J. Scott, and D. C. Joy, "Scanning electron microscopy and x-ray microanalysis," *Scanning Electron Microscopy and X-ray Microanalysis*, pp. 1–550, 2017.

[95] Claudionico, "Electron interaction with matter." https://creativecommons.org/licenses/by-sa/4.0.

[96] S. Ninomiya, K. Ichiki, H. Yamada, Y. Nakata, T. Seki, T. Aoki, and J. Matsuo, "Precise and fast secondary ion mass spectrometry depth profiling of polymer materials with large Ar cluster ion beams," *Rapid Communications in Mass Spectrometry*, vol. 23, no. 11, pp. 1601–1606, 2009.

[97] J. De Wild, E. Kalesaki, E. V. Robert, and P. J. Dale, "Quantum Efficiency Measurements and Modeling as Tools to Monitor Air Annealing of Cu2SnS3 Solar Cells," *IEEE Journal of Photovoltaics*, 2017.

[98] S. K. Saha, A. Guchhait, and A. J. Pal, "Cu_2ZnSnS_4 (CZTS) nanoparticle based nontoxic and earth-abundant hybrid pn-junction solar cells," *Physical Chemistry Chemical Physics*, vol. 14, no. 22, pp. 8090–8096, 2012.

[99] M. Göken, R. Sakidja, W. Nix, and J. Perepezko, "Microstructural mechanical properties and yield point effects in mo alloys," *Materials Science and Engineering A-structural Materials Properties Microstructure and Processing - MATER SCI ENG A-STRUCT MATER*, vol. 319, pp. 902–908, 2001.

[100] A. Gerthoffer, C. Poulain, F. Roux, F. Emieux, L. Grenet, and S. Perraud, "CIGS solar cells on ultra-thin glass substrates: Determination of mechanical properties by nanoindentation and application to bending-induced strain calculation," *Solar Energy Materials and Solar Cells*, 2017.

[101] S. F. L. for Materials Science, "Efficiency of flexible CIGS solar cells measured at record 21.4%,"

[102] S. Haass, C. Andrés, R. Figi, C. Schreiner, M. Bürki, Y. Romanyuk, and A. Tiwari, "Complex interplay between absorber composition and alkali doping in high-efficiency kesterite solar cells," *Advanced Energy Materials*, vol. 8, p. 1701760, 2017.

[103] G. Altamura, M. Wang, and K.-L. Choy, "Influence of alkali metals (Na, Li, Rb) on the performance of electrostatic spray-assisted vapor deposited $Cu_2ZnSn(S,Se)_4$ solar cells," *Scientific Reports*, vol. 6, p. 22109, 2016.

[104] T. Maeda, A. Kawabata, and T. Wada, "First-principles study on alkali-metal effect of Li, Na, and K in Cu_2ZnSnS_4 and Cu_2ZnSnS_4," *physica status solidi (c)*, vol. 12, 2015.

[105] P. Blösch, S. Nishiwaki, L. Kranz, C. M. Fella, F. Pianezzi, T. Jäger, C. Adelhelm, E. Franzke, S. Buecheler, and A. N. Tiwari, "Sodium-doped molybdenum back contact designs for $Cu(In,Ga)Se_2$ solar cells," *Solar Energy Materials and Solar Cells*, 2014.

[106] T. Gershon, B. Shin, N. Bojarczuk, M. Hopstaken, D. B. Mitzi, and S. Guha, "The Role of Sodium as a Surfactant and Suppressor of Non-Radiative Recombination at Internal Surfaces in Cu_2ZnSnS_4," *Advanced Energy Materials*, vol. 5, no. 2, p. 1400849, 2015.

[107] R. H. Doremus, "Exchange and Diffusion of Ions in Glass," vol. 68, no. 8, pp. 2212–2218, 1964.

[108] S. López-Marino, Y. Sánchez, M. Espíndola-Rodríguez, X. Alcobé, H. Xie, M. Neuschitzer, I. Becerril, S. Giraldo, M. Dimitrievska, M. Placidi, L. Fourdrinier, V. Izquierdo-Roca, A. Pérez-Rodríguez, and E. Saucedo, "Alkali doping strategies for flexible and light-weight $Cu_2ZnSnSe_4$ solar cells," *Journal of Materials Chemistry A*, vol. 4, no. 5, pp. 1895–1907, 2016.

[109] P. Salomé, V. Fjällström, A. Hultqvist, and M. Edoff, "Na doping of CIGS solar cells using low sodium-doped mo layer," *IEEE Journal of Photovoltaics*, vol. 3, no. 1, pp. 509–513, 2013.

[110] I. Becerril-Romero, L. Acebo, F. Oliva, V. Izquierdo-Roca, S. López-Marino, M. Espíndola-Rodríguez, M. Neuschitzer, Y. Sánchez, M. Placidi, A. Pérez-Rodríguez, E. Saucedo, and P. Pistor, "CZTSe solar cells developed on polymer substrates: Effects of low-temperature processing," *Progress in Photovoltaics: Research and Applications*, vol. 26, no. 1, pp. 55–68, 2018.

[111] E. Ghorbani, J. Kiss, H. Mirhosseini, M. Schmidt, J. Windeln, T. D. Kühne, and C. Felser, "Insights into Intrinsic Defects and the Incorporation of Na and K in the $Cu_2ZnSnSe_4$ Thin-Film Solar Cell Material from Hybrid-Functional Calculations," *Journal of Physical Chemistry C*, vol. 120, no. 4, pp. 2064–2069, 2016.

[112] X. Xu, *Flexible $Cu_2ZnSn(S,Se)_4$ solar cells made from nanoparticle inks*. PhD thesis, Northumbria University, 2019.

[113] G. Altamura, M. Wang, and K. L. Choy, "Influence of alkali metals (Na, Li, Rb) on the performance of electrostatic spray-assisted vapor deposited $Cu_2ZnSn(S,Se)_4$ solar cells," *Scientific Reports 2016 6:1*, vol. 6, no. 1, pp. 1–9, 2016.

[114] S. G. Haass, C. Andres, R. Figi, C. Schreiner, M. Bürki, Y. E. Romanyuk, A. N. Tiwari, S. G. Haass, C. Andres, Y. E. Romanyuk, A. N. Tiwari, R. Figi, C. Schreiner, and M. Bürki, "Complex Interplay between Absorber Composition and Alkali Doping in High-Efficiency Kesterite Solar Cells," *Advanced Energy Materials*, vol. 8, no. 4, p. 1701760, 2018.

[115] Y. S. Lee, T. Gershon, O. Gunawan, T. K. Todorov, T. Gokmen, Y. Virgus, and S. Guha, "Cu_2ZnSnS_4 Thin-Film Solar Cells by Thermal Co-evaporation with 11.6% Efficiency and Improved Minority Carrier Diffusion Length," *Advanced Energy Materials*, vol. 5, no. 7, p. 1401372, 2015.

[116] C. K. Miskin, W.-C. Yang, C. J. Hages, N. J. Carter, C. S. Joglekar, E. A. Stach, and R. Agrawal, "9.0% efficient $Cu_2ZnSn(S,Se)_4$ solar cells from selenized nanoparticle inks," *Progress in Photovoltaics: Research and Applications*, vol. 23, pp. 654–659, May 2015.

[117] F. Pianezzi, P. Reinhard, A. Chirilă, B. Bissig, S. Nishiwaki, S. Buecheler, and A. N. Tiwari, "Unveiling the effects of post-deposition treatment with different alkaline elements on the electronic properties of CIGS thin film solar cells," *Physical chemistry chemical physics : PCCP*, vol. 16, no. 19, pp. 8843–8851, 2014.

[118] A. Nakane, H. Tampo, M. Tamakoshi, S. Fujimoto, K. M. Kim, S. Kim, H. Shibata, S. Niki, and H. Fujiwara, "Quantitative determination of optical and recombination losses in thin-film photovoltaic devices based on external quantum efficiency analysis," *Journal of Applied Physics*, vol. 120, no. 6, p. 064505, 2016.

[119] L. Sun, H. Shen, J. Yang, H. Huang, A. Raza, and Q. Zhao, "Performance enhancement of $Cu_2ZnSn(S,Se)_4$ solar cell by inserting Sb and Sb_2Se_2 doping layer at the bottom of CZTS precursor," *Materials Research Express*, vol. 6, p. 125920, Jan 2020.

[120] Y. Ota, K. Araki, A. Nagaoka, and K. Nishioka, "Curve correction of vehicle-integrated photovoltaics using statistics on commercial car bodies," *Progress in Photovoltaics: Research and Applications*, 2021.

[121] Q. Tian, X. Xu, L. Han, M. Tang, R. Zou, Z. Chen, M. Yu, J. Yang, and J. Hu, "Hydrophilic cu2znsns4 nanocrystals for printing flexible, low-cost and environmentally friendly solar cells," *CrystEngComm*, vol. 14, pp. 3847–3850, 03 2012.

[122] Z. Y. W. L. Q. Y. C. Z. Q. Z. X. W. Y. L. . S. C. Hui Deng, Quanzhen Sun, "Novel symmetrical bifacial flexible CZTSSe thin film solar cells for indoor photovoltaic applications,"

[123] A. Gerthoffer, F. Roux, F. Emieux, P. Faucherand, H. Fournier, L. Grenet, and S. Perraud, "CIGS solar cells on flexible ultra-thin glass substrates: Characterization and bending test," *Thin Solid Films*, 2015.

[124] X. Xu, Y. Qu, V. Barrioz, G. Zoppi, and N. Beattie, "Reducing series resistance in $Cu_2ZnSn(S,Se)_4$ nanoparticle ink solar cells on flexible molybdenum foil substrates," *RSC Advances*, vol. 8, no. 7, 2018.

[125] S. Campbell, M. Duchamp, B. Ford, M. Jones, L. Lna Nguyen, M. C. Naylor, P. Xu, Xinya nd Maiello, G. Zoppi, V. Barrioz, N. S. Beattie, and Y. Qu, "Recovery Mechanisms in Aged Kesterite," ACS Applied Energy Materials 2022.

[126] C. Neubauer, A. Samieipour, S. Oueslati, M. Danilson, and D. Meissner, "Ageing of kesterite solar cells 1: Degradation processes and their influence on solar cell parameters," *Thin Solid Films*, vol. 669, pp. 595–599, Jan 2019.

[127] A. Samieipour, C. Neubauer, S. Oueslati, V. Mikli, and D. Meissner, "Ageing of kesterite solar cells 2: Impact on photocurrent generation," *Thin Solid Films*, vol. 669, pp. 509–513, Jan 2019.

[128] C. Yan, J. Huang, K. Sun, S. Johnston, Y. Zhang, H. Sun, A. Pu, M. He, F. Liu, K. Eder, L. Yang, J. M. Cairney, N. J. Ekins-Daukes, Z. Hameiri, J. A. Stride, S. Chen, M. A. Green, and X. Hao, "Cu_2ZnSnS_4 solar cells with over 10% power conversion efficiency enabled by heterojunction heat treatment," *Nature Energy*, 2018.

[129] P. Fan, J. Zhao, G. X. Liang, D. Gu, Z. H. Zheng, D. P. Zhang, X. M. Cai, J. T. Luo, and F. Ye, "Effects of annealing treatment on the properties of CZTSe thin films deposited by RF-magnetron sputtering," *Journal of Alloys and Compounds*, vol. 625, pp. 171–174, 2015.

[130] H. Xie, S. López-Marino, T. Olar, Y. Sánchez, M. Neuschitzer, F. Oliva, S. Giraldo, V. Izquierdo-Roca, I. Lauermann, A. Pérez-Rodríguez, and E. Saucedo, "Impact of Na Dynamics at the $Cu_2ZnSn(S,Se)_4$/CdS Interface during Post Low Temperature Treatment of Absorbers," *ACS Applied Materials and Interfaces*, 2016.

[131] S. K. Hwang, J.-H. Park, K. B. Cheon, S. W. Seo, J. E. Song, I. J. Park, S. G. Ji, M.-A. Park, and J. Y. Kim, "Improved interfacial properties of electrodeposited $Cu_2ZnSn(S,Se)_4$ thin-film solar cells by a facile post-heat treatment process," *Progress in Photovoltaics: Research and Applications*, vol. 28, no. 12, pp. 1345–1354, 2020.

[132] G. Rey, T. P. Weiss, J. Sendler, A. Finger, C. Spindler, F. Werner, M. Melchiorre, M. Hála, M. Guennou, and S. Siebentritt, "Ordering kesterite improves solar cells: A low temperature post-deposition annealing study," *Solar Energy Materials and Solar Cells*, vol. 151, pp. 131–138, 2016.

[133] D. Hironiwa, N. Sakai, T. Kato, H. Sugimoto, Z. Tang, J. Chantana, and T. Minemoto, "Impact of annealing treatment before buffer layer deposition on $Cu_2ZnSn(S,Se)_4$ solar cells," in *Thin Solid Films*, 2015.

[134] C. M. Sutter-Fella, J. A. Stückelberger, H. Hagendorfer, F. La Mattina, L. Kranz, S. Nishiwaki, A. R. Uhl, Y. E. Romanyuk, and A. N. Tiwari, "Sodium Assisted Sintering of Chalcogenides and Its Application to Solution Processed $Cu_2ZnSn(S,Se)_4$ Thin Film Solar Cells," *Chemistry of Materials*, vol. 26, no. 3, pp. 1420–1425, 2014.

[135] T. Mise, S. Tajima, T. Fukano, K. Higuchi, T. Washio, K. Jimbo, and H. Katagiri, "Improving the photovoltaic performance of co-evaporated Cu_2ZnSnS_4 thin-film solar cells by incorporation of sodium from NaF layers," *Progress in Photovoltaics: Research and Applications*, vol. 24, no. 7, pp. 1009–1015, 2016.